

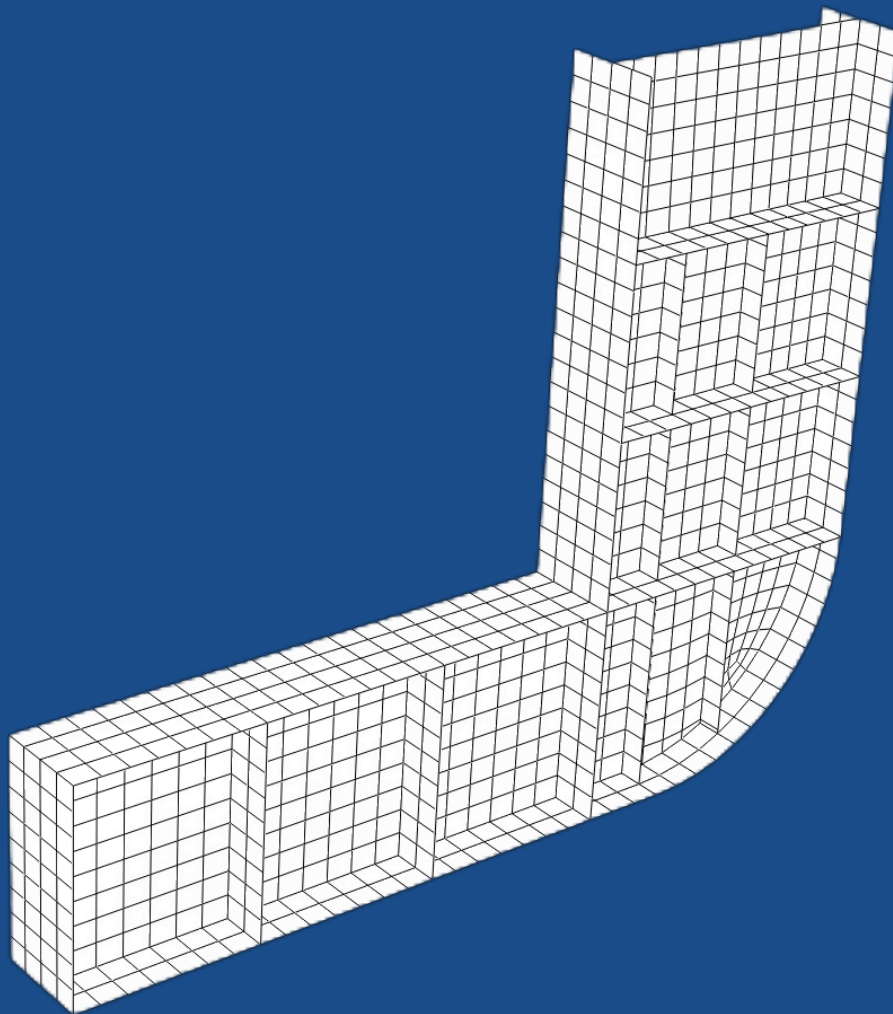
# Fatigue resistance similarity

---

Small-scale specimen test data reflecting the  
performance of full-scale maritime structures

---

M. B. Zwiép





# Fatigue resistance similarity

Small-scale specimen test data reflecting the  
performance of full-scale maritime structures

Thesis report

by

M. B. Zwiép

to obtain the degree of Master of Science  
at the Delft University of Technology  
to be defended publicly on Thursday 6<sup>th</sup> June, 2024

*Thesis committee:*

Chair:	Dr. Ir. J.H. Den Besten
Supervisors:	Ir. J.D. Rodenburg Ir. M.L. Deul
Committee member:	Dr. A. Grammatikopoulos
Place:	Faculty of Mechanical Engineering, Delft
Project Duration:	July 2023 - June 2024
Student number:	4707761

An electronic version of this thesis is available at <http://repository.tudelft.nl/>.



Copyright © Max Zwiep, 2024  
All rights reserved.

# Preface

Dear reader,

This report is my master thesis on the topic of "Fatigue resistance similarity." This thesis marks the end of my master's Offshore & Dredging Engineering at the Delft University of Technology. The work was completed under the supervision of Henk den Besten (TU Delft), Jorrit Rodenburg, and Marije Deul (both TNO).

First of all, Henk, thank you for helping me navigate the world of graduating. From finding a topic, connecting me with TNO, and, of course, all our meetings where, with your critical perspective, you made me evaluate my own results. The feedback was always thorough and greatly helped me in finding my final conclusions. Jorrit, thank you for all the time and effort you put into improving my thesis. Our bi-weekly meetings forced me to regularly reflect on my work, ensuring that the overview remained clear. Also, thank you for always being available for any small questions in between. Marije, thank you for ensuring my place at TNO before you had to step away for a while, and for staying involved in my thesis, albeit perhaps more from the background. Lastly, thank you to the steel team of TNO, you welcomed me with open arms in the upper corner of the Molengraaffsingel. Even though I had my own personal project, it was valuable to learn how a team operates within a bigger company. You made my time here certainly worth remembering.

To my friends and family with whom I had discussions about fatigue, graduating, and in general helping me through this period of graduating, thank you!

M. B. (Max Beerend) Zwiep  
Delft, June 2024

# Summary

This master's thesis investigates the fatigue resistance similarity between small-scale test specimens and large-scale structures, specifically focusing on steel welded joints. The primary goal is to improve the understanding of how fatigue data from small-scale tests can be reliably applied to predict the performance of full-scale maritime structures, thereby reducing conservatism in design and optimizing material usage without compromising safety.

Fatigue resistance is a critical factor in the design and maintenance of maritime structures. Traditional design methods often use S-N curves derived from small-scale specimen tests, which can be overly conservative when applied to full-scale structures. This conservatism, while ensuring safety, leads to increased material use and associated costs. The aim is to identify and quantify the scaling phenomena that influence the transfer of fatigue data from small-scale specimens to full-scale structures. By proving fatigue resistance similarity and understanding these scaling effects, the research seeks to refine the fatigue design process, thereby enhancing efficiency and reducing environmental impact.

The research utilizes various fatigue assessment concepts, including the Nominal Stress Concept (NSC), Hot Spot Structural Stress Concept (HSSSC), and the Effective Notch Stress Concept (ENSC). Finite Element (FE) models of large-scale specimens, created using Abaqus, are used to test these concepts. The study also explores the application of mean stress correction models to improve the fit of large-scale data within small-scale data scatter bands. The methods are evaluated based on their ability to incorporate local geometry information and their effectiveness in reducing scatter in fatigue data.

The study demonstrates that incorporating local geometry information is crucial for achieving fatigue resistance similarity between small-scale and large-scale specimens. The HSSSC and ENSC, which account for local geometrical variations, provide better fits for large-scale data within the small-scale data scatter bands compared to the NSC. This confirms the hypothesis that local weld geometry plays a significant role in fatigue resistance similarity. Furthermore, applying a mean stress correction improves the alignment of large-scale data with small-scale data, highlighting the importance of considering residual stresses and load ratios in fatigue assessments.

The findings can have practical implications for the design and maintenance of maritime structures. By improving the accuracy of fatigue life predictions, the research supports the development of more efficient and cost-effective designs. The insights gained from this research help address uncertainties and improve design assumptions for vessel fatigue performance. By incorporating local geometry information and applying mean stress corrections, the research provides a more accurate and less conservative approach to fatigue life prediction. These advancements have the potential to reduce material usage and costs in maritime structure design, while maintaining high safety standards.

# Samenvatting

Deze studie onderzoekt de overeenkomsten in vermoeiingsweerstand tussen kleinschalige proefstukken en grootschalige constructies, met een specifieke focus op stalen gelaste verbindingen. Het primaire doel is het verbeteren van het begrip van hoe vermoeiingsgegevens uit kleinschalige testen betrouwbaar kunnen worden toegepast om de prestaties van grootschalige maritieme constructies te voorspellen, waardoor conservatisme in de ontwerpfase kan worden verminderd en het materiaalgebruik wordt geoptimaliseerd zonder de veiligheid in gevaar te brengen.

Vermoeiingsweerstand is een kritieke factor bij het ontwerp en onderhoud van maritieme structuren. Traditionele ontwerpmethoden gebruiken vaak S-N-curves die zijn afgeleid van kleinschalige proefstuktesten, die overdreven conservatief kunnen zijn wanneer ze worden toegepast op grootschalige structuren. Dit conservatisme, hoewel het de veiligheid waarborgt, leidt tot een verhoogd materiaalgebruik en bijbehorende kosten. Het doel is het identificeren en kwantificeren van de schaalfenomenen die van invloed zijn op de overdracht van vermoeiingsgegevens van kleinschalige proefstukken naar grootschalige structuren. Door de overeenkomsten in vermoeiingsweerstand aan te tonen en deze schaalinvloeden te begrijpen, streeft het onderzoek ernaar het vermoeiingsontwerpproces te verfijnen, waardoor de efficiëntie wordt verbeterd en de milieu-impact wordt verminderd.

Het onderzoek maakt gebruik van verschillende vermoeiingsbeoordelingsconcepten, waaronder het Nominale Spanningsconcept (NSC), het Hot Spot Structurele Spanningsconcept (HSSSC), en het Effectieve Notch Spanningsconcept (ENSC). Finite Element (FE) modellen van grootschalige proefstukken, gemaakt met behulp van Abaqus, worden gebruikt om deze concepten te testen. De studie onderzoekt ook de toepassing van modellen voor gemiddelde spanningscorrectie om de passing van grootschalige gegevens binnen de kleinschalige gegevensverstrooiingsbanden te verbeteren. De methoden worden geëvalueerd op basis van hun vermogen om lokale geometrie-informatie te integreren en hun effectiviteit in het verminderen van de verstrooiing in vermoeiingsgegevens.

De studie toont aan dat het integreren van lokale geometrie-informatie cruciaal is voor het bereiken van overeenkomsten in vermoeiingsweerstand tussen kleinschalige en grootschalige proefstukken. Het HSSSC en ENSC, die rekening houden met lokale geometrische variaties, zorgen ervoor dat de grootschalige gegevens beter binnen de kleinschalige gegevensverstrooiingsbanden passen in vergelijking met het NSC. Dit bevestigt de hypothese dat lokale geometrie een significante rol speelt in de overeenkomsten in vermoeiingsweerstand. Bovendien verbetert de toepassing van een gemiddelde spanningscorrectie de afstemming van grootschalige gegevens met kleinschalige gegevens, wat het belang van het overwegen van residuele spanningen en belastingverhoudingen in vermoeiingsbeoordelingen benadrukt.

De bevindingen kunnen praktische implicaties hebben voor het ontwerp en onderhoud van maritieme structuren. Door de nauwkeurigheid van vermoeiingslevensduurvoorspellingen te verbeteren, ondersteunt het onderzoek de ontwikkeling van efficiëntere en kosteneffectievere ontwerpen. De inzichten die uit dit onderzoek zijn verkregen, helpen onzekerheden aan te pakken en de ontwerpaanpak voor vermoeiingsprestaties van schepen te verbeteren. Door lokale geometrie-informatie te integreren en gemiddelde spanningscorrecties toe te passen, biedt het onderzoek een nauwkeurigere en minder conservatieve benadering van vermoeiingslevensduurvoorspelling. Deze vooruitgangen hebben het potentieel om het materiaalgebruik en de kosten in het ontwerp van maritieme structuren te verminderen, terwijl hoge veiligheidsnormen worden gehandhaafd.

# Contents

<b>Summary</b>	<b>iv</b>
<b>Samenvatting</b>	<b>v</b>
<b>Table of Contents</b>	<b>vi</b>
<b>List of Figures</b>	<b>viii</b>
<b>List of Tables</b>	<b>x</b>
<b>1 Introduction</b>	<b>1</b>
1.1 Fatigue fundamentals . . . . .	1
1.2 Problem definition . . . . .	4
1.3 Motivation & Relevance . . . . .	4
1.4 Research goal . . . . .	5
1.5 Scope . . . . .	5
1.6 Report outline . . . . .	5
<b>I Literature review</b>	<b>6</b>
<b>2 Fatigue assessment concepts</b>	<b>7</b>
2.1 Nominal stress concept . . . . .	8
2.2 Hot spot structural stress concept . . . . .	9
2.3 (Averaged) Effective notch stress concept . . . . .	10
2.4 Total stress concept . . . . .	10
2.5 Concluding remarks . . . . .	11
<b>3 Small- and large-scale specimen fatigue resistance similarity</b>	<b>12</b>
3.1 Small-scale specimen fatigue resistance . . . . .	12
3.2 Large-scale specimen fatigue resistance . . . . .	15
3.3 Full-scale structure fatigue loading & response . . . . .	18
3.4 Scale Effects . . . . .	19
3.5 Concluding remarks . . . . .	26
<b>4 Research overview</b>	<b>29</b>
4.1 Knowledge gap . . . . .	29
4.2 Hypotheses . . . . .	29
4.3 Methods . . . . .	30
<b>II Research</b>	<b>31</b>
<b>5 Small- &amp; large-scale specimens</b>	<b>32</b>
5.1 Small-scale specimens . . . . .	32
5.2 Large-scale specimens . . . . .	34
<b>6 Similarity analysis</b>	<b>45</b>
6.1 Nominal stress concept . . . . .	45
6.2 Hot spot structural stress concept . . . . .	56
6.3 Effective notch stress concept . . . . .	64
6.4 Scale effects . . . . .	71

---

<b>III Judgement &amp; future work</b>	<b>75</b>
<b>7 Evaluation</b>	<b>76</b>
7.1 Conclusions . . . . .	76
7.2 Discussion . . . . .	78
7.3 Recommendations . . . . .	81
<b>References</b>	<b>87</b>
<b>A Derivations</b>	<b>88</b>
A.1 Weakest link theory . . . . .	88
<b>B HSSSC analysis</b>	<b>91</b>
B.1 Bilge corner . . . . .	91
B.2 T-shaped stiffener . . . . .	92
B.3 Scallop . . . . .	93
<b>C ENSC analysis</b>	<b>95</b>

# Nomenclature

## List of Abbreviations

CA	Constant Amplitude
CAT	Fatigue CATegories
CEN	Comité Européen de Normalisation
DNV	Det Norske Veritas
DS	Double-sided
ENSC	Effective Notch Stress Concept
FAT	FATigue classes
FE	Finite Element
FEA	Finite Element Analysis
HCF	High cycle fatigue
HMS	Hull monitoring system
HS	Hot spot
HSSSC	Hot Spot Structural Stress Concept
IIW	International Institute of Welding
LC	Load-carrying
LCF	Low cycle fatigue
LDAM	Linear Damage Accumulation Model
LSS	Large-scale specimen
MCF	Medium cycle fatigue
MLE	Maximum Likelihood Estimator
MSC	Macroscopic stress concentration
mSC	Micro- or meso-scale stress concentration
NLC	Non-load-carrying
NSC	Nominal Stress Concept
SCF	Stress Concentration Factor
SIF	Stress Intensity Factor
SS	Single-sided

SSS	Small-scale specimen
TSC	Total Stress Concept
VA	Variable Amplitude

## List of Symbols

$\Delta\sigma$	Stress range
$\Delta\sigma_s$	Structural stress range
$\rho^*$	Micro-structural support length
$\rho$	Notch radius
$\rho_e$	Effective notch radius
$\sigma$	Standard deviation
$C$	Scaling factor
$C_{bw}$	Weld load carrying stress coefficient
$D$	(total) fatigue damage
$K$	Stress intensity factor
$m$	Fatigue resistance slope
$N$	(total) number of cycles until failure
$P_f$	Probability of failure
$S$	Stress range
$s$	Notch support factor
$S_e$	Effective (notch) stress range
$S_n$	Nominal stress range
$S_s$	(hot spot) structural stress range
$t_p$	Plate thickness
$T_{\sigma_s}$	Strength scatter band index
$Y_f$	Far-field factor
$Y_n$	Notch factor
R	Load ratio

# List of Figures

1.1	Stages and periods of the fatigue life (Schijve, 2009)	1
1.2	S-N curves for various classes of welded-joints (Arzola et al., 2017)	2
1.3	Explanation of the Palmgren-Miner model (NEN, 2012)	3
1.4	Loading modes I, II and III (Zehnder, 2013)	3
1.5	Different hotspot types (DNV, 2021a)	4
2.1	Overview of different fatigue concepts (den Besten, 2018)	7
2.2	Nominal stress based small-scale data scatter band (Qin et al., 2019)	9
3.1	Example of a double S-N curve (Sungwoo et al., 2021)	13
3.2	Characteristic stress levels of a load cycle, $S_{max}$ = maximum stress level, $S_m$ = mean stress level, $S_{min}$ = minimum stress level, $S_a$ = stress amplitude, $\Delta S$ = stress range (Schijve, 2009)	14
3.3	Nominal stress small-scale specimen data scatter band without (left) and with (right) mean stress correction (Qin et al., 2019)	14
3.4	Types of tubular joints (Saini et al., 2016)	15
3.5	An example of a typical stiffened panel (Paik et al., 2002)	16
3.6	Large-scale specimen of a side-longitudinal (Lotsberg et al., 2005)	17
3.7	Large-scale specimen of a bilge corner (C. Fischer et al., 2018)	17
3.8	Large-scale specimen of a T-shaped longitudinal stiffener (Rizzo et al., 2007)	18
3.9	Failure probability density function of cables with different lengths (Heckel et al., 1975)	20
3.10	Visualization of the weakest link argument (Pedersen, 2019)	20
3.11	Geometry of the mini and standard specimens (Tomaszewski, 2018)	21
3.12	Fatigue data for mini and standard specimens (Tomaszewski, 2018)	21
3.13	Notch size effect (Liao et al., 2020)	23
3.14	S-N curve for different surface roughnesses (Alang et al., 2011)	24
3.15	Effect of tensile residual stress on fatigue life (Sonsino, 2009)	26
3.16	Scaling phases 1 & 2, corresponding with scaling from small-scale specimens (Loporcaro et al., 2015) to large-scale specimens (Fricke et al., 2010) and from large-scale specimens to full-scale structures (Siemens, 2021), respectively	27
5.1	SSS database scatter band excluding run-outs	33
5.2	Large-scale specimen database by joint types	35
5.3	Selected large-scale specimens	36
5.4	The bilge corner specimen (C. Fischer et al., 2018)	37
5.5	Schematic of the bilge corner (Kozak, 1999)	37
5.6	The propagation of fatigue cracks in one of the specimens (Kozak et al., 2015)	38
5.7	Overview of the bilge corner FE model in loaded condition	39
5.8	Boundary conditions and loading position of the bilge corner	39
5.9	T-shaped stiffener connection (C. Fischer et al., 2018)	40
5.10	Schematic of the T-shaped stiffener (Rizzo et al., 2007)	41
5.11	Overview of the T-shaped stiffener FE model in loaded condition	42
5.12	Boundary conditions and loading position of the T-shaped stiffener	42
5.13	Double-sided H-shaped attachment (Z.-G. Xiao et al., 2005)	43
5.14	Schematic of the scallop (Z.-G. Xiao et al., 2005)	43
5.15	Overview of the scallop FE model in loaded condition	44
5.16	Boundary conditions and loading position of the scallop	44
6.1	NSC SSS database scatter band including run-outs	46
6.2	SSS database scatter band excluding run-outs	47
6.3	Curves with a varying slope	48

6.4	Large-scale specimen database by joint type	49
6.5	Large-scale specimen database by HS-type	50
6.6	Large-scale specimen database by plate thickness	51
6.7	Large-scale specimen database by load ratio	52
6.8	Large-scale & small-scale specimen database nominal stress comparison	53
6.9	Large-scale & small-scale specimen DS cruciform joint comparison	54
6.10	Large-scale & small-scale specimen DS longitudinal attachment comparison	54
6.11	Large-scale & small-scale specimen DS T-joint comparison	55
6.12	Large-scale & small-scale specimen DS butt joint comparison	55
6.13	Large-scale & small-scale specimen SS longitudinal attachment comparison	56
6.14	HSSSC SSS database scatter band	57
6.15	Stress distribution on the path towards the hot spot on the bilge corner	58
6.16	FEM detail of the hot spot	58
6.17	Visual representation of the structural stress method (Dong, 2001)	59
6.18	Stress distribution on the path towards the hot spot on the T-shaped stiffener	60
6.19	Stress distribution on the path towards the hot spot on the scallop	62
6.20	FEM detail of the hot spot	62
6.21	SSS and LSS comparison hot spot structural stress	64
6.22	Sketch with input parameters for the ENSC (Qin et al., 2019)	65
6.23	ENSC SSS database scatter band	66
6.24	Notch & far-field stress distribution for the bilge corner	67
6.25	Notch & far-field stress distribution for the T-shaped stiffener	68
6.26	Notch & far-field stress distribution for the scallop	69
6.27	SSS and LSS comparison effective notch stress	70
6.28	SSS and LSS comparison effective notch stress with scatter parameters	70
6.29	SSS and LSS comparison nominal stress	71
6.30	SSS and LSS comparison hot spot structural stress	72
6.31	SSS and LSS comparison effective notch stress	72
6.32	SSS and LSS comparison with the mean stress correction	73
6.33	SSS and LSS comparison without the mean stress correction	74
6.34	SSS and LSS comparison with a different mean stress correction	74
7.1	SSS and LSS comparison hot spot structural stress with a different failure criterion for the bilge corner	78
7.2	SSS and LSS comparison effective notch stress with a different failure criterion for the bilge corner	79
7.3	HS type A and C comparison for the bilge corner	79
7.4	HSSSC comparison using the virtual node method	80
7.5	ENSC comparison using the virtual node method	80
7.6	SSS and LSS comparison effective notch stress with a different failure criterion for the bilge corner	81
A.1	Relationship between the probability of failure $P_f$ and number of cycles $N$	89
A.2	Relationship between the probability of failure $P_f$ and stress range $S$	90
B.1	Method to convert nodal forces to line forces	91
B.2	Structural stress calculation	91
B.3	Structural stress mesh size comparison	92
B.4	Virtual node method (den Besten, 2021b)	92
B.5	Stress calculation using the virtual node method	93
B.6	Structural stress mesh size comparison	93
B.7	Nodal forces of the scallop for different mesh sizes	93
B.8	Structural stress mesh size comparison	94

# List of Tables

3.1	Specimen dimensions . . . . .	21
4.1	The methods used to check for the effect of different scale effects . . . . .	30
5.1	The large-scale specimen database . . . . .	34
6.1	Scatter parameters comparison for the different joints . . . . .	56
6.2	Results linear extrapolation of the bilge corner . . . . .	57
6.3	Results hot spot stress calculations of the bilge corner . . . . .	60
6.4	Results linear extrapolation of the T-shaped stiffener . . . . .	60
6.5	Results hot spot stress calculations of the T-shaped stiffener . . . . .	61
6.6	Results linear extrapolation of hot spot stress for the scallop . . . . .	61
6.7	Results hot spot stress calculations for the scallop . . . . .	63
6.8	The $K_s$ factors for all three specimens . . . . .	63
6.9	Scatter parameters large-scale specimens for the HSSSC . . . . .	64
6.10	The $K_e$ and $K_t$ factors for all three specimens . . . . .	69
6.11	Scatter parameters large-scale specimens for the ENSC . . . . .	71
7.1	Scatter parameters large-scale specimens for the HSSSC . . . . .	77
7.2	Scatter parameters large-scale specimens for the ENSC . . . . .	77

# Introduction

Maritime structures, including vessels, offshore wind turbines (floating or fixed), and platforms, are subjected to cyclic mechanical loading and response conditions, which are caused by the environment or operational demands. Therefore, fatigue is a critical limiting state for these structures (Schijve, 2009). An understanding of fatigue behavior is essential to ensure the structural integrity and safety of maritime structures.

## 1.1. Fatigue fundamentals

The fatigue damage process is split into two periods: the crack initiation period and the crack growth period. Figure 1.1 shows different stages and periods of the fatigue life.

The first period includes the crack nucleation and crack growth on micro-scale. In the second period, the crack grows until fracture (Schijve, 2009). For the nucleation of cracks, (local) plasticity is required. This phenomenon primarily manifests as dislocation activities or cyclic slip at the micro- and meso-scale of the material structure. In situations where the material is subjected to stresses below its yield strength, plastic deformation is confined to a limited number of grains, predominantly those positioned at the material's surface. This is because, at the free surface, there is a lower constraint on the slip because the surrounding material is only present at one side (Schijve, 2009). Consequently, slip events give rise to intrusion-extrusion pairs, which introduce micro- and mesoscopic stress concentrations (mSCs) within the material (den Besten, 2018).

At the macro-scale, these mSCs are supported by macroscopic stress concentrations (MSCs), which are localized regions of elevated stress. Imperfections and discontinuities within the material serve as locations where these MSCs, acting as hot spots, tend to emerge. In the context of maritime structures, welded joints are particularly prone to experiencing such imperfections and flaws.

The transition from the initiation period to the growth period occurs when the development of the crack no longer depends on the local surface condition, but instead primarily depends on the crack growth resistance of the material as a kind of bulk property (Schijve, 2012). However, how to define the exact moment of the transition is more difficult. It is a gradual process and will not suddenly occur.

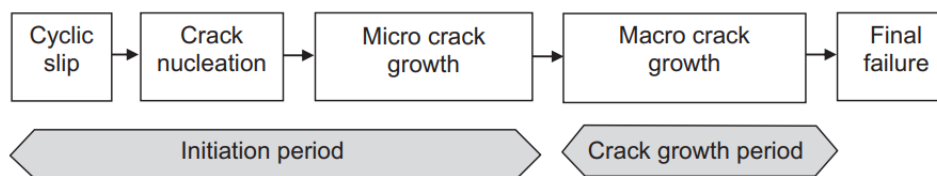


**Figure 1.1:** Stages and periods of the fatigue life (Schijve, 2009).

Numerous models have been developed for describing and predicting fatigue life. Augustus Wöhler (1819-1914) was one of the first who conducted research demonstrating that fractures could occur under

repeated stresses significantly below the yield strength (Wöhler, 1860). Between 1858 and 1870, Wöhler published five different papers on fatigue strength and conducting fatigue tests (Zenner et al., 2019). Building upon Wöhler's experimental data, Basquin introduced a logarithmic relationship for S-N curves in 1910, wherein  $S$  represents the elastic stress range and  $N$  denotes the number of load cycles. Basquin's linear relationship is shown in equation (1.1). Basquin's equation remains highly relevant in today's fatigue analysis, and numerous modifications and extensions have been proposed over the past century to enhance its applicability. Figure 1.2 displays an example S-N curve for various classes of welded joints, with on the x-axis the number of cycles until failure and on the y-axis the corresponding stress range in MPa.

$$\log(N) = \log(C) - m * \log(S) \quad (1.1)$$

The number of fatigue life cycles is typically expressed as  $N$  and can be divided into three categories, low cycle fatigue (LCF), mid cycle fatigue (MCF) and high cycle fatigue (HCF). LCF corresponds to  $N < 10^4$ , MCF to  $10^4 < N < 5 \cdot 10^6$  or  $1 \cdot 10^7$ , the exact limit varies in literature. HCF corresponds to  $5 \cdot 10^6$  or  $1 \cdot 10^7 < N$ . For maritime applications, the mid- and high-cycle fatigue range are the governing design limit state, because of the design lifetime of around 30 years.

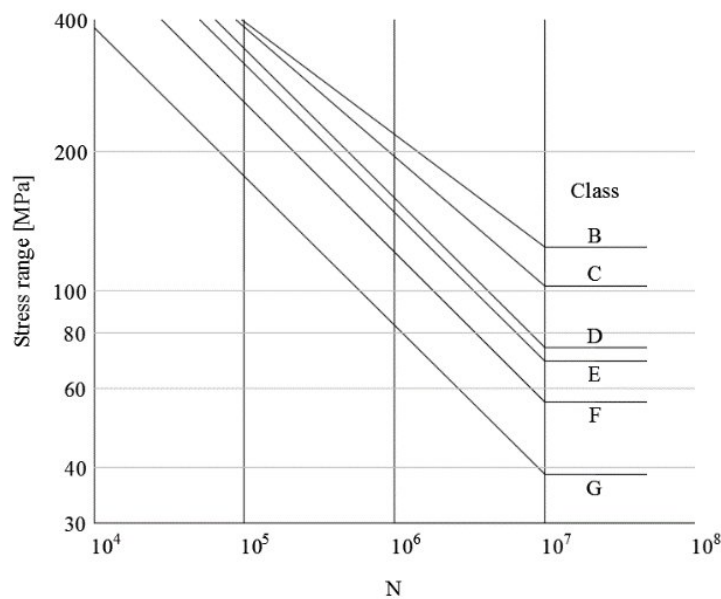


**Figure 1.2:** S-N curves for various classes of welded-joints (Arzola et al., 2017)

As explained, fatigue damage accumulates over a multitude of cycles. In this context, the Linear Damage Accumulation Model (LDAM) by Palmgren (1924) and later refined by Miner (1945), is a fundamental concept that plays a pivotal role in assessing the durability of various structures subjected to repetitive loading conditions. The LDAM is most often used in practice due to its simplicity (Inoma et al., 2019), and its integration in multiple fatigue design codes (Hobbacher, 2016; NEN, 2012).

At the core of the LDAM is the principle that the life of a structure or component can be equated to the sum of damage contributions from each load cycle it experiences. Basically, it acknowledges that repeated load cycles at different stress levels contribute cumulatively to the overall fatigue damage. The Palmgren-Miner equation is given in equation (1.2), where the number of stress levels is denoted as  $k$ , the number of cycles per stress level as  $n_i$  and the number of cycles to failure per stress level as  $N_i$ , as mentioned in section 1.1. A visualization of the Palmgren-Miner's principle is given in figure 1.3. It can be seen that the design S-N curve determines what the allowed number of cycles to failure is for a stress level. When the cumulative damage, denoted as  $D$ , is equal to 1, the structure is expected to fail.

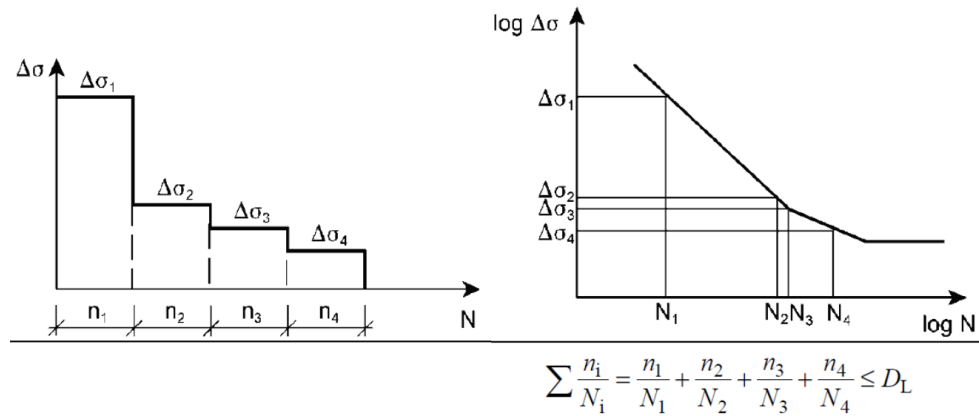


**Figure 1.3:** Explanation of the Palmgren-Miner model (NEN, 2012)

$$D = \sum_{i=1}^k \frac{n_i}{N_i} \quad (1.2)$$

The Palmgren-Miner rule is a valuable tool in fatigue design, however, it also has weak points that limit its applicability. Due to its linearity, the validity of the Palmgren-Miner model for VA loading is questionable. If for every random load cycle  $\frac{n_i}{N_i}$  needed to be determined, it would become very unpractical. The model is unable to capture the effects related to variable amplitudes properly (Fatemi et al., 1998), however, the model can give a good estimate for typical maritime loads (Garbatov et al., 2018). Typically, damage accumulation models based on VA loading, such as the method by Leonetti et al. (2020), are more useful for maritime applications.

For crack growth, three loading modes can be distinguished, see figure 1.4. Mode-I shows crack growth perpendicular to the loading direction. Loading mode-I appears under normal and bending stresses, which are the most governing for maritime structures for multiple reasons. Firstly is the construction set-up for stiffened plates. The hierarchy of the members leads to normal stresses since the structural members vary in direction. Another reason is that normal stresses are governing in thin-walled structures. Mode-II shows in-plane shear, usually not so relevant for maritime applications. Mode-III shows out-of-plane shear, which could contribute significantly to certain applications.

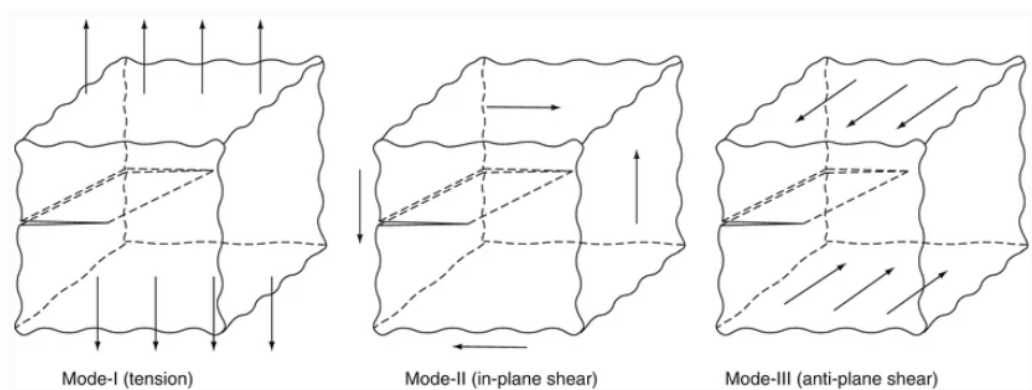


**Figure 1.4:** Loading modes I, II and III (Zehnder, 2013).

Macroscopic stress concentrations (MSCs) act as hot spots (HS). These fatigue hot spot locations can generally be categorized into three different groups, HS type A, B, and C (den Besten, 2021a; DNV, 2021a). These three groups are distinguished, because crack growth behavior and stress calculations can differ depending on the HS type. The different types can be seen in figure 1.5.

- Hot spot type A: Notches that can be found at the weld toe on the plate surface at an ending attachment, perpendicular to the weld seam.
- Hot spot type B: Notches that can be found at the weld toe around the plate edge of an ending attachment, parallel to the weld seam.
- Hot spot Type C: Notches that can be found at the weld toe of an attached plate on both the plate and attachment surface.

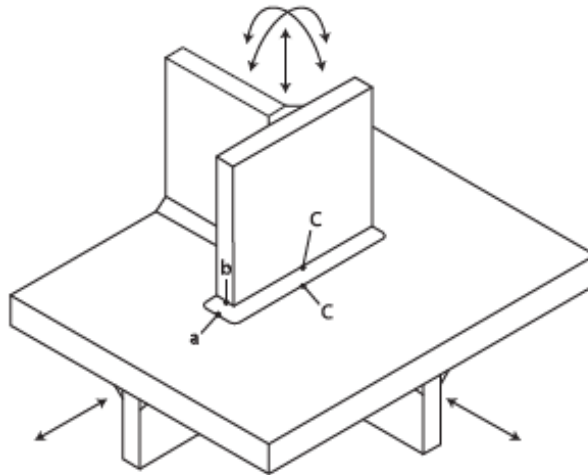


Figure 1.5: Different hotspot types (DNV, 2021a).

## 1.2. Problem definition

The fatigue life of a structure is often determined using design S-N curves. S-N curves are constructed using fatigue tests. A wide range of specimens have been tested, from which fatigue test data points have been obtained. These points are plotted in an S-N plot, through which an S-N curve can be drawn.

To assess the fatigue endurance of an entire structural system, ideally, a fatigue test of the full-scale structure would prove the actual fatigue limit state performance. However, such tests are impossible due to financial and technical limitations. A full-scale structure does not fit in a fatigue test rig and testing in actual operational conditions would mean testing for the intended operational lifetime. Consequently, researchers resort to performing experiments on small-scale specimens as an alternative approach. These results are then utilized to design a full-scale structure for its fatigue life. This adoption of small-scale specimen fatigue data into the design of full-scale structures involves the assumption that fatigue behavior remains consistent on smaller and larger scales. Literature illustrates that full-scale structures can exhibit different fatigue performance than their small-scale equivalents. Results from Fricke et al. (2010) agree quite well with the design S-N curves, however, Maddox et al. (2008) demonstrate that the high-cycle fatigue strength and the fatigue limit of full-scale specimens are significantly lower than those for strip specimens. For that reason, conservatism in the form of safety factors is introduced into the design S-N curves to prevent early fatigue failure. Gaining more insight into the differences in fatigue behavior when scaling from smaller to larger scales would help reduce conservatism in the design of full-scale structures. Furthermore, using more advanced fatigue strength criteria, which can incorporate the differences, may be a way to achieve resistance similarity between small-scale specimens and full-scale structures.

## 1.3. Motivation & Relevance

The fatigue strength of maritime structures is a primary concern for ensuring the safety and longevity of these complex structures, structures that are becoming increasingly important as offshore markets continue to expand. As the demand for offshore resources surges, these structures are pushed to their operational limits, and subjected to harsh environmental conditions such as extreme waves, corrosive saltwater, and cyclic mechanical loading and response conditions. Given the high costs and critical roles these structures

play in energy production, transportation, and maritime exploration, any structural failure due to fatigue could lead to not only substantial economic losses but also severe environmental consequences.

As mentioned, the design for fatigue strength often relies on S-N curves, which in most cases are typically conservative. Deul et al. (2022) proved that for some specific cases, the stress in small-scale specimens is higher in comparison to the original full-scale plate. So full-scale plates based on these small-scale specimen S-N curves will be overly conservative. In design standards, the design S-N curve is the mean S-N curve minus two times the standard deviation, associated with a 97.5% probability of survival (DNV, 2021a). From a safety perspective, conservatism is not necessarily a bad thing. Nevertheless, a better understanding of the establishment of S-N curves can lead to more confidence with regard to fatigue life prediction. When there is more confidence, less steel can be used which in turn leads to a reduction of structural weight, without compromising safety standards. Reduction of structural weight has multiple benefits, such as savings of cost, increased payload per capacity, and less environmental impact.

This thesis also has relevance for the FReady project. The FReady project is a joint industry project by various companies and institutions around the world. This thesis is done under the supervision of TNO and the Technical University of Delft, which are both part of the FReady fatigue resistance team, a sub-team of the FReady project. This team also includes Nevesbu, Femto, and COMMIT. The research of the team focuses on uncertainties and calculation assumptions based on information known at the design stage of a vessel. This thesis will help to add knowledge to this research goal.

## 1.4. Research goal

The goal of this research is to improve the understanding of fatigue resistance similarity between steel small-scale test specimens and large-scale specimens used for fatigue design. Specifically listing and quantifying the scaling phenomena that arise when transferring fatigue data from small-scale specimen tests to large-scale results used for structure design. Proving fatigue resistance similarity and mapping these scale effects and their influence on the fatigue strength of a full-scale structure can reduce design conservatism.

## 1.5. Scope

The research will make use of intact geometry fatigue assessment only and will cover only steel welded joints. The loading considered will be uni-axial, so mode-I loading and of a constant amplitude. Variable amplitude loading will not be considered in this research. Differences between stiffened panels and truss/frame type configurations will be mentioned, but research will focus only on stiffened panels as they are relevant for ship structures and the FReady project focuses on ships.

## 1.6. Report outline

This literature review aims to address the current state of the art for fatigue resistance similarity. The initial chapter, chapter 2, will delve into the different fatigue assessment concepts that are viable to use. Furthermore, the subsequent chapter 3 will delve into the scale effects between small-scale and large-scale specimens. Next, chapter 4 will provide an overview of the proposed research. The following chapters will start discussing the research, with chapter 5 discussing small- and large-scale specimens, and chapter 6 performing the similarity analysis. Chapter 7 will provide the conclusions, discussion points, and recommendations.

# Part I

## Literature review

# Fatigue assessment concepts

Over time, multiple fatigue assessment concepts have been developed to assess the fatigue lifetime of a structure. The concepts are shown in figure 2.1 and can be classified using (den Besten, 2018):

- global or local information criteria
- intact or cracked geometry criteria
- stress (intensity), strain (intensity), or energy (density) parameter criteria
- point, line, or area/volume criteria

The first category dictates the level of detail taken into consideration in the concept. This can either be global information about a structural detail, or local information concerning a specific (welded) joint. The next difference is in whether an intact or cracked geometry is considered. Although the fatigue lifetime of arc-welded joints is typically limited to growth, thus with an existing crack, the biggest part of the lifetime is spent in the weld notch affected region, meaning an SCF-related concept makes sense as well (den Besten, 2018).

A fatigue assessment concept can be based on a stress, strain, or energy parameter. Which parameter is used is dependent on the underlying nature of the problem. If the problem is predominantly linear elastic, the stress type parameter is used. If elastoplasticity is dominant, the strain parameter will be adopted. The concepts can also be distinguished by if they are based on a point, line, or area/volume. A point criteria is easiest to obtain, but are less detailed than line or area/volume criteria.

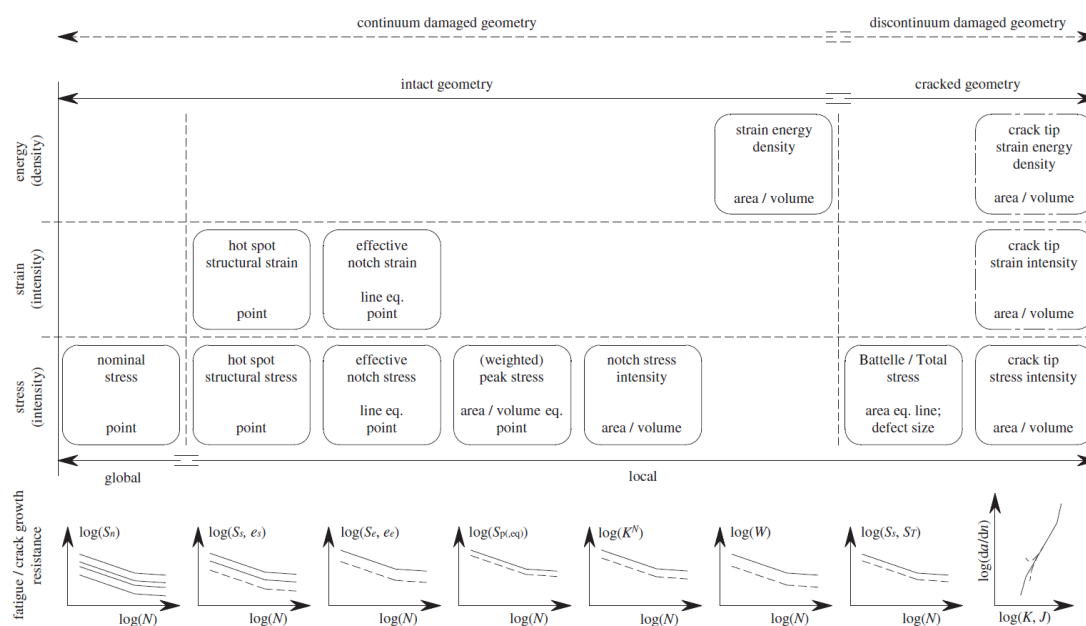


Figure 2.1: Overview of different fatigue concepts (den Besten, 2018)

The different concepts vary in accuracy in predicting the fatigue life of a specimen. One way to quantify the accuracy is via the strength scatter band index, denoted as  $T_{\sigma_s}$ . The strength scatter band index is calculated by dividing the fatigue strengths of the 10% and 90% probability of survival bands, for a certain number of cycles. If a method has a lower strength scatter, it means that the survival bands it produces are closer together, resulting in a lower value for  $T_{\sigma_s}$ . This lower  $T_{\sigma_s}$  value indicates that the method is more accurate. Scatter reduction can only be achieved up to a certain limit because fatigue strength exhibits considerable scatter even under constant amplitude loading in controlled laboratory conditions (Lassen et al., 2005). Another way to tell if a curve has more confidence is via a reduced fatigue lifetime scatter or fatigue lifetime standard deviation. The fatigue lifetime scatter is essentially the scatter on the x-axis, while the  $T_{\sigma_s}$  displays the scatter on the y-axis.

The following paragraphs will dive into different fatigue assessment concepts. These are different methods of calculating the stress that a structure is subjected to when loaded. These calculations are based on measurements that take place on the tested specimen. These measurements were often strain-based, using strain gauges or digital image correlation. Nowadays it is more common to perform finite element analysis (FEA), or both. At what location these measurements have to be done can vary with the different fatigue assessment concepts. For this thesis, no experiments will be performed, so mainly FEA will be used.

## 2.1. Nominal stress concept

The nominal stress concept (NSC) is an intact geometry approach, built upon a stress parameter criterion and the only approach adopting a global criterion with the nominal stress range  $S_n$ . Using this global information facilitates the need for a structural detail for each individual joint to include local information. Hence, each structural detail needs to have a unique fatigue resistance curve. However, this will lead to an infinite number of fatigue resistance curves, which is not practically feasible. That is why only the most common structural details have been classified.

These details, varying in geometry and size, are provided in fatigue classes (FAT) by the International Institute of Welding (IIW) (Hobbacher, 2016) and the fatigue categories (CAT) from the European Standard (NEN, 2012). Both sets include approximately 80 distinct details and employ a Basquin type of equation. The damage mechanism is assumed to be similar for all structural details, so the slope  $m$  does not change. The only changing variable is the intercept  $\log C$ , defining the position on the vertical axis of the fatigue resistance curve.

In cases where geometry, material, loading & response conditions, and environment align with the employed code, the results of the nominal stress concept prove to be quite sufficient, with limited computational efforts. That is one of the reasons why this method is the most widely used method in the marine industry (Liu et al., 2019). However, there are also some cons to this method. The fatigue resistance information in the fatigue classes and categories is obtained with constant amplitude (CA) testing. While marine structures are mainly subjected to variable amplitude loading, full accuracy can not be achieved, however a satisfactory can be made.

While the nominal stress concept permits the integration of localized information to a certain extent, it tends to falter when dealing with complex geometries beyond the scope of the collected joint data. Also, retrieving the nominal stress from a finite element (FE) calculation of a complex geometry could prove to be challenging as it is often unclear at which location the nominal stress needs to be obtained.

Figure 2.2 shows a fatigue test data scatter band, based on the nominal stress concept. It was created by Qin et al. (2019) in his research to prove the applicability of different fatigue assessment concepts to welded joints in steel structures. At the top of the figure, a strength scatter band index of  $T_{\sigma_s} = 1 : 2.29$  is given.

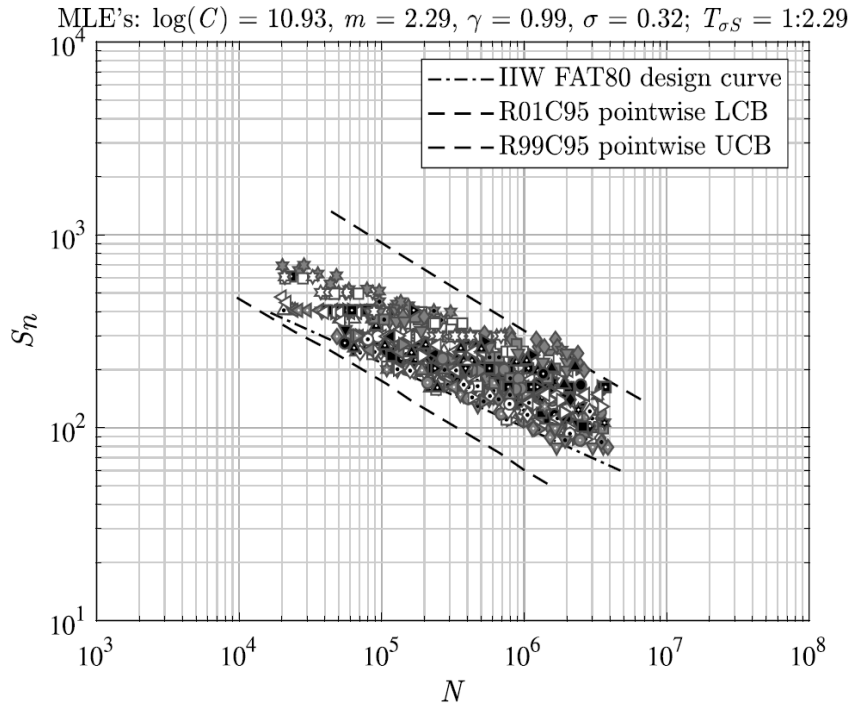


**Figure 2.2:** Nominal stress based small-scale data scatter band (Qin et al., 2019)

## 2.2. Hot spot structural stress concept

Like the NSC, the hot spot structural stress concept (HSSSC) is an intact geometry concept, based on a stress parameter criterion. But contrary to the NSC, the HSSSC includes local information about the structural detail, what local information is included depends on which stress calculation method is chosen.

There are different methods to calculate the stress at the hot spot (den Besten, 2021b; DNV, 2021a):

- Linear surface extrapolation through two points at certain distances away from the notch, can be  $0.4$  and  $1.0 t_p$  or  $0.5$  and  $1.5 t_p$
- Non-linear surface extrapolation through three points at a distance of  $0.4$ ,  $0.9$ , and  $1.4 t_p$  away from the notch.
- Stress evaluation at a location  $0.5 t_p$  away from the notch, multiplied by a factor of  $1.12$ .
- Stress evaluation at a sub-surface location of  $0.1 t_p$  below the surface, precisely at the notch.
- Through-thickness linearization of the nodal forces and moments of a shell/plate model, or achieving force and moment equilibrium of nodal forces in a cross-section of a solid model.

The choice of method is dependent upon the joint characteristics, such as geometry and hot-spot type. This method distinguishes two types of details, namely a load-carrying (LC) detail and a non-load-carrying (NLC) detail. This limits the amount of FAT classes and S-N curves to two. There are no clear-cut guidelines available for distinguishing whether a detail should be categorized as LC or NLC. An engineer needs to use their professional judgement to determine whether a detail should be classified as LC or NLC.

For T-joints and double-sided cruciform joints, the strength scatter band index  $T_{\sigma_s}$  actually increases compared to the NSC to a value of  $T_{\sigma_s} = 1 : 2.41$  (Qin et al., 2019). This can be explained by second-order bending stresses that are introduced in the  $S_s$  data because of non-symmetry in double-sided T-joints. This second-order bending stress is not accounted for in the NSC, so that is why the strength scatter band index could increase.

To summarize, the hot spot structural stress concept is an intact geometry concept based on a stress

criterion. It can include local geometrical variations, to solve the "local" nominal stress issue. Only two FAT classes are needed, for LC and NLC details, a great improvement compared to the NSC. These advantages come with some downsides. For example, the requirement for an engineering judgement arises, giving the method user variations. Also, the complexity of the method increases compared to the NSC.

## 2.3. (Averaged) Effective notch stress concept

The effective notch stress concept (ENSC) is, like the HSSSC, an intact geometry concept, based on a stress parameter criterion and including local information. The concept involves representing the real weld geometry along with the resultant stress distribution across the weld notch's thickness. This is achieved by either utilizing solid modeling to capture the genuine geometry or by averaging the actual through-thickness weld notch stress distribution (using a semi-analytical expression) across a characteristic depth. As a result, this approach addresses all the concerns raised against the original NSC, albeit requiring more intricate modeling and additional effort.

The existence of a notch creates the notch effect, an increased stress concentration at geometric discontinuities. The notch radius is usually minimal ( $\rho \rightarrow 0$ ), and the theoretical stress concentration is not in full effect. This implies that considering a peak stress in zone 1 as the fatigue damage criterion, where  $S_{max} = \sigma_{max}$ , would be excessively conservative (den Besten, 2018). An effective notch stress estimate ( $S_e = \Delta\sigma_s$ ) can be obtained via three main proposals:

- Adopting the stress value ( $\Delta\sigma_e$ ) at a material characteristic micro- and mesostructural distance  $\rho^*$  from the notch (Peterson, 1938).
- Taking the average of the stress distribution ( $\Delta\sigma_{av}$ ) around the notch along the presumed crack path across a material-specific micro- and meso-structural length  $\rho^*$ , see equation (2.1) (Neuber, 1937). This method is also called the averaged effective notch stress concept (AENSC).

$$\sigma_{av} = \frac{1}{\rho^*} \int_0^{\rho^*} \sigma_n(r) dr \quad (2.1)$$

- Adopting the notch stress range ( $\Delta\sigma_{max}(\rho_e)$ ), acquired with an artificially enlarged effective notch radius  $\rho_e$ , obtained with equation (2.2) (Sonsino et al., 2012).

$$\rho_e = \rho + s \cdot \rho^* \quad (2.2)$$

To account for the notch and its geometry in an FE model, the weld seam needs to be modeled with much detail. Typically, a solid FE solution is required to obtain an effective notch stress estimate. However, the analytical weld notch stress distribution formulation can also be used (den Besten, 2015).

Qin et al. (2019) applied the AENSC methodology to T-joints and double-sided cruciform joints, resulting in a strength scatter band index of  $T_{\sigma_s} = 1 : 1.52$  demonstrating a notable reduction in scatter when contrasted with the outcomes obtained from the NSC and HSSSC approaches.

In summary, the ENSC is an intact geometry concept based on a stress criterion. It can include local geometrical variations and size effects to improve the accuracy of the method. Also, the number of FAT-classes has been reduced to only one, based on a reference notch radius. This comes with the downside that the method has an increased complexity when compared with the NSC and HSSSC.

## 2.4. Total stress concept

The total stress concept (TSC) is, contrary to the previous concepts, a cracked geometry concept. It was proposed by den Besten (2015) in his PhD thesis, to further increase the fatigue strength similarity and thus reduce the strength scatter band index. A cracked geometry is validated, based on the assumption that the fatigue life is primarily spent in the crack growth period, due to welding-induced flaws and defects. Because the method is based on a cracked geometry, a stress intensity factor (SIF) is adopted.

The SIF, denoted as  $K$ , characterizes the amplitude of linear elastic stress at an infinitely sharp crack tip. For weld toe notches, represented as infinitely sharp cracks, this concept is mathematically represented in equation (2.3). Here,  $K$  corresponds to the stress intensity factor, where  $Y_n$  and  $Y_f$  denote the crack length-dependent notch and far-field factors, respectively (den Besten, 2015).

$$K = \sigma Y_n Y_f \sqrt{\pi a} \quad (2.3)$$

Comparisons between the four models show the smallest strength scatter band index for the TSC (den Besten, 2015; Qin et al., 2019). A strength scatter band index of  $T_{\sigma_s} = 1 : 1.47$  is achieved.

To sum up, the TSC is the only concept based on a cracked geometry. Therefore, it uses a stress intensity factor, here denoted as  $K$ . The concept, with short and long crack factors including local information, offers the least scatter among all the aforementioned concepts.

## 2.5. Concluding remarks

This chapter presents four fatigue damage criteria for steel structures, the nominal stress concept, hot spot structural stress concept, (averaged) effective notch stress concept, and the total stress concept. The concepts vary in terms of the extent of local information incorporated within the concept and in the methods used to achieve the desired stress values, with one method being more complex than the other. One noticeable trend is the exchange of simplicity for accuracy, with the TSC being the prime example as it gives the highest accuracy while also being the most complex.

For the current assessment, a fitting fatigue damage concept needs to be selected. Despite the TSC providing the highest accuracy, the ENSC is considered the optimal selection when evaluating the problem statement and the restricted time frame.

# Small- and large-scale specimen fatigue resistance similarity

Section 3.1 will cover the fatigue resistance of small-scale specimens, section 3.2 the fatigue resistance of large-scale specimens and section 3.3 the loading & response conditions for full-scale structures. Section 3.4 covers the scale effects that arise when scaling from small- to large- to full-scale and concluding remarks are given in section 3.5.

## 3.1. Small-scale specimen fatigue resistance

Results from fatigue tests are used to establish S-N curves. S-N curves are used for predicting the fatigue life of structures adopting a stress amplitude (S) to number of cycles to failure (N) relationship. This relationship is usually displayed on a logarithmic scale, with S on the y-axis and N on the x-axis. The curve typically takes the form of a smooth linear line, although it consists of discrete data points that come from fatigue tests.

The data points consist of a stress range on the vertical axis and a number of cycles to failure on the horizontal axis. The stress range represents the stress range on which the specimen was tested to failure. The stress range can be calculated as the difference between the maximum and minimum stress levels the specimen is subjected to during a load cycle. For a constant amplitude (CA) fatigue test, the stress range and amplitude will stay constant for the entirety of the fatigue test. The fatigue test continues until failure in the material or welded joint. This number of cycles to failure N is plotted on the horizontal axis and can range from a few cycles to tens of millions.

S-N curves often include a (near) horizontal line in the HCF range. This line represents the fatigue limit. The fatigue limit is the stress amplitude below which the material can theoretically endure an infinite number of cycles without failing. The S-N curve approaches infinity for that stress range and lower. Because the fatigue limit is often based on run-outs, specimens that have not failed at the end of testing, the existence of a fatigue limit can be questioned (Pyttel et al., 2011). Rather than stating that the material can endure an infinite number of cycles, it can be expressed that there is not sufficient time to conduct tests for an infinite number of cycles. The issue is more related to an insufficient amount of HCF test data.

Even though the fatigue limit cannot be a general material property (Pyttel et al., 2011), it is still a good estimation of a change in fatigue behavior in the HCF. This change in fatigue behavior is visualized by a change in the slope of the curve. The slope of the S-N curve indicates the material's sensitivity to cyclic loading. Materials or welded joints with steeper slopes are more sensitive to a change in cyclic loading level, while shallower slopes are an indication of less sensitivity. The slope can vary depending on the material's microstructure or other mechanical properties. Figure 3.1 shows some S-N curves with a double change in slope. Not only at the fatigue limit but also at the start of the HCF range. This demonstrates a change in fatigue behavior as the stress range decreases.

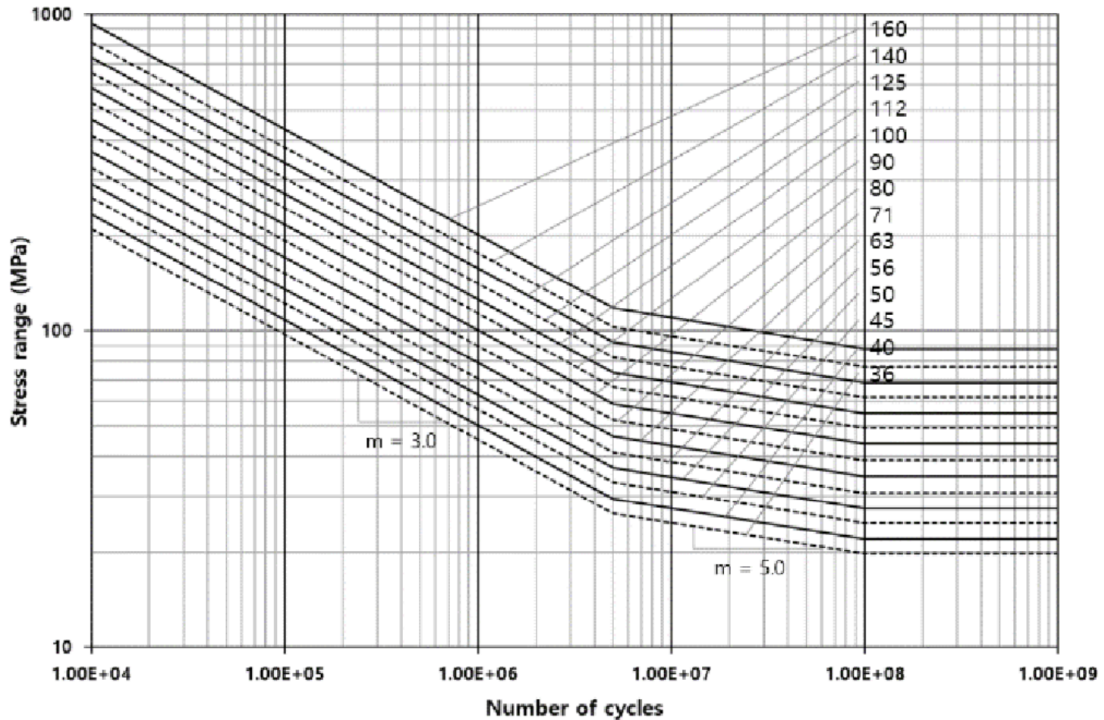


**Figure 3.1:** Example of a double S-N curve (Sungwoo et al., 2021)

The S-N curve is a line that is fitted through the data points and thus represents the average behavior of the specimens. And for design S-N curves it is the average minus two times the standard deviation (NEN, 2012). So these curves include statistical aspects from the data set. However, there is often scatter or variability in the data. In many cases, extreme outliers are removed to reduce their influence on the S-N curve. However, scatter and variability will still be present in the curve, because for a given stress amplitude, fatigue tests conducted on identical material specimens still have a different number of cycles to failure (Lassen et al., 2005), emphasizing the complexity of fatigue behavior. To mitigate the risks associated with scatter and variability, probabilistic models are employed to estimate the probability of failure over a design life.

Another aspect to consider is the effect the load ratio has on the fatigue life and thus the S-N curve. The load ratio ( $R$ ) signifies the relationship between the minimum stress and the maximum stress experienced during a load cycle. The relationship is visualized in equation (3.1).

$$R = \frac{\sigma_{min}}{\sigma_{max}} \quad (3.1)$$

When assessing fatigue behavior, the influence of the stress ratio is known and not something to be overlooked as the material can exhibit different responses to cyclic loading based on the stress ratio (Klevtsov et al., 2008; Schijve, 2009). A visualization of a stress cycle is given in figure 3.2. When  $S_m$  equals zero, a stress cycle divides its time equally between tension and compression stresses. These would be ideal circumstances with no mean stress present in the tested material. However, if  $S_m$  rises while  $S_a$  remains constant, then  $S_{max}$  will increase. As a result, a larger stress is present to open micro- or macrocracks and a shorter fatigue life and a lower fatigue limit should be expected. Even if  $S_a$  does not remain constant and  $S_{max}$  remains the same, if  $S_m$  increases, more time is spent in the tensile stress region which negatively affects the fatigue life of a specimen.

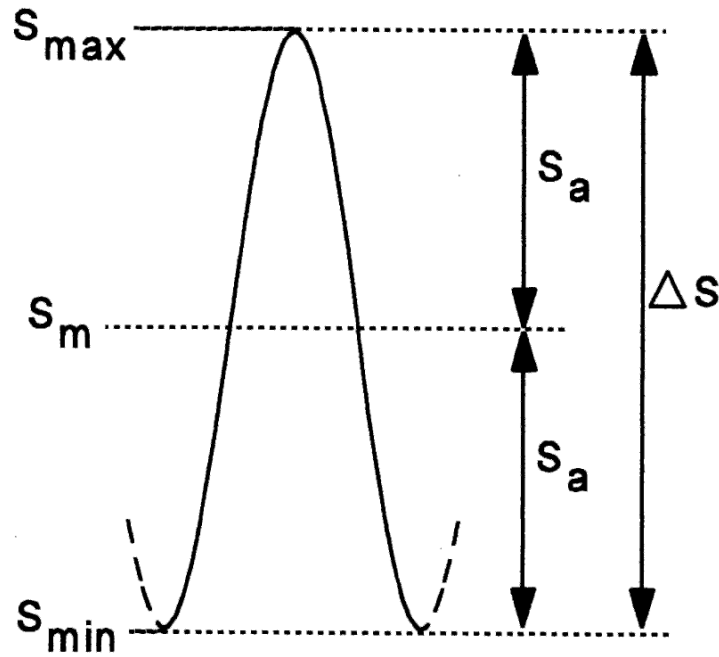


**Figure 3.2:** Characteristic stress levels of a load cycle,  $S_{max}$  = maximum stress level,  $S_m$  = mean stress level,  $S_{min}$  = minimum stress level,  $S_a$  = stress amplitude,  $\Delta S$  = stress range (Schijve, 2009)

Results from fatigue tests with a low load ratio ( $-\infty < R \leq 0$ ) often show better fatigue performance than results from fatigue tests with a high load ratio ( $0.5 \leq R$ ) on identical specimens. So when evaluating data points in an S-N curve, it is important to know the corresponding load ratio. Figure 3.3 shows a side-by-side comparison of a small-scale specimen fatigue data scatter band by Qin et al. (2019). On the left is the scatter band without any load ratio corrections, while on the right the stress range has been translated to  $R = 0.5$  by means of the correction model by Walker (1970). It can be seen, by the eye and the strength scatter range index  $T_{\sigma S}$ , that the scatter has been reduced when applying a correction model.

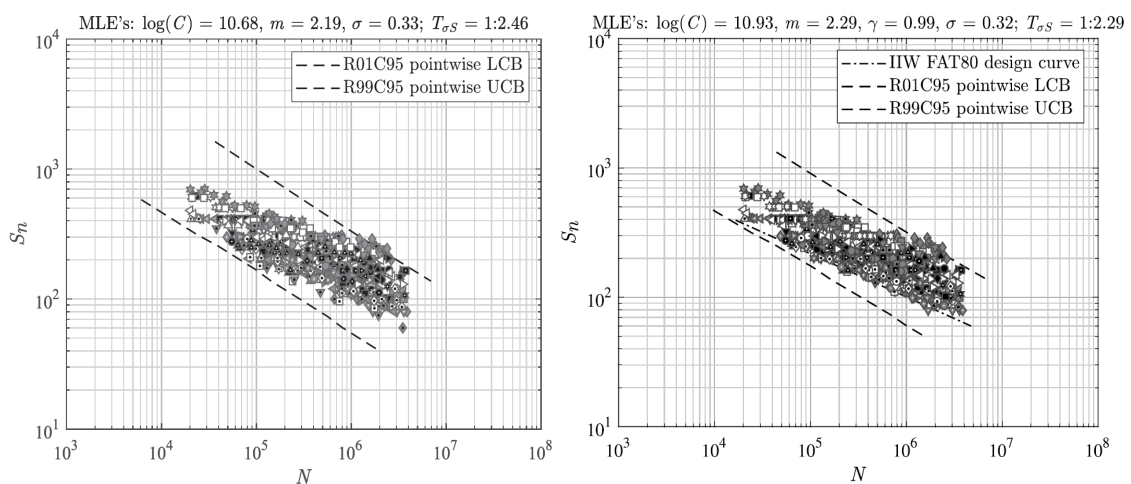


**Figure 3.3:** Nominal stress small-scale specimen data scatter band without (left) and with (right) mean stress correction (Qin et al., 2019)

The small-scale specimen database used in figure 3.3 is from Qin et al. (2019) and consists of double-sided T-joints, and double-sided cruciform-joints. Work on the database has continued and is now filled with

around 2600 specimens and also includes butt joints, cover plate joints, and gusset plate joints (Qin et al., 2021). The base plate thicknesses in the database vary from 2 to 160 mm. Loading and response ratios range from -1 to 0.8 and the yield strength is between 245 and 1030 MPa. The applied load is either a (3- or 4-point bending) bending moment or a normal force. The fatigue life times  $N$  cover the MCF and HCF region. With all these variations, this is a representative database for the most common types of connections and loading.

Small-scale tests serve as fundamental building blocks in the study of fatigue behavior due to their practical feasibility and ease of execution compared to large-scale tests. These smaller tests allow for easy exploration and establishment of critical assumptions about material properties and structural responses under cyclic loading conditions. Caution needs to be taken when extrapolating results from small-scale tests to large- and full-scale structures.

## 3.2. Large-scale specimen fatigue resistance

Moving from small-scale specimens to large-scale structures, the evaluation of fatigue resistance takes on a new dimension. The behavior of materials under cyclic loading in full-scale components often reveals different characteristics and challenges. Different characteristics certainly come to light when addressing tubular and planar configurations.

### 3.2.1. Tubular structures

Recent developments in the space of marine renewable energy systems have led to challenges for the design and construction of steel tubular structures to be cost-efficient while safeguarding structural safety (Papatheocharis et al., 2020). Thus, bringing attention to the fatigue behavior of tubular welded structures, which differs from stiffened panel-type configurations. Figure 3.4 displays an array of types of tubular joints.

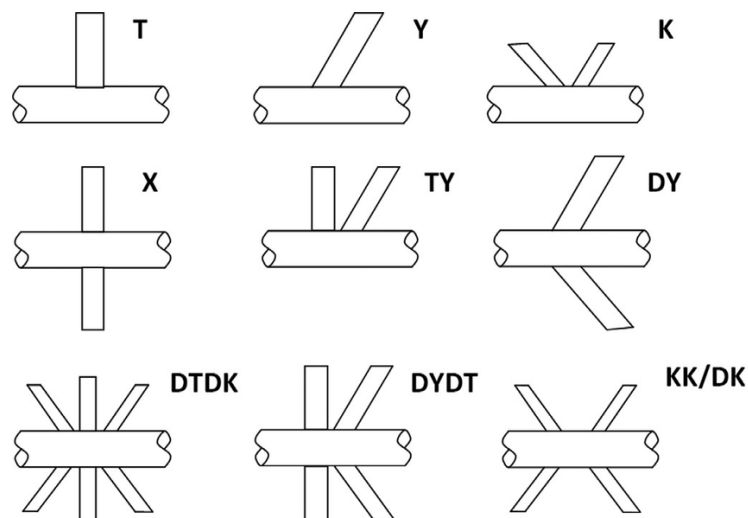


**Figure 3.4:** Types of tubular joints (Saini et al., 2016)

Tubular structures can be single-planar, but multi-planar as well. Single planer tubular structures often experience more predictable stress distributions, leading to more predictable failure modes and fatigue (damage) assessment. The stress distribution becomes more complex in multi-planar tubular structures when forces are applied in multiple directions. The fatigue life and failure modes become more intricate, making fatigue design and assessment more challenging.

Tubular structures have varying cross-sections. While circular cross-sections are common, non-circular cross-sections also exist. A circular shape offers a more uniform stress distribution. This characteristic often leads to better fatigue resistance due to the absence of stress concentrations that arise with sharp edges or sudden changes in geometry. Non-circular cross-sections can introduce stress concentrations

due to their geometric irregularities. These stress concentrations might occur at corners, edges, or geometric changes and can impact the initiation and propagation of fatigue cracks.

The tubular configurations have hollow intersections, which change the loading & response characteristics. In tubular structures, the bending stiffness is affected significantly. The outer edges, being further away from the neutral axis, contribute more to the structure's overall bending stiffness. However, the transition from one section to another can lead to stress concentrations, making the weld stiffness very important for tubular structures. When modeling tubular structures, much effort needs to be spent in modeling the weld geometry to ensure its correctness. However, this thesis will focus on planar-type configurations only.

### 3.2.2. Planar structures

Marine vessels predominantly consist of planar structural configurations, which show different fatigue behavior compared to tubular structures. Figure 3.5 shows a typical stiffened panel configuration, consisting of a base plate with stiffeners, transverse frames, and longitudinal girders. Transverse bulkheads can be envisioned at either end of the depicted plate. In a stiffened panel, the arrangement and hierarchy of the structural elements play a key role in the (fatigue) strength of the panel. The hierarchy refers to the organization and relationship between the structural members. The panels are the primary load-bearing elements forming the outer surface of the structure. They experience direct loading and transfer these loads to the stiffeners and frames. The thickness of the plate greatly impacts the overall stiffness of the structure. The stiffeners are longitudinal members attached to the plate to enhance the load-carrying capacity, transfer loads to the frames, and increase the stiffness of the panels. Transverse frames are placed perpendicular to the stiffeners to increase the transverse stiffness.

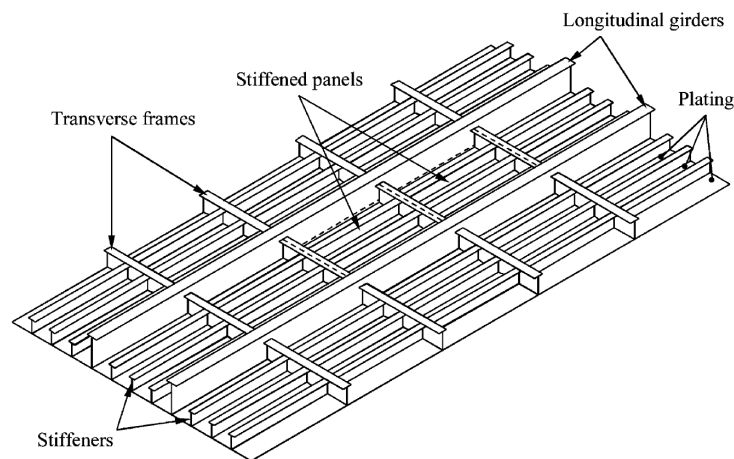


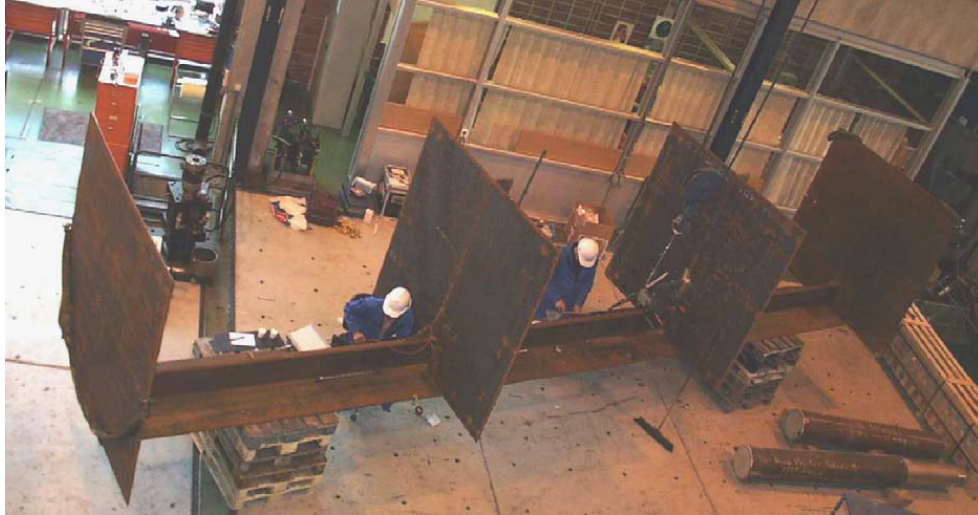
**Figure 3.5:** An example of a typical stiffened panel (Paik et al., 2002)

The hierarchy ensures that loads are efficiently distributed throughout the structure, minimizing stress concentrations and preventing localized fatigue-prone areas. This helps to improve the overall fatigue resistance of the structure. The hierarchy also affects the propagation of fatigue cracks. A well-organized structure may slow down or divert crack propagation, extending the structure's fatigue life.

With all the different structural members comes a range of connections that can be investigated. Numerous stiffeners result in a significant amount of plate-stiffener connections. The transverse frames crossing with the stiffeners results in a large amount of frame-stiffener connections. The last connection of interest is where two frames meet each other and form a frame-frame connection. These welded connections are interesting from a fatigue point of view since welds often induce defects which are locations prone to fatigue cracks. The stiffness of a planar structure is lower compared to a tubular structure, meaning that the weld stiffness is less important and modeling can be done with less detail.

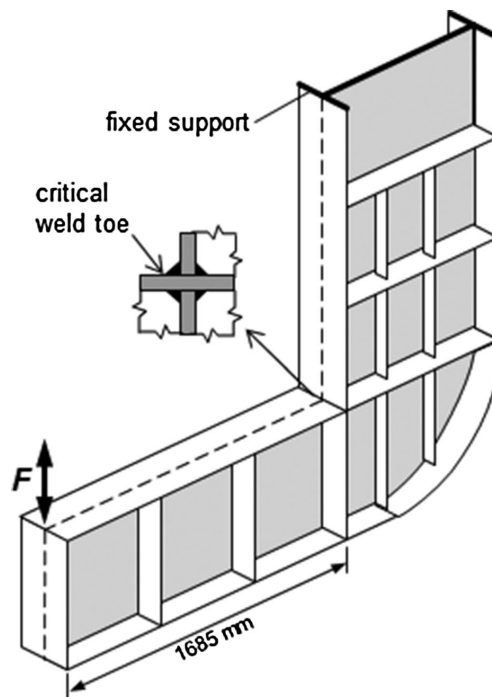
### 3.2.3. Large-scale fatigue tests

Because of the limitations of testing full-scale structures, the most representative fatigue tests are tests on full-scale representative large-scale specimens (LSS). These are tests not on one structural member but on a system of members. Literature provides a diverse range of these tests. Figure 3.6 displays a large-scale fatigue test of a side-longitudinal. The locations of interest are the frame-stiffener connections at the top of the stiffener.



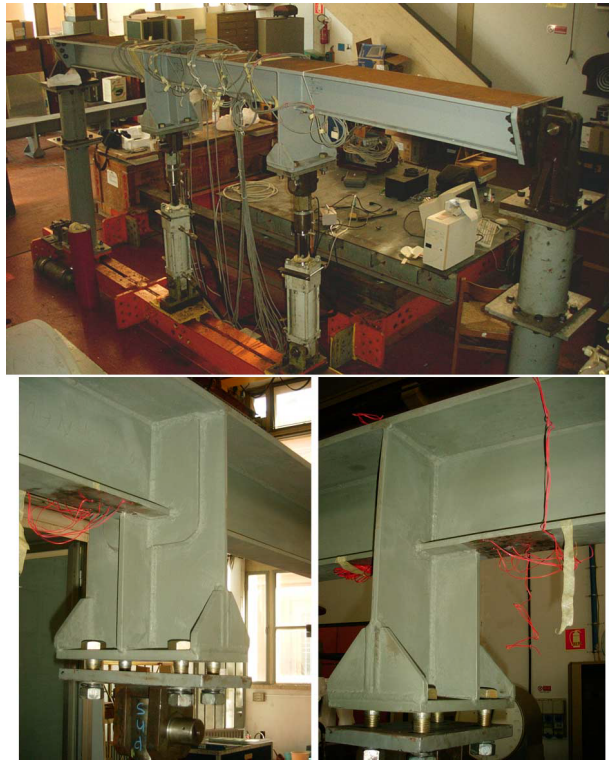
**Figure 3.6:** Large-scale specimen of a side-longitudinal (Lotsberg et al., 2005)

Figure 3.7 present the (schematic) LSS that was investigated in the papers from C. Fischer et al. (2018), Kozak (1999), and Kozak et al. (2015). The specimen is the bilge corner of a Ro-Ro ship and the figure also displays the loading location and the fixed support. The point of interest is depicted as the critical weld toe and is where a frame-frame connection is made.



**Figure 3.7:** Large-scale specimen of a bilge corner (C. Fischer et al., 2018)

In the paper by Rizzo et al. (2007), a T-shaped longitudinal stiffener, shown in figure 3.8, is examined. The locations of interest are shown in the bottom half of the figure. These locations are where the stiffener is connected to a frame. The specimen was tested via 4-point bending and was expected to fail at the frame-stiffener connections.



**Figure 3.8:** Large-scale specimen of a T-shaped longitudinal stiffener (Rizzo et al., 2007)

Examinations of LSS are way less common than tests on SSS and a big portion of LSS tests are not from recent times. The fatigue assessment approach applied in these studies is notably influenced by the time at which the tests were conducted, with the more advanced concepts not being applied in the older fatigue tests. The LSS from literature can be recreated in FE software to perform stress calculations that have not been conducted in the original research. The created FE models can be used in this research to examine the influence of different fatigue assessment concepts.

### 3.3. Full-scale structure fatigue loading & response

Instead of conducting impractical fatigue tests or waiting over two decades for a crack to initiate, full-scale structures are assessed via loading and response. The main purpose of conducting full-scale structure loading and response assessment for ships is to ensure their resilience and durability and load distribution behavior is as expected under various operational conditions. It helps in understanding how a structure responds to dynamic loads like waves, wind, cargo weight, and various environmental conditions throughout its service life.

For accurate load and response measurements, hull monitoring systems (HMS) can be installed in new or existing vessels. HMS can include but are not limited to (Magoga et al., 2019):

- accelerometers;
- strain-gauges;
- torsionmeters to measure shaft power;
- an inertial six-degree of freedom rigid body motion reference unit;
- an external global positioning system.

With the HMS in place, a vessel can undergo sea trials or start its service life. With different loading conditions with various speeds, maneuvers, and wave impacts data can be collected. Data collected from the sensors is analyzed to understand how the ship's structure responds to different loads and environmental factors.

By evaluating structural responses, the assessment ensures that vessels can withstand the expected loads during the operational lifespan, minimizing the risk of structural failure. Insights gained from the assessment can be used to optimize ship design, making them more robust and fatigue-resistant, enhancing performance and longevity. The assessment helps in identifying potential fatigue hotspots and critical areas within the ship's structure that are prone to fatigue-induced damage due to cycling loading. Following this, strategies can be devised to reinforce these areas, select appropriate materials, or adjust operational practices to enhance the vessels fatigue resistance (Ibrahim, 2015).

This thesis focuses on the examination of large-scale specimens, like those examined in papers such as Fricke et al. (2010), Kozak et al. (2015), and Rizzo et al. (2007), which delve into the fatigue life testing of full-scale representative large-scale specimens. To replicate real-world conditions, these specimens are exposed to loads designed to mimic real-world operational scenarios, and these loads are applied in a controlled laboratory environment. Here lies the advantage for this thesis, as the loads are known they are able to be replicated in FE modeling. The advantage lies in the precise knowledge of the applied force, the application point(s), and the boundary conditions, which facilitates the determination of loading conditions for FE modeling. However, difficulties could certainly arise in FE modeling to perfectly recreate the large-scale specimen as they could include complicated shapes or connections.

### 3.4. Scale Effects

The foundation for designing full-scale structures relies on the results obtained from tests conducted on small-scale specimens. This emphasizes the need to carefully assess the scale-related effects that emerge during the transition of data from small-scale specimens to full-scale structures. (Sonsino et al., 2005; Zhu et al., 2021). Scale effects can be classified into three categories:

- 1 Statistical scale effects
- 2 Geometrical scale effects
- 3 Technological scale effects

This paragraph will address the various categories. Subsection 3.4.1 explains the scale effects that originate from a statistical standpoint. Subsection 3.4.2 will examine how increasing size leads to scale effects, Subsection 3.4.3 will delve into the scale effects that originate during production or manufacturing. Finally, section 3.5 draws conclusions from this section.

#### 3.4.1. Statistical scale effects

Firstly, this section will touch on the statistical scale effect that is introduced when scaling from small-scale specimens to large-scale specimens. The statistical scale effect can be interpreted in multiple ways. On one side there is an increase in the number of defects when enlarging a specimen, which negatively impacts the fatigue strength. This will be explained first. Furthermore, there is the aspect of (un)certainly with the amount of fatigue test data. A higher number of data points contributes to a more reliable S-N curve. This topic will be addressed in the subsequent paragraph.

##### **Weakest link**

As the dimensions of a specimen increase, the likelihood of encountering large defects within its geometry increases accordingly. These defects can be of many sizes, but there is a limit due to inspection and quality standards. The relationship between an increase in size and has been empirically demonstrated, such as in the case of longer wires, where it has been observed that their capacity to bear weight diminishes with an increase in size (Alava et al., 2009; Makkonen, 2001). Figure 3.9 displays this phenomenon.

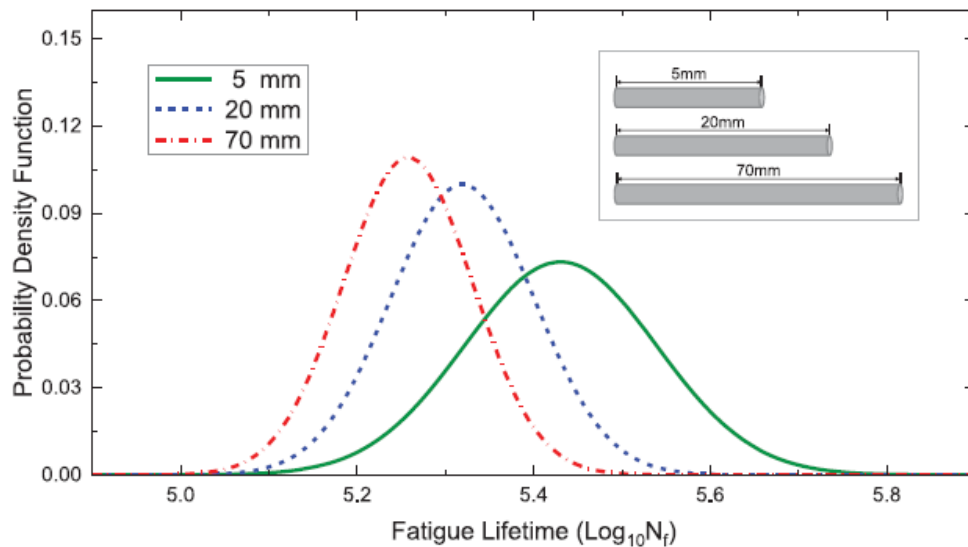


**Figure 3.9:** Failure probability density function of cables with different lengths (Heckel et al., 1975)

This behavior can be attributed to discontinuities present within the material, a characteristic that contributes significantly to the statistical scale effect. The concept underlying this phenomenon aligns with the weakest link argument, wherein the failure strength of an object is primarily determined by the characteristics of its weakest local sub-volume. Hence, in larger samples, the likelihood of such a vulnerable area being present becomes more substantial, underlining the observers' reduction in fatigue capacity. Figure 3.10 visualizes the weakest link theory. Imagine that some material containing a severe defect (red) is used to make one large specimen. Then it will necessarily contain the severe defect and, when tested, it will show low fatigue strength. If instead six small specimens were made from the same material, only one of them will contain the severe defect. Thus, when testing, only one of the results will show low fatigue strength, while the other five will show much higher fatigue strength (Pedersen, 2019).

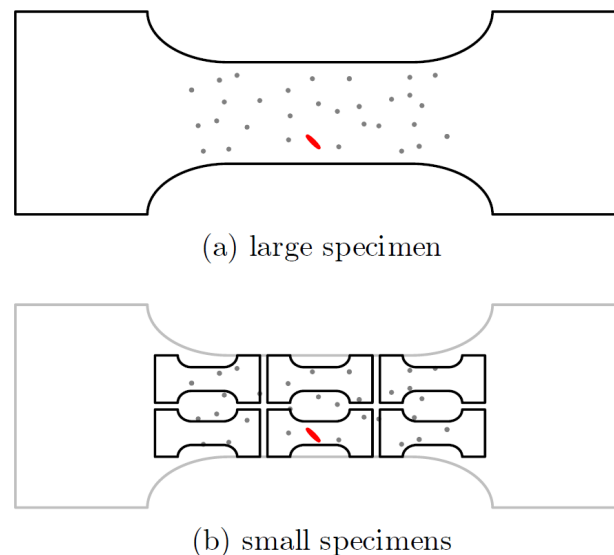


**Figure 3.10:** Visualization of the weakest link argument (Pedersen, 2019)

Tomaszewski (2018, 2020) and Tomaszewski et al. (2014) conducted research that delved into mini specimens to measure the scale effects when transitioning from mini to small-scale specimens. Figure 3.11

and table 3.1 show respectively the geometry and the dimensions of the standard and mini specimen.

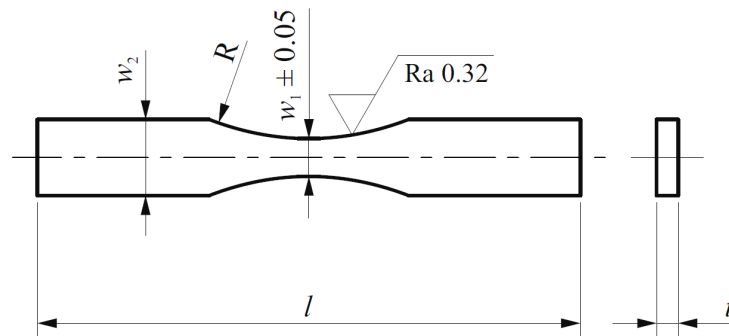


**Figure 3.11:** Geometry of the mini and standard specimens (Tomaszewski, 2018)

**Table 3.1:** Specimen dimensions

Type of geometry	$t$ [mm]	$w_1$ [mm]	$w_2$ [mm]	$R$ [mm]	$l$ [mm]	$V$ [mm <sup>3</sup> ]
Standard specimen	4	7	14	25	100	5117
Mini specimen	1.4	2.5	5	18	35	214

The research confirmed the expected outcome that the mini specimens would exhibit a greater fatigue strength compared to their larger counterparts. Results from the mini and standard specimen tests are shown in figure 3.12.

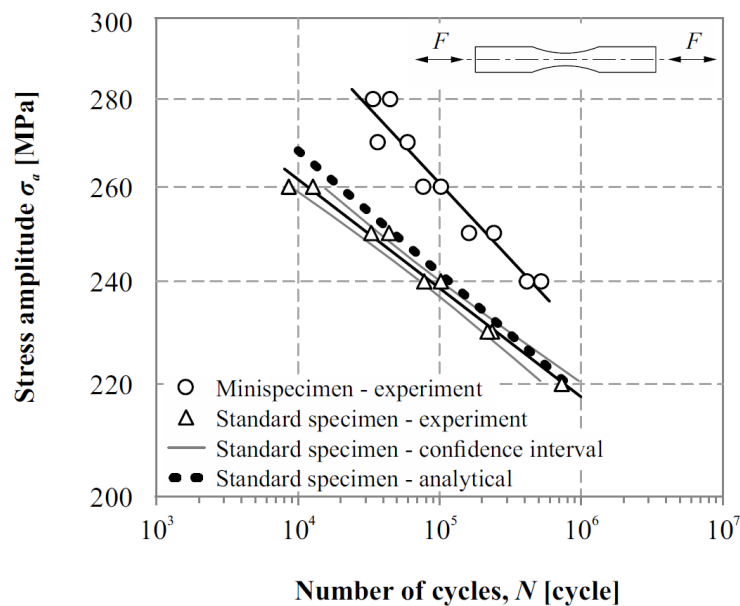


**Figure 3.12:** Fatigue data for mini and standard specimens (Tomaszewski, 2018)

Another phenomenon that falls under the statistical weakest link theory, is the thickness effect. In general, the fatigue strength decreases with an increased plate thickness, due to an increased chance of large defects (Pedersen, 2019). However, the notch effect, explained in Subsection 3.4.2, also contributes due to a change in the stress gradient. This effect is mostly negated by testing small-scale specimens that have similar thicknesses to real-world structures. The small-scale database covered in section 3.1 covers

a wide range of plate thicknesses. So it can be concluded there are no substantial differences between plate thicknesses of small-scale test specimens and full-scale structures.

As described earlier, welds are highly susceptible to fatigue crack initiation. "An analysis carried out on the test results reveals the relationship between increasing length of the weld, as well as dimensions of welded element, and decrease in fatigue durability. Such an effect is called the volume effect" (Blacha et al., 2013). In their research, Blacha et al. (2013) proposed a non-local probabilistic computational model for fatigue life assessment of welded joints.

For an element with an inhomogeneous stress field  $\Delta\sigma(x, y, z)$ , the proposed failure probability distribution  $P_f$  is shown in equation (3.2). The formula is defined through four parameters. Fatigue parameters for efficient material  $C_f$  and  $m_f$ , referential volume  $V_0$ , and shape parameter  $p$ . The process of identification of these parameters is presented in appendix A.1. Plots displaying the sensitivity of the weld volume to the stress range and number of cycles are also in appendix A.1.

$$P_f(N) = 1 - P_s(N) = 1 - e^{-\frac{1}{V_0} \int_V \left( \frac{\log N}{\log C_f - m_f \log \Delta\sigma(x, y, z)} \right)^p dV} \quad (3.2)$$

The proposed model shows that the statistical characteristics of fatigue durability rely on various material and geometry-related variables and that scaling from small-scale to a larger scale has a negative impact on the fatigue life.

### Sample size

Another way of looking at the statistical size effect is with respect to database size. S-N curves are based on failure data points, obtained with fatigue resistance tests. With an increase of those data points or sample size, S-N curves show a rapid convergence and an increase in confidence (Beretta et al., 1995; DNV, 2021b). This raises the question of how many tests are needed for a viable fatigue assessment.

It is hard to find a definite answer, but the sample size should be sufficient to account for the following principles. To begin, a larger sample size enhances the statistical significance of a curve, ensuring that the curve's outcomes carry genuine meaning rather than being subject to random chance (Sumeracki, 2018). As mentioned, a larger sample size increases the reliability and confidence of a curve. Next, with a larger sample size a curve is more likely to be applicable to a broader range of situations and materials. Lastly, a larger sample size allows for a better data quality assessment. It helps identify data anomalies, outliers, and errors leading to a more accurate and reliable curve.

For this thesis, the sample size relates to the number of large-scale models that will be created. The goal is to create a data set with sufficient size from which conclusions can be drawn. If only one large-scale model is created, it is nearly impossible to draw conclusions. Hence, the decision has been made to create as many large-scale models as is reasonably achievable within the allocated time frame.

### 3.4.2. Geometrical scale effects

The next scale effects can be categorized as geometrical scale effects. They address the effects arising from geometric variations that become apparent when scaling from small-scale to large-scale. First is the notch effect, a change in stress gradient reducing the fatigue limit and strength. Next is the principle of load path redundancy. As the specimen size increases, there is also an increase in the amount of excess material. Material that can withhold additional stress when other components of the structure experience failure. This generally leads to an increase in fatigue life.

#### Notch effect

The geometrical notch effect is observed when a material has certain irregular shapes that influence how stress is distributed. Figure 3.13 provides an illustrative example showcasing the notch effect. The two notched specimens have consistent shapes, but specimen 1 is larger compared to specimen 2. Both specimens demonstrate similar patterns in internal and external stress distribution, and the peak stress, denoted as  $\sigma_{max}$ , remains identical. If a crack of length  $a_0$  is considered in both notches, it can be observed that the stress cycle at the crack tip is higher in the larger specimen, denoted as  $\sigma_1$ . This elevation in

stress implies a corresponding increase in the stress intensity factor range. Consequently, it results in a lower resistance to fatigue for the specimen with increased size (Liao et al., 2020; Makkonen, 2003).

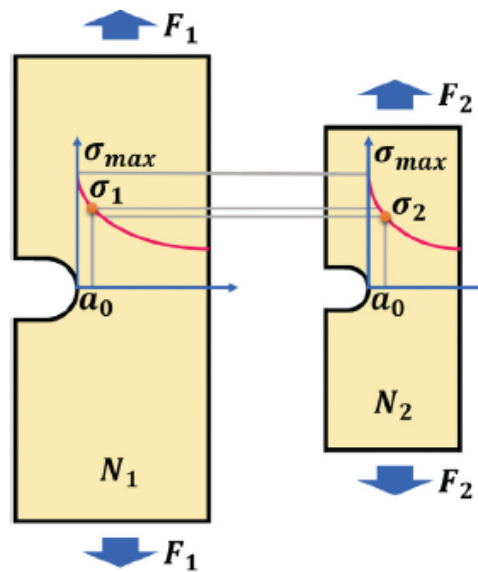


Figure 3.13: Notch size effect (Liao et al., 2020)

However, the ENSC accounts for this effect. When taking the average stress over the presumed crack path, the notch effect is encompassed in the ENSC. Thus comparing the ENSC to a concept that does not account for the notch effect could be an effective way to gather information on the influence of the notch effect.

#### Load path redundancy

Another geometrical size effect that originates when scaling from small- to large-scale specimens, is load path redundancy, or structural redundancy. Structural redundancy refers to the (intentional) inclusion of excess structural elements within the design of a structure. These additional components serve as backup load paths, to ensure that a structure can continue to function safely even if certain elements fail or become damaged, therefore it is a desired capability of all structures that have to be reliable in service (Blagojević et al., 2008). In essence, structural redundancy provides a safety net by distributing loads more evenly across the structure, reducing the risk of sudden and catastrophic failure due to a single point of weakness (Hendawi et al., 1994; Nikolaidis et al., 1990; Stiansen, 1984).

Structural redundancy can have a profound impact on fatigue strength. The presence of redundancy allows a structure to better withstand fatigue-related stresses. When cyclic loads are applied, the redundant elements can help distribute these loads across multiple paths. Redundancy is a desirable property of a structural system and often structures are designed to have redundancy (Fang et al., 2011). However, structural redundancy typically becomes evident when examining an entire structure. When evaluating a welded joint on a local level, redundancy has little to no impact on the result of the local assessment. Surrounding material is not relevant when applying concepts including sufficient local information, such as the effective notch stress concept. However, this does not mean that it does not affect the results of a fatigue test when looking at the number of cycles to failure. Small-scale specimens have few redundant load paths so when a crack initiates, it will almost certainly fail soon after. After crack growth, it will soon propagate through the entire specimen. This is different in comparison with large-scale specimens. Larger specimens have redundant material through which the load paths can be distributed after a crack initiates. The crack growth process will also take longer since stresses can be redistributed. This will lead to better results in fatigue tests for large-scale specimens.

### 3.4.3. Technological scale effects

The final category of scale effects that can be identified are the technological scale effects. These are scale effects that are introduced when the material is produced, transported, or processed. Small-scale specimens can also experience these effects, but generally to a lesser extent than large-scale specimens. Firstly, there is the surface roughness. Larger specimens are generally rougher and are experiencing a loss of fatigue life because of it. Next, the introduction of residual stress when structures are produced. Residual stresses can have either a negative or positive impact on the fatigue strength of a structure.

#### Surface roughness

Surface roughness relates to the microscopic geometric features, including small gaps, peaks, and valleys on a machined steel sheet. Surface roughness results from the way the material is processed. Examples include the friction between the tool and the metal surface, the reshaping of the metal's surface layer when chips are removed, and the vibrations occurring in the processing system (YPI, 2020).

As aforementioned, surface roughness indicates that the exposed surface is not entirely flat, it has microscopic peaks and valleys. As a result, mSCs emerge at the material surface, promoting crack nucleation at the material surface. Since fatigue cracks generally initiate on the specimen surface, it is known that the surface roughness of a specimen has a great effect on its fatigue strength (Alang et al., 2011). Figure 3.14 shows an S-N diagram for different surface roughnesses. Here the decrease in fatigue strength is visualized for an increase in surface roughness. In the low cycle fatigue range, the effects of surface roughness are noticeable but do not cause big variability (W. Xiao et al., 2012). For mid- and high-cycle fatigue, more and more scatter appears.

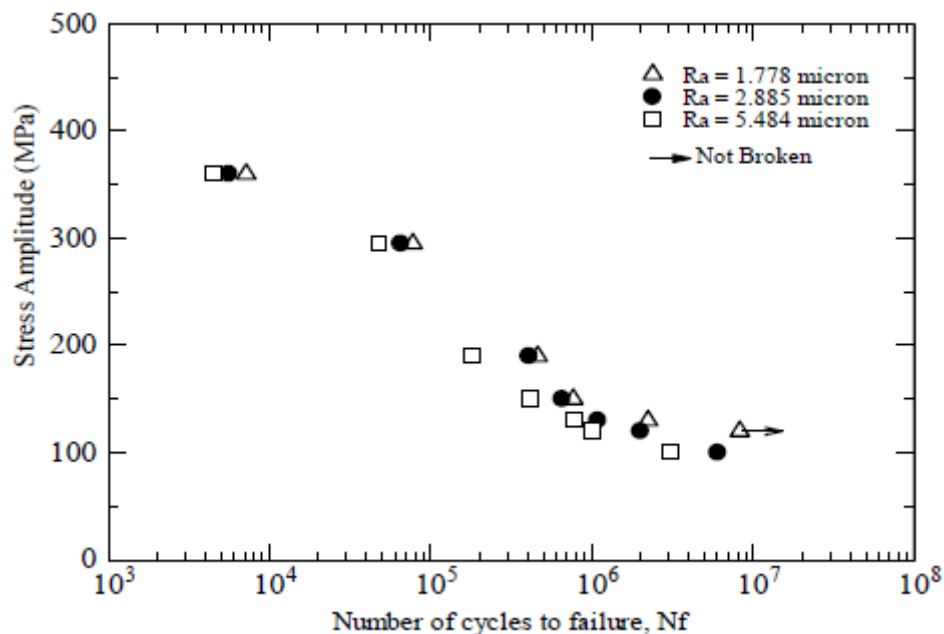


Figure 3.14: S-N curve for different surface roughnesses (Alang et al., 2011)

In their study, Alang et al. (2011) utilized emery papers of varying grit sizes to induce distinct surface roughness levels on test specimens. These specimens were then tested, leading to the conclusion that surface roughness does indeed impact fatigue life. However, it's important to highlight that in fatigue tests involving small- and large-scale specimens, the testing environment is consistent. When testing specimens, attention is paid to ensure metal quality is up to standard, for both small- and large-scale specimens, so no differences in surface roughness are present. Also, small-scale specimens are often cut from larger pieces of material, so the small-scale specimens used in fatigue tests exhibit an equivalent surface roughness to the large-scale specimen. Operational full-scale structures might exhibit more surface roughness due to corrosion and other external influences, influences that fall beyond the scope of this thesis and cannot be assessed within its confines.

All in all, it can be confirmed that surface roughness influences fatigue life, but it cannot be claimed that the steel employed in large-scale specimens is inherently rougher than the small-scale specimens. This scale effect might have a bigger influence on full-scale structures. Also, welded joints are often the location of failure in small- and large-scale specimens. The roughness of the surface is of little importance for these failures, as the surface defects are often way smaller when compared to defects in a weld.

### Residual stress

The differences in behavior seen in large-scale specimens and what would be expected from small-scale specimens can partly be attributed to the presence of residual stresses (Deul et al., 2022). Residual stress denotes a state of internal stress distribution persisting within a structure, component, plate, or sheet, even in the absence of any externally applied loads. The fatigue resistance of a structure is influenced by residual stresses, which can exert either a positive or negative effect. Tensile residual stresses negatively impact the fatigue life, whereas compressive residual stresses enhance it. If the local residual stress is highly compressive it squeezes the crack shut, effectively halting micro-crack growth (Schijve, 2009).

Figure 3.15 visualizes the effect residual stress has on the fatigue life of a specimen. Lines A and B represent constant amplitude loading, whereas the specimens used for line B have been thermally stress relieved of their residual stresses. The figure shows that stress relief heat treatment improves the high-cycle fatigue strength compared to the as-welded counterparts, but does not influence the fatigue strength for  $N < 10^6$  (Sonsino, 2009). Research by Ohta et al. (1986) also states the reduced fatigue life for specimens containing tensile residual stresses. Specimen experiencing loading cycling down from the yield strength, to simulate high tensile residual stresses, showed a reduced fatigue life compared to the same specimen at fixed stress ratios of -1, 0 and 0,5. The greatest reduction in fatigue strength was measured in the HCF region.

Residual stresses are caused by inhomogeneous plastic deformation. The area of plastic deformation no longer fits stress-free in the elastic material by which it is surrounded, which introduces a residual stress distribution. This plastic deformation is often heat-induced during the welding process. For this reason, there is a general assumption that the greater the number of welds in a specimen, the more extensive the distribution of residual stress tends to be. Thus, S-N curves that are created with small-scale specimen data would then overestimate the fatigue lifetime of full-scale structures, because of the present high tensile residual stresses. Fortunately, literature offers various recommendations for addressing the variations in residual stress between full-scale and small-scale specimens.

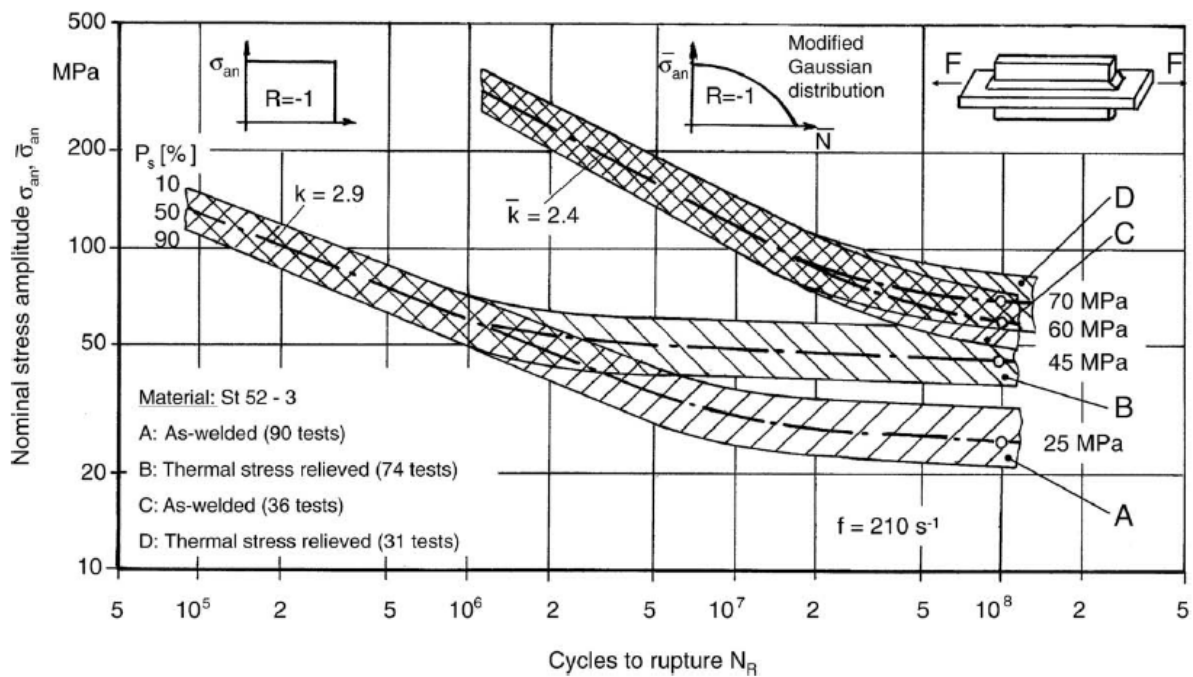


**Figure 3.15:** Effect of tensile residual stress on fatigue life (Sonsino, 2009)

In their research, Ohta et al. (2002) found a testing technique to simulate high residual stress distributions in small-scale specimens. He concluded that testing with the maximum stress equal to the material yield strength simulates the effect of high tensile residual stresses in small-scale welded specimens. This method is also recommended by Hobbacher (2016) and Lotsberg (2016). Ohta et al. (2002) also demonstrated that cut-outs taken from joints with residual stresses typically exhibit reduced residual stress levels, as is assumed by DNV (2021a, 2021b). However, Deul et al. (2022) demonstrated that an increased residual stress distribution is also possible, which means whether the residual stresses increase or decrease depends on the particular situation.

To account for residual stresses in fatigue assessment, one can use a mean stress correction model. Several methods exist, such as the Goodman or Gerber relation (Dowling, 2007), the Soderberg relation (Herzberg, 1995), or Walker's mean stress correction model (Walker, 1970). These correction models can be used to correct the measured stress, depending on the load ratio, as has been done in figure 3.3. With a correction model, stress that resulted from a fatigue test can be shifted to simulate a higher mean stress and thus a higher residual stress. This method can be applied to investigate the effect of residual stresses on small- and large-scale specimens.

### 3.5. Concluding remarks

This paragraph will conclude the findings from section 3.4 and relate to what it means for the current research.

First are the statistical scale effects. The weakest link theory showed that smaller specimens were, in general, less likely to fail. This can be explained by welding-induced defects that are embraced in the volume effect theory by Blacha et al. (2013). The theory shows a relationship between the probability of failure and increasing weld length, as well as dimensions of welded elements. Other studies also present similar findings with a reduced fatigue life in specimens with reduced size. Thus it can be concluded that this scale effect certainly plays a role in reducing fatigue life for larger specimens. However, exact details of weld defects and weld lengths are missing, so it is impossible to include them in this research. So for this thesis, this scale effect is not something that will be investigated.

The sample size scale effect will be tackled by creating as many FE models as possible within the allowable time frame, as more data points will lead to more trustworthy conclusions.

Next are the geometrical scale effects. The geometrical notch effect is observed when material irregularities affect the stress distribution. In a study using notched specimens, it was found that larger specimens have higher stress at crack tips, leading to a higher stress concentration factor and lower fatigue resistance. However, the effective notch stress concept (ENSC) considers this effect. Comparing the ENSC with concepts ignoring the notch effect can help assess its influence.

Structural redundancy involves intentionally including extra structural components in a design to ensure a structure's reliability, even if some elements fail. It distributes loads evenly, reducing the risk of catastrophic failure. Redundancy can significantly enhance fatigue strength, as it helps distribute cyclic loads across multiple paths. While it's a desirable property for overall structures, it's often less relevant when examining local elements, like welded joints. When examining a joint with a concept including local information, the scale effect disappears. So in this thesis, these concepts will be used to examine the influence of the structural redundancy scale effect.

The following scale effects are technological scale effects that are introduced during production. Surface roughness in machined steel sheets results from the material's processing, with factors like tool-metal friction, chip removal, and processing system vibrations playing a role. Surface roughness leads to the emergence of microscopic defects, promoting crack initiation on the material surface. It affects fatigue strength, with rougher surfaces leading to decreased fatigue life. Studies show this impact, but these tests are with intentionally introduced surface roughnesses. In a testing environment, small-scale specimens have an equal roughness as large-scale specimens, so there is no reason to believe that this scale effect has an impact on scaling from small to large scale. Full-scale operational structures, however, may have more roughness due to external factors, such as corrosion. This is something to keep in mind when assessing a full-scale structure, but that lies outside of the scope of this thesis.

The final scale effect that can be distinguished is residual stress. Residual stresses refer to a higher or lower mean stress being present in the material. It can impact fatigue resistance, with tensile stresses reducing it and compressive stresses enhancing it. The amount of residual stress is often unknown without destroying the specimen, which makes it hard to account for it exactly. Testing techniques at high load ratios can simulate high residual stress conditions in small-scale specimens. Also, mean stress correction models can account for present residual stresses. This thesis will use this approach to investigate the influence of residual stress on fatigue life.

It was mentioned that some scale effects are not present in some phases of scaling. Figure 3.16 shows the two different scaling phases. Associated with the first arrow are: the weakest link theory, the sample size, the notch effect, structural redundancy, and residual stress. Associated with the second arrow are the same, plus the additional surface roughness scale effect.

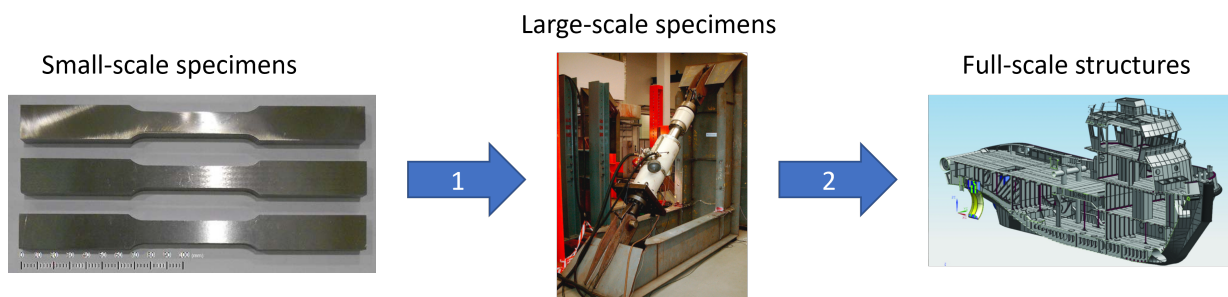


**Figure 3.16:** Scaling phases 1 & 2, corresponding with scaling from small-scale specimens (Loporcaro et al., 2015) to large-scale specimens (Fricke et al., 2010) and from large-scale specimens to full-scale structures (Siemens, 2021), respectively.

---

This thesis will focus on scale effects related to the fatigue resistance behavior of materials. Scale effects can also be distinguished when looking at the loading on a small-scale specimen and a full-scale operational structure. Marine structures are loaded with water pressures, operational demands, wind gusts, and more. A complex range of loads, which are impossible to recreate in a laboratory environment with forces and a three or four-point bending moment.

# 4

## Research overview

This chapter presents an overview of what will be researched in this thesis. The knowledge gap is given in section 4.1. Section 4.2 presents the hypotheses that will be tested in this research, with some explanation given for each hypothesis. The research methods that will be adopted in this research will be given in section 4.3.

### 4.1. Knowledge gap

In literature, research into the fatigue similarity of small-scale specimens and large-scale specimens is limited. In his PhD, den Besten (2015) showed small- and large-scale specimen fatigue resistance similarity using local fatigue assessment concepts, but for aluminum structures and not for steel. Additionally, the similarity was proven using the total stress concept (TSC). This research will focus on proving fatigue similarity between steel small- and large-scale specimens, using a less complex fatigue assessment concept than the TSC.

Section 3.4 dove into the different scale effects that arise when scaling from small- to larger scales. The different effects are known in literature, however, it is unclear how big the influence of each effect is on the fatigue performance of specimens. Research in which full-scale pipes and small-scale specimens cut from the same series of pipes and where a lower fatigue limit for the full-scale structures was found, Maddox et al. (2008) state: "Attempts to explain the difference in fatigue limit between the full-scale and strip specimens suggested that it was due to a combination of differences in flaw size, weld root bead quality and residual stress, but a definitive explanation could not be found from the information available." This research will seek to illustrate the amount of impact of certain scale effects. Specific attention will be paid to the notch effect, structural redundancy, and residual stresses.

Simultaneously, to achieve immediate practical relevance, a clear understanding of the scale effects that are currently not accounted for when using the HSSSC is desired. A better understanding of what is left out and the influence of these factors can help reduce fatigue design conservatism.

### 4.2. Hypotheses

The hypotheses that will be tested in this research are the following:

- I: Large-scale fatigue data will fit in the small-scale data scatter band when incorporating local (weld) geometry information.

This hypothesis essentially has two sides to the coin. First, it states that fatigue resistance similarity can be proven if local geometry information is incorporated. Fatigue resistance similarity between the large-scale fatigue specimens and the small-scale fatigue specimens is proven if the large-scale fatigue data fits the small-scale data scatter band. It is expected that the large-scale data will fit when a fatigue assessment concept is used that incorporates local joint information, i.e., the HSSSC or ENSC. On the other side, it also states that large-scale fatigue data will not fit the small-scale data scatter band when local geometry information is not included. Thus, it is expected that local weld geometry is needed to prove fatigue similarity.

II: Large-scale fatigue data captured with the ENSC will prove to have a better fit in the small-scale data scatter band than fatigue data captured with the HSSSC. The reason for the better fit is less structural redundancy effect and the removal of the notch effect.

This hypothesis originates from the work of Qin et al. (2021), Qin et al. (2019) where it is demonstrated that the ENSC provides a better fit for steel welded joints in the small-scale data scatter band than the HSSSC. It is expected that this will also be the case for large-scale specimens. A better fit means that the performance indicators, such as the standard deviation and the strength scatter band index  $T_{\sigma s}$ , will decrease.

III: Applying a mean stress correction will provide for a better fit of the large-scale specimen data in the small-scale data scatter band.

Applying a mean (residual) stress correction will show the influence of the load ratio as well as the residual stress on the fatigue performance of large-scale specimens. It is expected that it will provide a better fit.

### 4.3. Methods

This paragraph will present research methods employed in this thesis to provide evidence that will or will not support the hypotheses.

To test if large-scale fatigue data will fit in the small-scale data scatter band using local information, the HSSSC and ENSC will be adopted, using the semi-analytical formulation. These concepts can only be applied once FE models have been created from the large-scale specimens tested in literature. These FE models will be created using the FE software Abaqus 2023. To test the third hypothesis, a mean stress correction model will be adopted.

Table 4.1 displays the methods that will be used to check for the different scale effects. The nominal stress concept will be used as a baseline to compare the other methods. More local fatigue assessment concepts include more of the scale effects.

**Table 4.1:** The methods used to check for the effect of different scale effects

Method	Scale effects included
Nominal stress concept	Load path redundancy & notch effect
Hot spot structural stress concept	Less load path redundancy & notch effect
Effective notch stress concept	Little load path redundancy

# Part II

## Research

# 5

## Small- & large-scale specimens

This chapter will explain the SSS and LSS that this research revolves around. To test and determine if the LSS fit the SSS scatter band, large- and small-scale specimens are needed to compare and draw conclusions. Section 5.1 will dive into the small-scale specimens that will be used as a reference in this research, while section 5.2 will explain which large-scale specimens are going to be examined.

### 5.1. Small-scale specimens

This section will dive into the small-scale specimen fatigue test results that are going to be used in this research. To make a comparison between the fatigue resistance of SSS and LSS, a reference database of SSS fatigue test results will be consulted. This database was constructed in papers from Qin et al. (2021), Qin et al. (2019) and was mentioned in chapter 2.

The database consists of more than 2600 data points, of which 2090 are failures and can be used for analysis. The database covers the joint types that are the most common in steel plate structures. With this variation in joint types also comes the variation in HS types. Figure 5.1 shows the SSS database for nominal stress and excluding run-outs. The database also varies in base plate thickness, load ratio, yield strength, and ways of loading. The base plate thicknesses in the database vary from 2 to 160 mm. Loading and response ratios range from -1 to 0.8 and the yield strength is between 245 and 1030 MPa. Materials with different yield strengths can be compared for their fatigue performance because factors such as weld geometry, weld quality, and loading conditions often have more of an influence on fatigue behavior than the base material's yield strength. Since fatigue loading involves cyclic stresses much lower than the material's yield strength, the absolute value of yield strength becomes less important in fatigue analysis. Instead, the focus is on factors that affect fatigue life, such as micro-, meso-, and macroscopic stress concentrations at welds and defects (Hobbacher, 2016; Ohta et al., 1993). Therefore, materials with different yield strengths can still be compared effectively based on their fatigue performance under similar conditions. The applied load is either a (3- or 4-point) bending moment or a normal force. The fatigue lifetimes  $N$  cover the MCF and HCF region. All small-scale specimens are in as-welded condition and failures have been obtained at the weld toe (Qin et al., 2019). With all these variations, the database can justifiably be used as a reference database.

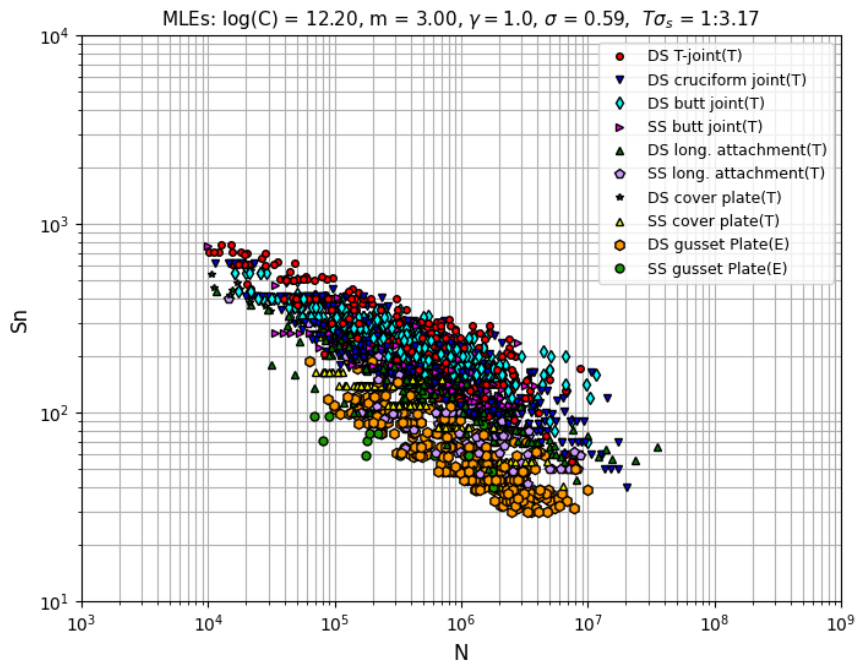


**Figure 5.1:** SSS database scatter band excluding run-outs

Figure 5.1 depicts the nominal stress scatter band. The HSSSC and ENSC have been applied to all data points to create scatter bands for these concepts as well. The three SSS scatter bands will be used in chapter 6 to compare with the results from the LSS.

At the top of figure 5.1, the symbol  $\gamma$  is displayed. This denotes the application of Walker's mean stress correction to account for mean stress effects. This correction involves the response stress range  $\Delta\sigma = (\sigma_{max} - \sigma_{min})$  and the load ratio  $R = (\sigma_{min}/\sigma_{max})$ . The effective stress is calculated using equation (5.1). The loading and response ratio coefficient  $\gamma$  serves as a fitting parameter. Notably, when  $\gamma = 1$ , the mean stress correction is not applied, as shown in figure 5.1.

$$S_{eff} = \Delta\sigma_{eff} = \frac{\Delta\sigma}{(1 - R)^{1-\gamma}} \quad (5.1)$$

## 5.2. Large-scale specimens

The small-scale specimen scatter band will be compared to a database of large-scale specimen data points. This database has been compiled from the results of fatigue tests on LSS. The database is displayed in table 5.1.

**Table 5.1:** The large-scale specimen database

Joint type	HS type	$t_p$	$R$	Nominal stress by:	Reference
DS long.attachment	A	15	0	Strain gauges <sup>2</sup>	Polezhayeva et al. (2013)
DS T-joint	A	11.5	0	Strain gauges <sup>1</sup>	Fricke et al. (2010)
DS long. attachment	A	10	0	Strain gauges <sup>1</sup>	Fricke et al. (2010)
DS T-joint	C	10	0	Structural calculation <sup>5</sup>	Zamiri Aklaghi et al. (2009)
DS cruciform joint	C	6	-1	Structural calculation <sup>5</sup>	Kozak (1999)
DS T-joint	C	16	0.2	Strain gauges <sup>1</sup>	Feng et al. (2022)
DS butt joint	A	16	0	Structural calculation <sup>5</sup>	Miki et al. (1997)
DS cruciform joint	A	13	-0.5	Strain gauges <sup>3</sup>	Rizzo et al. (2007)
DS cruciform joint	A	13	-1	Strain gauges <sup>3</sup>	Rizzo et al. (2007)
DS cruciform joint	A	14	-1	Structural calculation <sup>5</sup>	Yuan (2011)
SS long. attachment	A	14	0	Structural calculation <sup>5</sup>	Nagy et al. (2017)
DS butt joint	A	7	-1	Strain gauges <sup>4</sup>	Rizzo et al. (2013)
DS cruciform joint	C	9	-1	Strain gauges <sup>1</sup>	Zheng et al. (2019)
DS cruciform joint	A	9	-1	Strain gauges <sup>1</sup>	Zheng et al. (2019)
DS T-joint	A	16	0	Strain gauges <sup>1</sup>	Li et al. (2020)
DS long. attachment	A	9	0.2	Structural calculation <sup>5</sup>	Z.-G. Xiao et al. (2005)

<sup>1</sup> at 1.5t away from weld toe

<sup>2</sup> at 50 mm distance from weld toe

<sup>3</sup> at the midspan of the specimen

<sup>4</sup> at the top of the bulb

<sup>5</sup> with a bending moment or normal force

The database consists of 55 data points, varying in joint type, HS-type, plate thickness, and load ratio. The database is displayed in figure 5.2, where it is categorized by joint type. In the papers, nominal stress data on the LSS was found, meaning a one-to-one comparison can be made.

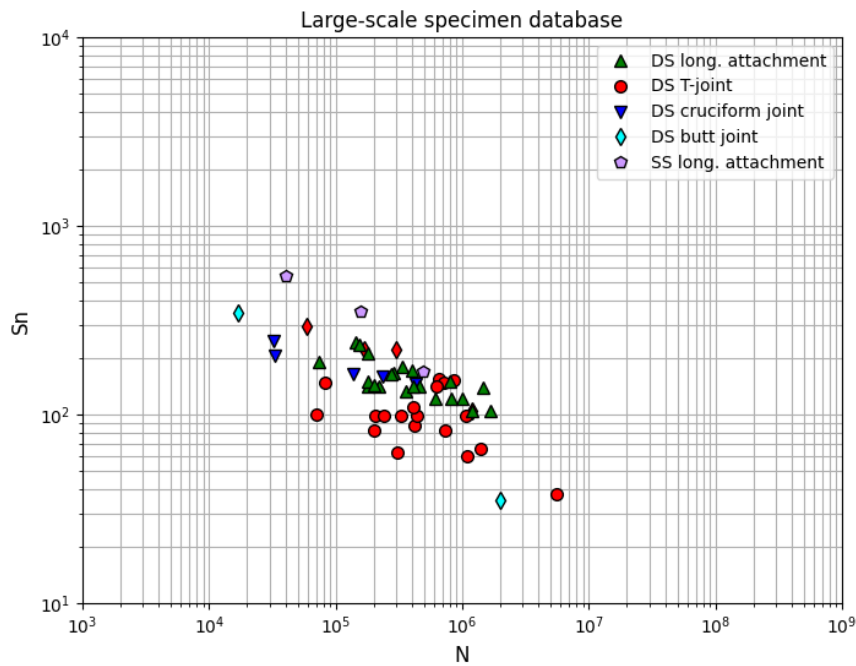


**Figure 5.2:** Large-scale specimen database by joint types

In order to compare small- and large-scale specimens using the HSSSC and the ENSC, it is necessary to create FE models. These models are essential because the fatigue assessment concepts require information that is not present in the papers constituting the database. This information can be acquired through creating and analyzing FE models.

The FE models will be created using the finite element software ABAQUS. Modeling was done employing 2D shell elements for their applicability to the analysis of thin-walled structures, where the aspect ratio between two dimensions significantly exceeds that of the third. However, it is necessary to discuss the alternative option of 3D solid elements within finite element analysis. Unlike shell elements, solid elements possess three-dimensional geometry, occupying volume within the model space. They are typically characterized by 4, 8, 10, or 20 nodes per element, offering a comprehensive representation of the component's geometry and material behavior throughout its entire volume. While solid elements are suitable for a wide range of geometries, their utilization in thin-walled structures is limited due to their inefficiency in capturing the structural behavior of components with highly disparate dimensions. Moreover, the computational resources required for meshing and solving solid element models can be considerably greater than those required for shell element models, as shell elements only use 4, 5, 6, or 8 nodes. Therefore, while solid elements may provide more accurate results in certain scenarios, the practicality and efficiency of shell elements make them the preferred choice for the analysis of thin-walled structures in this study.

Due to time limitations, it is not possible to create FE models for every LSS that is in the database. A selection was made of three specimens, varying in connection and hot spot type. These LSS originate from papers from Kozak (1999), Rizzo et al. (2007), and Z.-G. Xiao et al. (2005) and concern a frame-frame connection, frame-stiffener connection, and a scallop respectively. To get a feel of the position of these specimens in the nominal scatter band, figure 5.3 displays the nominal stress data points for the selected specimens.

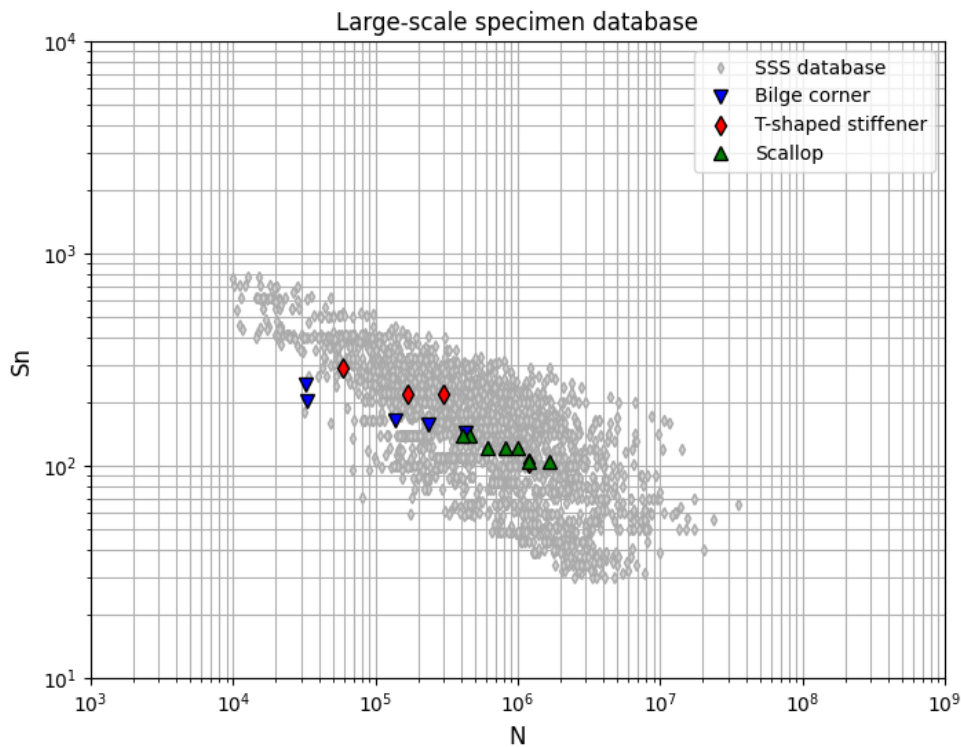


**Figure 5.3:** Selected large-scale specimens

This section will delve into the three distinct specimens along with their respective finite element models. Specifically, subsection 5.2.1 will explore the bilge-corner of a Ro-Ro (Roll-on-Roll-off) ship detailed in Kozak (1999), subsection 5.2.2 will address a T-shaped stiffener into a deep web connection, documented in Rizzo et al. (2007), and finally, subsection 5.2.3 will examine the scallop discussed by Z.-G. Xiao et al. (2005).

### 5.2.1. Bilge corner of Ro-Ro ship

The first large-scale specimen that will be discussed is the bilge corner of a Ro-Ro ship, found in papers by Kozak (1999) and Kozak et al. (2015). The specimen is previewed in figure 5.4. The figure depicts the bilge corner consisting of an outer and inner hull, a transverse web with stiffeners and frames spanning between the outer and inner hull. The specimen has a width of 300 mm, a depth of 2585 mm, and a height of 1650 mm. The thickness of all plates is equal to 6 mm, except for the transverse web having a thickness of 5 mm. The loading and support location is also shown, together with the critical weld toe. A schematic of the specimen is given in figure 5.5. The specimen is part of a series that was tested in the Technology Laboratory of Shipbuilding Faculty of the Technical University of Gdansk. Five identical specimens, called specimens 22 to 26, underwent testing with varying load ranges, leading to differences in the number of cycles required for failure to occur. The nominal stress ranges vary between 147 and 245 MPa and the number of cycles to failure vary between 32000 and 427000. The loading that is applied is fully reversed, so  $R = -1$ .

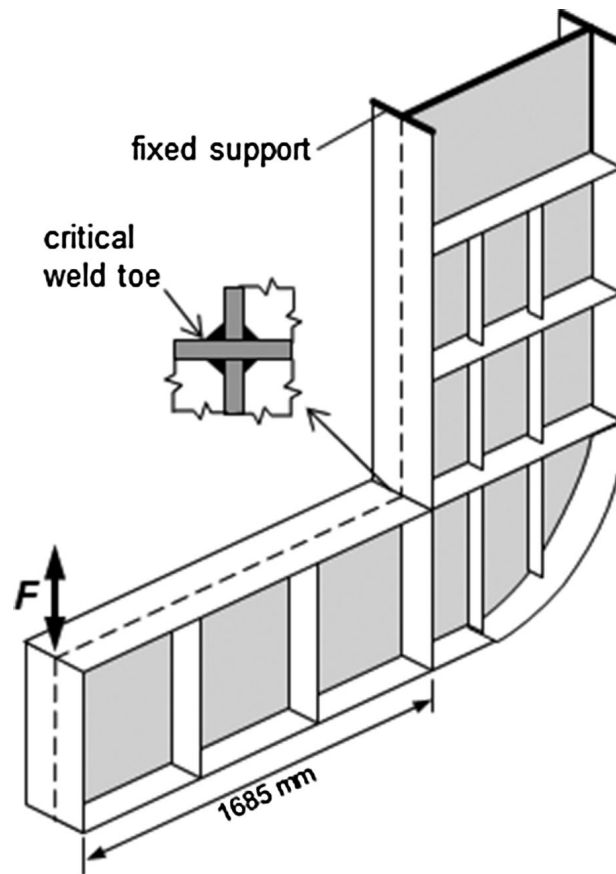


Figure 5.4: The bilge corner specimen (C. Fischer et al., 2018)

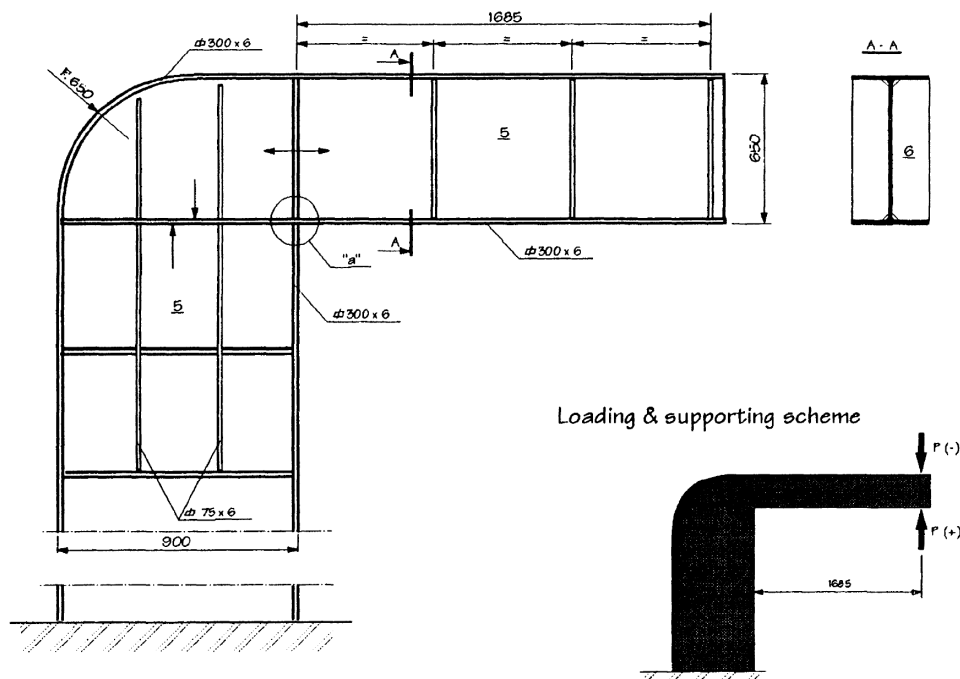
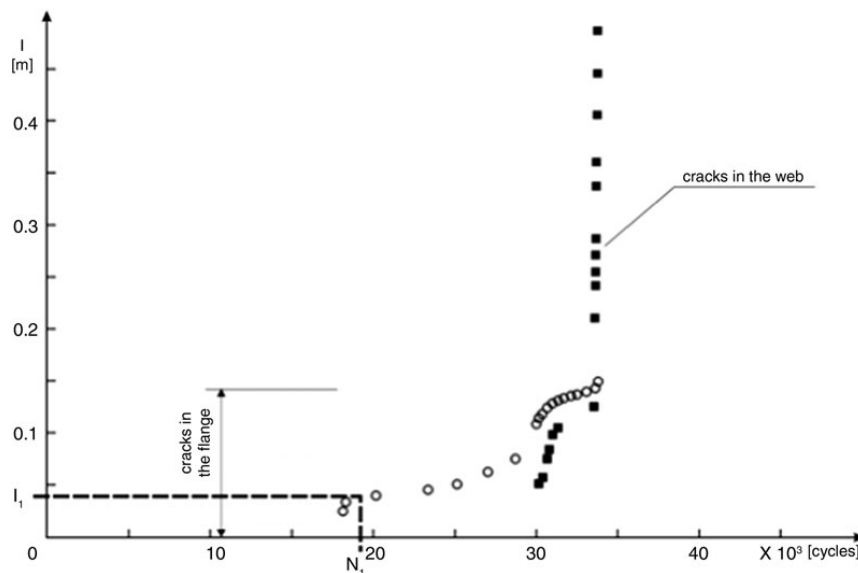


Figure 5.5: Schematic of the bilge corner (Kozak, 1999)

The paper by Kozak (1999) does not explicitly mention the failure criterion and thus when testing is stopped.

In the later paper by Kozak et al. (2015), the same bilge corner specimen is mentioned, named specimen 25, which corresponds to a specimen number in Kozak (1999) as mentioned before. However, it is not mentioned explicitly that it covers the exact same specimen. In Kozak et al. (2015), a figure displaying the crack propagation in the flange and web for specimen 25 is given. This figure is displayed in figure 5.6. The first visible cracks in the flange and web are respectively at 18000 and 30000 cycles. The fatigue test was stopped at 34000 cycles. At this point, the crack in the flange has reached a length of 150 mm, which is assumed to be the length from the middle to the outer side of the specimen, as the total width of the specimen is 300 mm. After the complete fracture of flanges, web cracks accumulated exponentially until a length greater than 500 mm. For specimens 22, 23, 24, and 26, the length and propagation of the fatigue cracks are unknown.

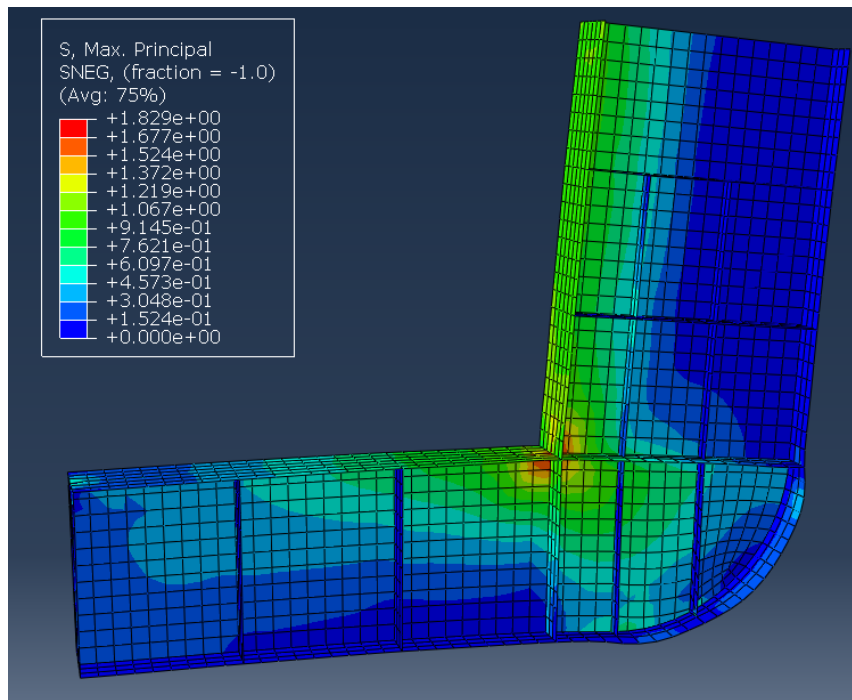


**Figure 5.6:** The propagation of fatigue cracks in one of the specimens (Kozak et al., 2015)

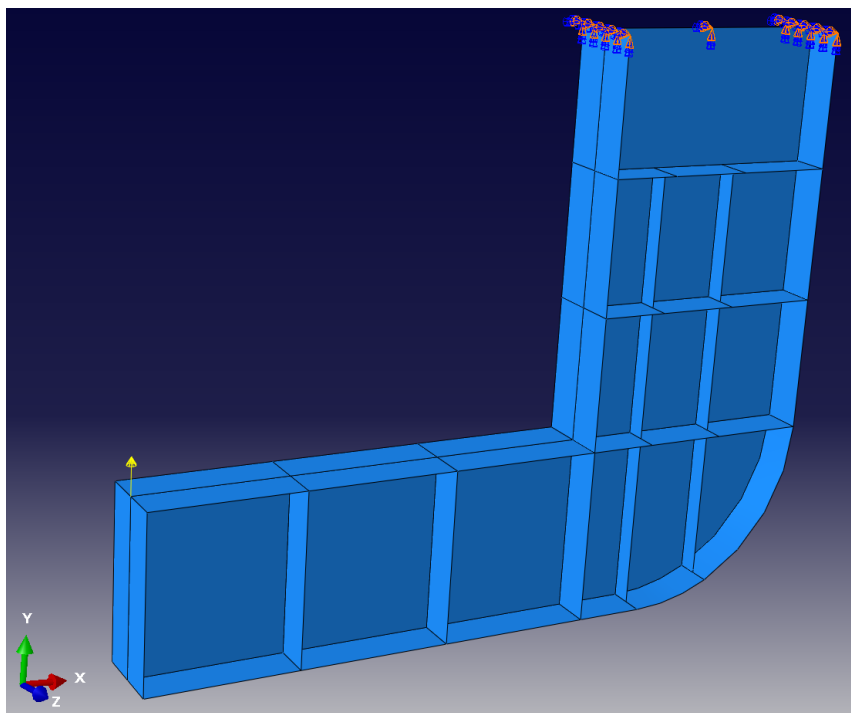
The critical weld toe is displayed in figure 5.4. The critical point is located centrally along the specimen's weld, designated as a HS type C, but considering the web attachment, it can alternatively be interpreted as a HS type A. However, in this research, the critical weld toe will be treated as a HS type C. This joint is considered as load-carrying.

Figure 5.7 shows the FE model from ABAQUS in a loaded condition. In the figure the maximum principal stress is shown. It can be seen that the hot spot is at the location that was pointed out previously. The applied loading was such, that using the nominal bending stress the stress at the weld was equal to 1 MPa. Kozak (1999) applied loading that, with the same method, led to stresses equal to 147, 158, 165, 206 and 245 MPa. This method was not chosen in the FE model for simplicity. As the model is fully elastic, the stresses and forces could be multiplied by the desired nominal stress to obtain the required results.

The constraints and loading position are shown in figure 5.8. The nodes at the top of the bilge corner are fully constrained and, thus are restricted to move and rotate in any direction. The yellow arrow at the left end of the model indicates the position where the loading is applied.



**Figure 5.7:** Overview of the bilge corner FE model in loaded condition



**Figure 5.8:** Boundary conditions and loading position of the bilge corner

### 5.2.2. T-shaped stiffener

The second LSS is the crossing of a T-shaped longitudinal stiffener into a deep web, found in the paper by Rizzo et al. (2007) and displayed in figure 5.9. This deep web can simulate either the web of primary structural members or bulkhead plating. The stiffener is connected to a plate, simulating the shell of a structure. The specimen has a total length of 4000 mm, with the bulkhead plates being placed at equal

distances from either side and a distance of 1300 mm between them. Onto one of the bulkhead plates, an overlapping patch is welded, which creates two different details in one specimen. The T-stiffener has dimensions 200 x 13 x 120 x 13 mm. A schematic overview with dimensions is given in figure 5.10. At both ends the beam is supported by hinged supports and loading is applied synchronously on both the faceplates of the deep webs, which creates a 4-point bending test. The locations of interest are where the flat bars (that are attached to each bulkhead plate) are connected to the T-shaped stiffener. Both locations are interesting because one side has an overlapping patch, which could lead to different structural behavior. Multiple specimens were tested, with stress ranges varying between 105 and 294 MPa, and load ratios of either -0.5 or -1.

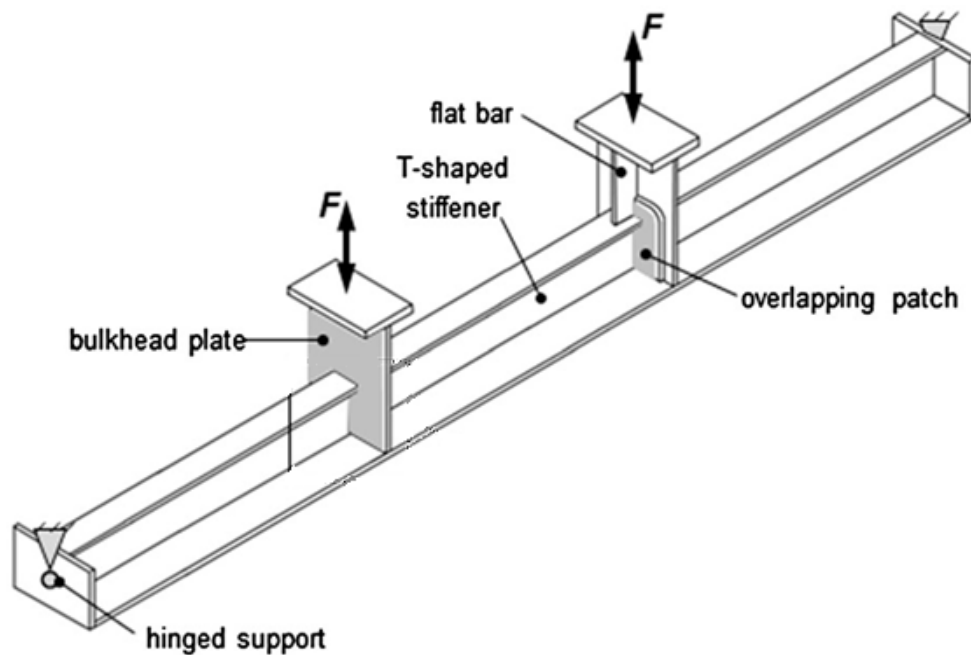


**Figure 5.9:** T-shaped stiffener connection (C. Fischer et al., 2018)

As well as all the dimensions, figure 5.10 also shows the fatigue crack initiation locations, denoted as crack positions 1 & 2. This is where the flat bars meet the flange of the stiffener, and can thus be denoted as a HS type A. This joint is considered as load-carrying. The large-scale specimens were tested until complete failure of the flange of the stiffener. This is the failure criterion considered for the number of cycles to failure. For this specimen,  $N$  varies between 59460 and 120000.

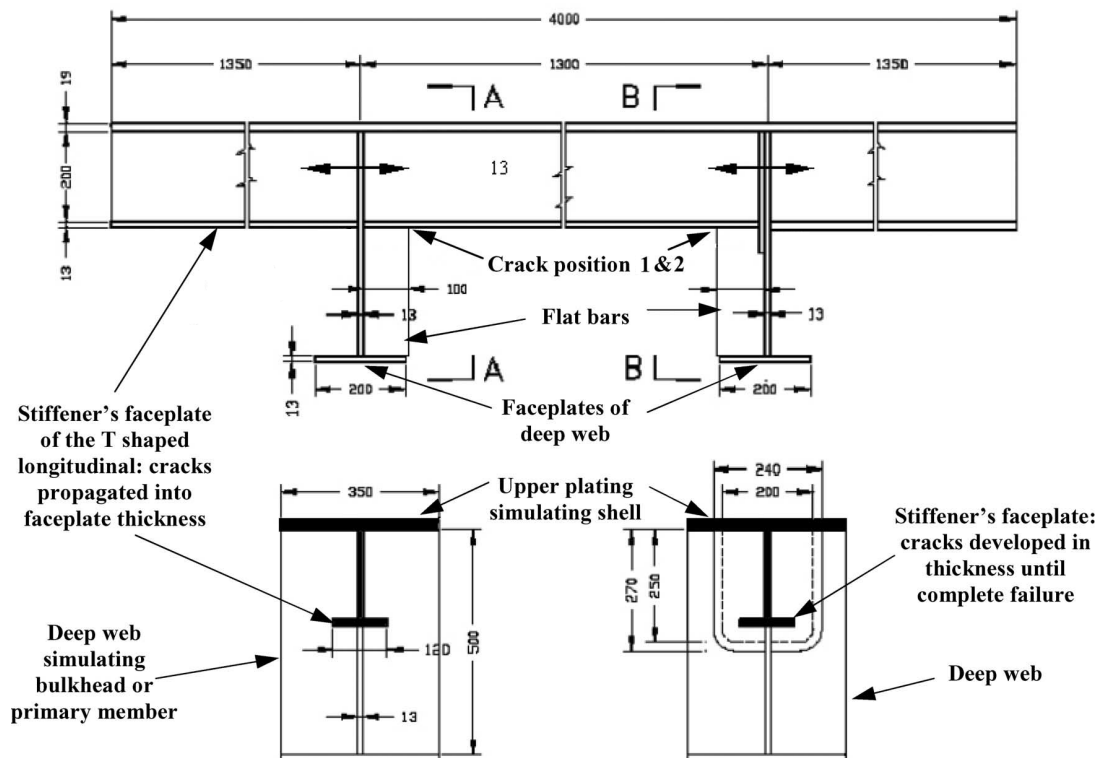


**Figure 5.10:** Schematic of the T-shaped stiffener (Rizzo et al., 2007)

The FE model is shown in figure 5.11 in loaded condition. The maximum principal stresses are shown. In the figure, the fatigue crack positions are already visible. Where the flat bars meet the top of the flange, the model shows an increase in stress. The overlapping patch was modeled as a plate with a local increase in plate thickness to ensure a good connection with the other shell elements and to make sure that the stresses travel through the heart of the plate. "The stress acting along the longitudinal direction on the lower faceplate of the stiffener at midspan has been assumed as the reference nominal acting stress" (Rizzo et al., 2007). The same reference stress location has been assumed for the FE model. The loading was applied on the two faceplates, so that the stress at the reference location was equal to 1 MPa, for the same reason as with the bilge corner.

The constraints and loading position are shown in figure 5.12. The nodes at both ends of the stiffener are restricted from moving in any direction and also rotation around the y- & z-axis is prohibited, meaning only rotation around the x-axis is allowed. The nodes located at the bottom of the specimen, where the actuators are located, can not rotate in any direction and can only move in the z-direction. This mimics the pure up-and-down motion initiated by the actuators. At the same location, thus all the nodes at the bottom, the load is applied in the form of a pressure.

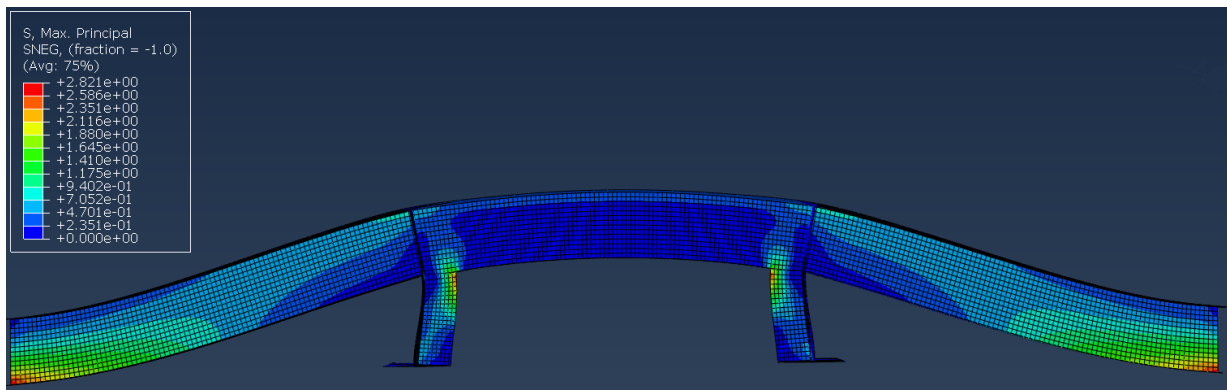


**Figure 5.11:** Overview of the T-shaped stiffener FE model in loaded condition

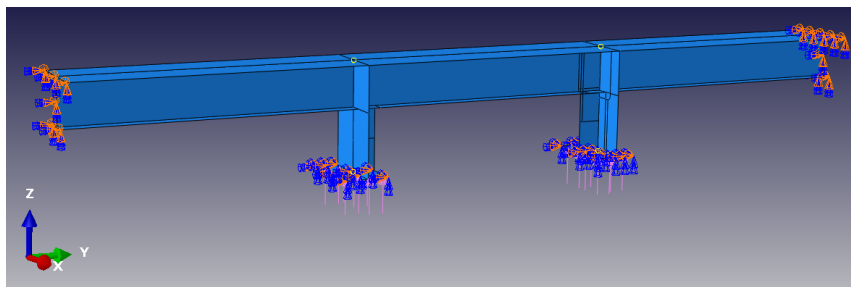


**Figure 5.12:** Boundary conditions and loading position of the T-shaped stiffener

### 5.2.3. Scallop

The last LSS that will be discussed in detail is a scallop by Z.-G. Xiao et al. (2005). The specimen is displayed in figure 5.13. The figure shows a double-sided H-shaped attachment welded onto a base plate. The base plate has a length of 1000 mm and a width of 200 mm. The H-shaped attachment has a length of 200 mm, a width of 160 mm, and a height of 100 mm. All plates have a thickness of 9 mm. The interesting feature of this specimen is the scallop that is introduced on both sides of the longitudinal plate. This scallop has a radius of 35 mm. A schematic overview with all dimensions is shown in figure 5.14. The loading is applied as a normal force on the base plate. The stress range was set at three levels, i.e., 105, 122, and 140 MPa. The minimum tensile stress was set at 27 MPa throughout all tests, so the tests have a load ratio  $0.15 < R \leq 0.20$ . The number of cycles to failure varies between 411000 and 1672000. The fatigue crack developed on the location shown in figure 5.13. The HS on this location is of type A, where the longitudinal attachment turns into the scallop. This joint is considered as non-load-carrying. On each specimen and at a distance of 10 mm from all hot spots, small copper wires were attached. Failure of a specimen was considered when the wires had broken as a result of fatigue crack growth.

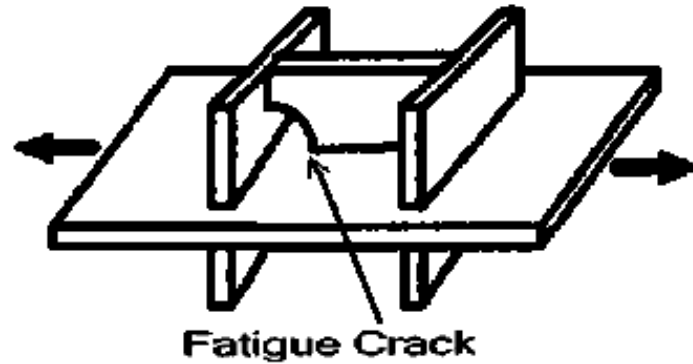


Figure 5.13: Double-sided H-shaped attachment (Z.-G. Xiao et al., 2005)

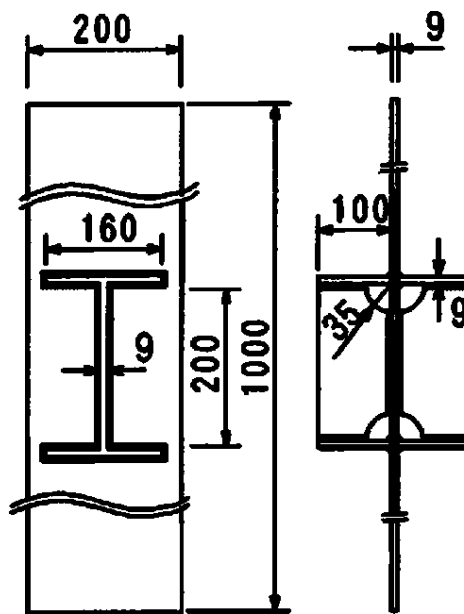


Figure 5.14: Schematic of the scallop (Z.-G. Xiao et al., 2005)

The corresponding FE model is shown in figure 5.15 in loaded condition. At the bottom of the scallop, where it meets the base plate, a stress concentration is visible. This is the same location as where fatigue cracks originated. The applied loading is a normal force applied at one side of the model. The force applied was such that in the plate a stress equal to 1 MPa was achieved.

The constraints and loading position are shown in figure 5.16. The left end of the model is fully clamped, and thus the nodes are restricted to move or rotate in any direction. The loading is applied on the right end of the model. On this side, the nodes are free to move along the y-axis.

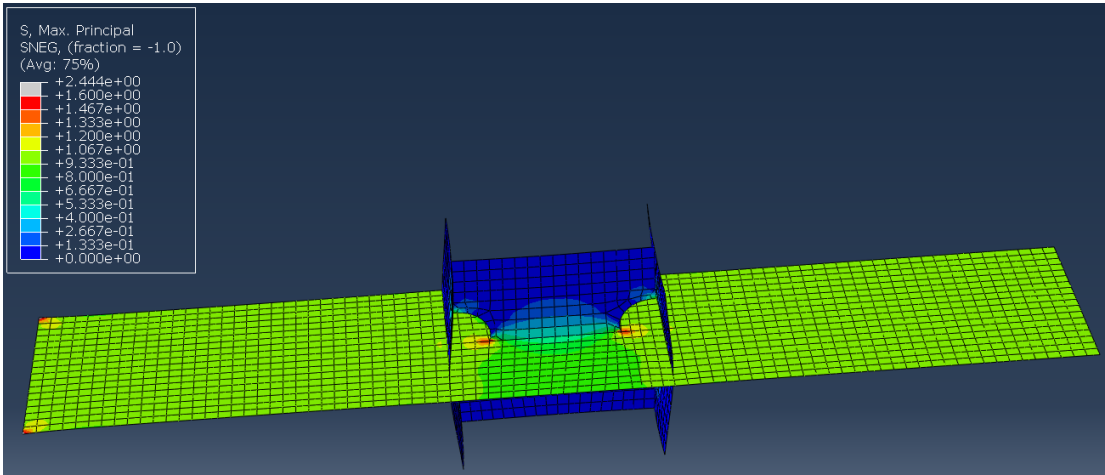


Figure 5.15: Overview of the scallop FE model in loaded condition

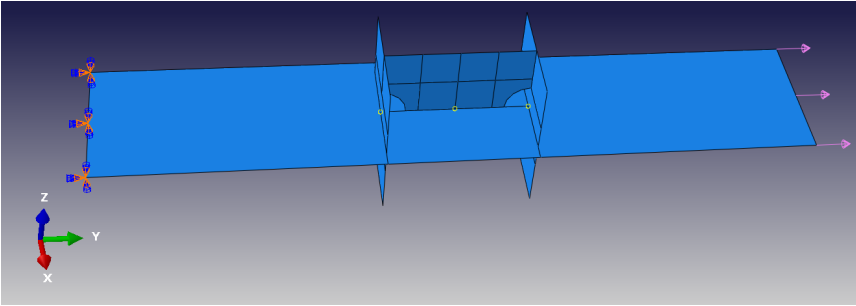


Figure 5.16: Boundary conditions and loading position of the scallop

# 6

## Similarity analysis

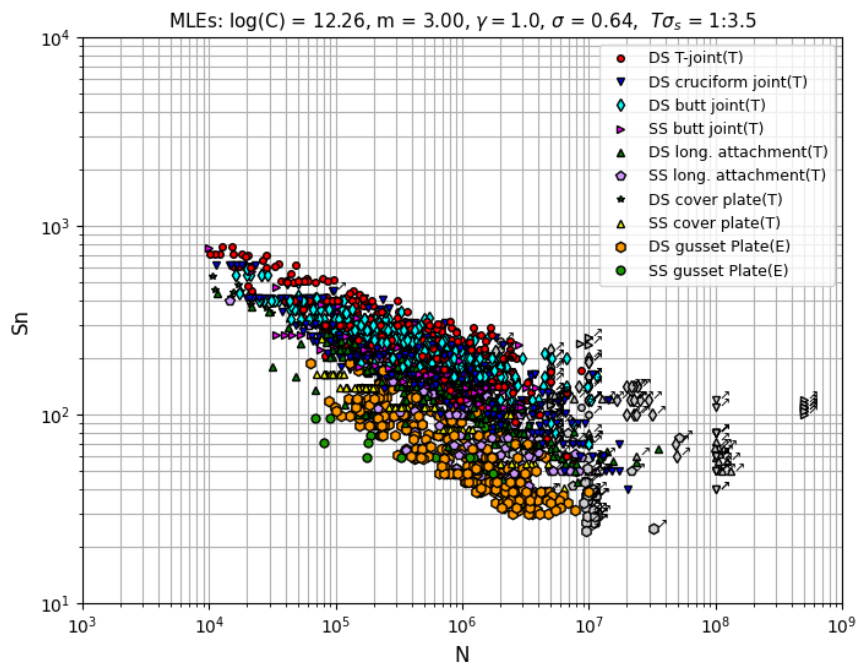
This chapter presents the analyses and considerations concerning fatigue resistance similarity between small-scale specimens and large-scale specimens. For this analysis, three fatigue assessment concepts will be used. First, in section 6.1 the NSC will be adopted. In section 6.2 similarity will be looked at using the HSSSC and finally in section 6.3 the ENSC will be used. Section 6.4 will make a direct comparison for all concepts and dicate the influence of the scale effects.

### 6.1. Nominal stress concept

One of the most widely used fatigue assessment concept is the NSC, which is explained in more detail in section 2.1. This section will use the NSC to test and compare the small- and large-scale specimen database from chapter 5. Subsection 6.1.1 will discuss the SSS database, while Subsection 6.1.2 covers the LSS database. In Subsection 6.1.3 a comparison will be made.

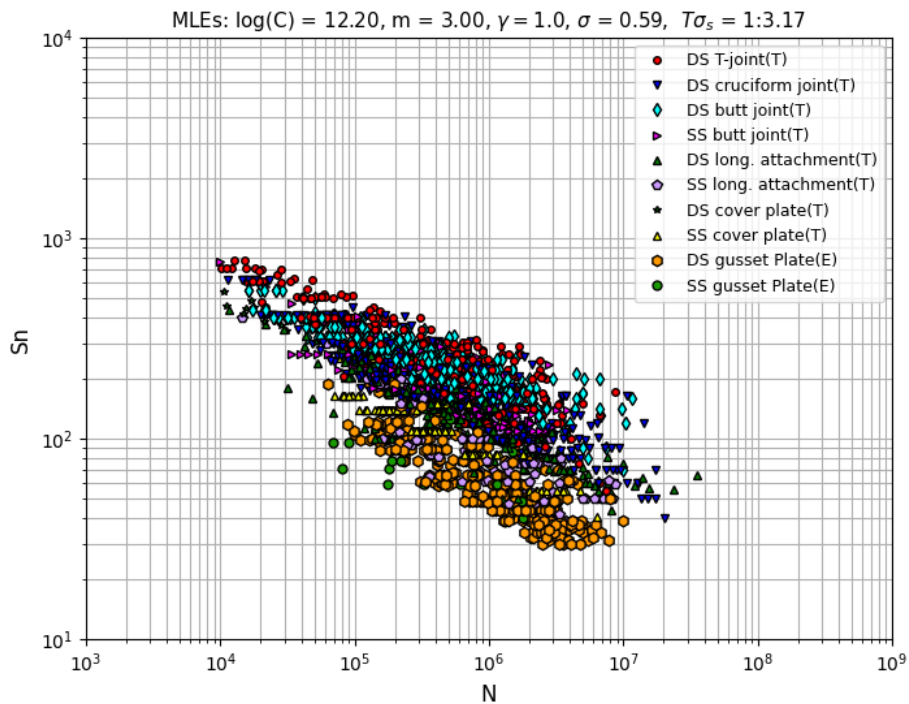
#### 6.1.1. Small-scale specimen database

Figure 6.1 shows the full SSS database consisting of over 2600 specimens. The figure also shows the maximum likelihood estimators (MLE's) and the  $T_{\sigma_s}$ . For the NSC SSS scatter band including run-outs, the values for the standard deviation ( $\sigma$ ) and  $T_{\sigma_s}$  are 0.64 and 1:3.5 respectively.



**Figure 6.1:** NSC SSS database scatter band including run-outs

As for this research, it is a priority to identify and understand the critical failure mechanisms. For this reason, only complete fatigue data will be considered. By concentrating on complete failures, the factors that caused fatigue failure can be distinguished. Figure 6.2 displays the SSS scatter band without the run-outs. The MLE's display a reduction in scatter. The  $\sigma$  reduces from 0.64 to 0.59 and the  $T_{\sigma_s}$  is brought down from 1:3.5 to 1:3.17. The reduction in scatter can be expected when examining the positions of the run-outs in figure 6.1. The majority of run-outs are positioned to the right of the main cluster of data points, contributing to the observed scatter.



**Figure 6.2:** SSS database scatter band excluding run-outs

The value for  $m$  in figures 6.1 and 6.2 is equal to 3.00, and should originate from a linear curve fit using equation (6.1).

$$\log(N) = \log(C) - m * \log(S) \quad (6.1)$$

However, the values for  $m$  in the NSC analysis do not originate from equation (6.1). Instead, it has been decided to set  $m = 3.00$ , because this value is usually adopted for the nominal stress (Hobbacher, 2016). In the other analyses, the value for  $m$  will be based on a fit using equation (6.1). For illustration purposes, figure 6.3 displays what a different value of  $m$  does to the slope of the curve.

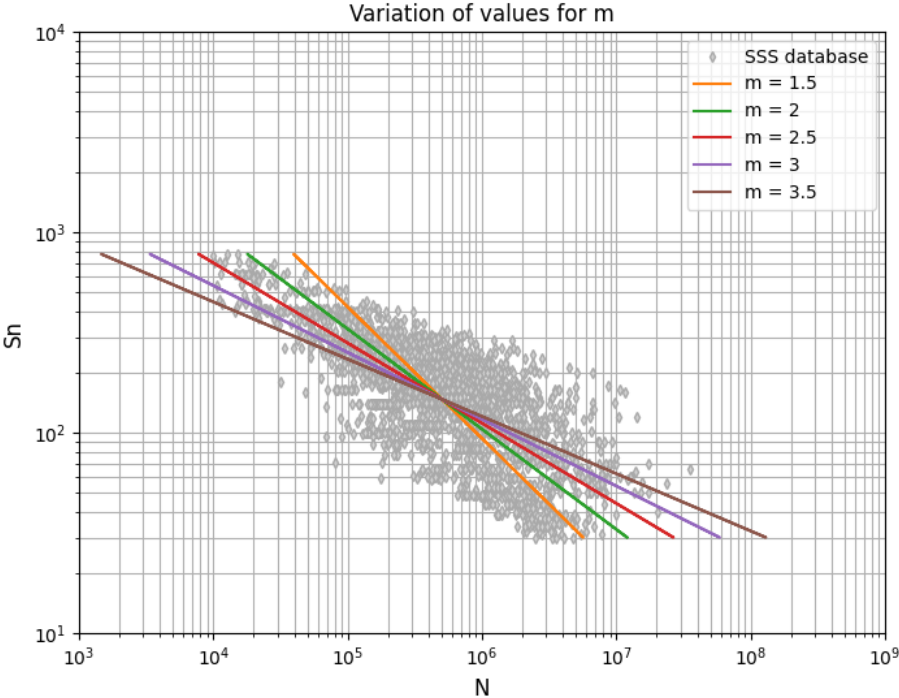


Figure 6.3: Curves with a varying slope

**6.1.2. Large-scale specimen database**

The displayed SSS fatigue data scatter band will be compared with the database mentioned in section 5.2. The database is shown in figure 6.4, and the first comparisons can be made. The figure reveals the placement of double-sided (DS) T-joints near the lower extremity, with the DS longitudinal attachments slightly higher and the cruciform joints positioned just above them. While this subtle pattern is noticeable, drawing definitive conclusions from the figure is challenging due to other influencing factors, such as HS-type, plate thickness, and load ratio.

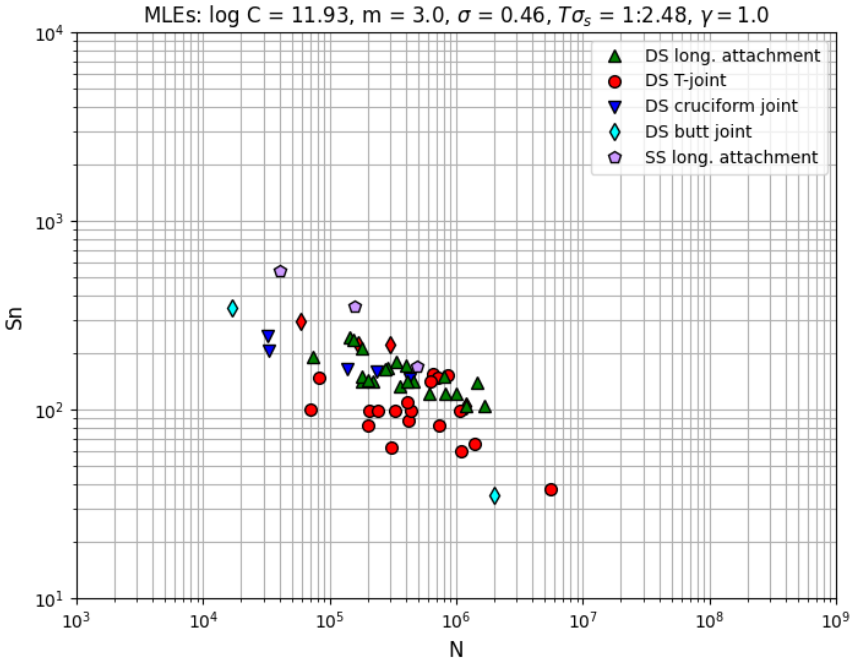
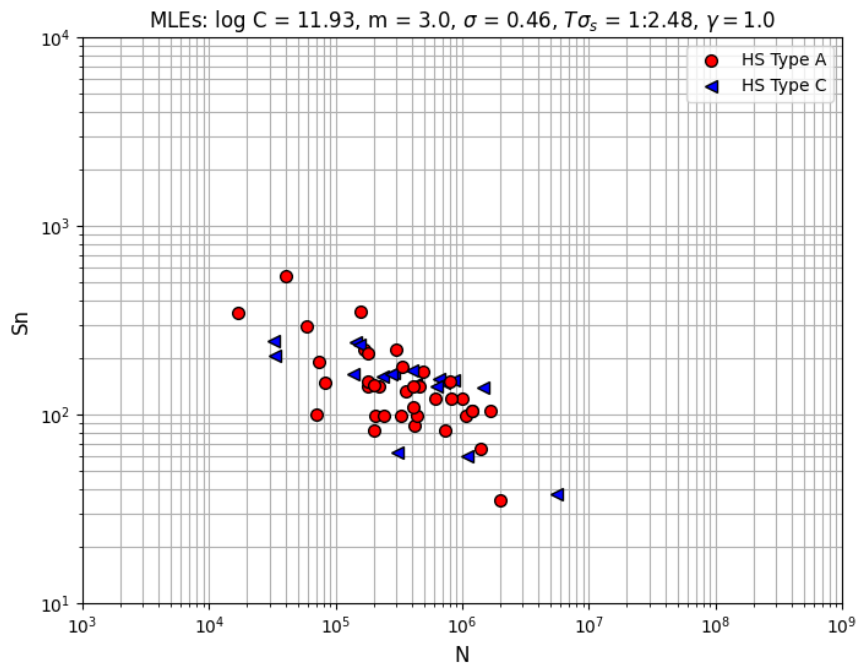


Figure 6.4: Large-scale specimen database by joint type

Figure 6.5 illustrates the LSS database, now categorized specifically into hot spot types A and C. Notably, the dataset lacks any instances of hot spot type B. The distribution of data points, especially for hot spot type A, is quite extensive, complicating the identification of clear trends or the formulation of definitive conclusions. Additionally, no distinct trends are observable between the hot spot types, as both types appear intermixed on the graph.



**Figure 6.5:** Large-scale specimen database by HS-type

In figure 6.6 the data is divided into three distinct groups based on plate thickness: under 10 mm, between 10 and 15 mm, and between 15 and 20 mm. Upon examination of the individual data points, a noticeable intermixing is observed, suggesting a diverse distribution. However, the mean curves exhibit a discernible pattern, aligning in ascending order from larger to smaller plate thickness, with the greater plate thicknesses situated at the lower end. So for nominal stress, the fatigue strength decreases as the plate thickness increases. This trend is in line with the expected geometrical size effect and is also supported in Qin et al. (2019).

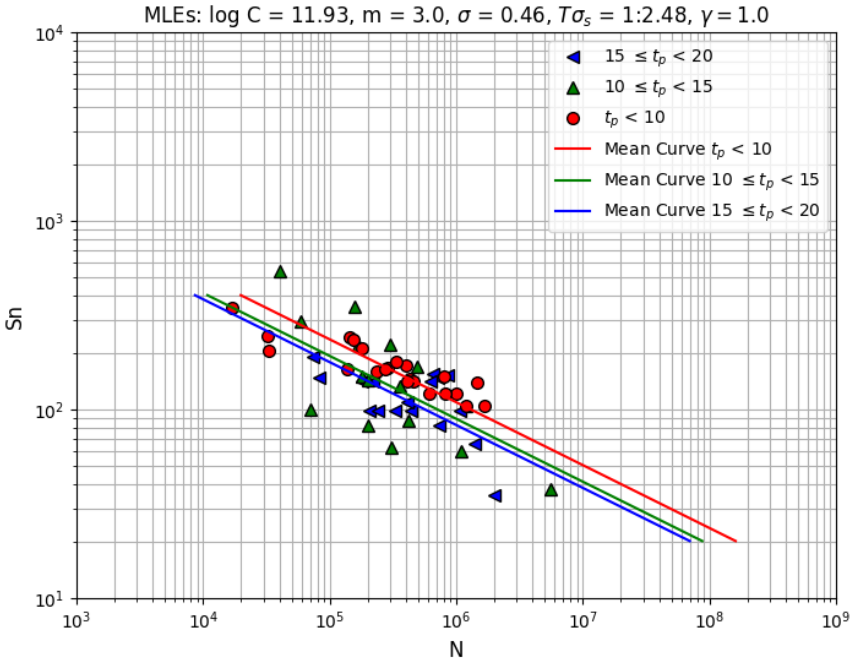


Figure 6.6: Large-scale specimen database by plate thickness

In figure 6.7 the data is organized based on their experienced load ratios. The load ratios span from -1 to 0.3, and a general trend emerges where the mean curves of higher load ratios are predominantly positioned at higher points, while lower load ratios are situated lower down. This trend broadly corresponds with expectations. If a cycle is spent more time in tensile loading, it negatively affects the fatigue strength. However, it's noteworthy that occasional deviations from this pattern occur, this could be attributed to the limited amount of data points, as there is only one data point available for a load ratio of -1,1.

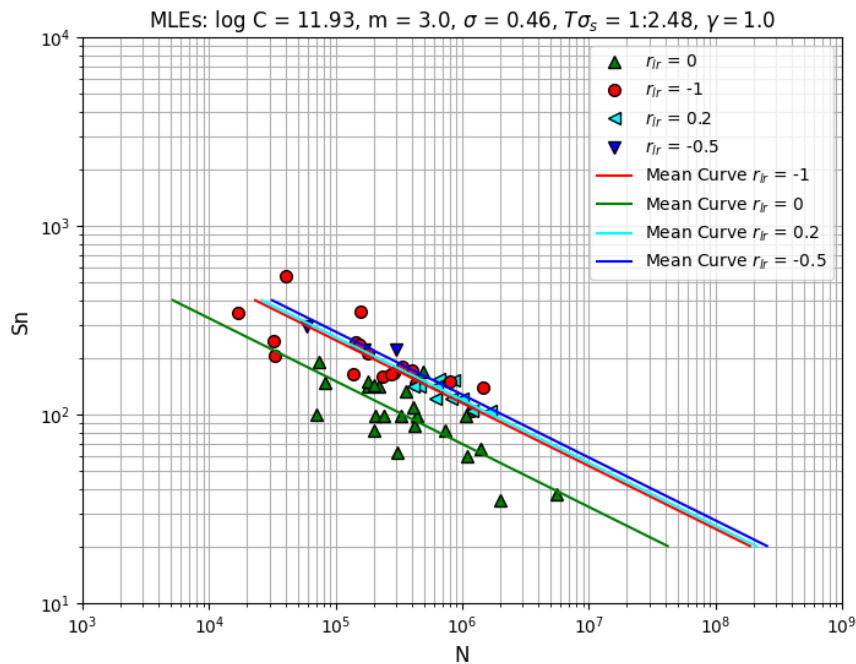


Figure 6.7: Large-scale specimen database by load ratio

### 6.1.3. Database comparison

Having explored both the small-scale and large-scale databases, the next phase of the nominal stress analysis involves a comprehensive comparison between the two. The goal of this analysis is to determine the presence or absence of overlap between the large-scale and small-scale databases and to provide insights into the reasons behind any observed patterns or differences.

The size of both large-scale and small-scale specimen databases significantly influences the outcomes of this comparison. A larger database boosts statistical reliability by providing a greater number of data points, enabling more precise identification of trends and conclusions. Furthermore, it enhances representativeness by encompassing a broader spectrum of species and variations and therefore mitigating potential biases in the results. Also, smaller databases are susceptible to overfitting, where conclusions may excessively incorporate outliers, compromising the overall validity of the conclusions. Moreover, smaller datasets are more vulnerable to errors, as the impact of individual inaccuracies is amplified.

While the large-scale database captures significantly fewer data points, it provides a diverse range of joint types, HS-types, and load ratios to still be able to conclude from the findings. The small-scale database is much more extensive and will serve as a valuable reference frame for comparing the LSS.

Figure 6.8 displays the SSS database and the LSS database together in one figure. At first glance, the large-scale database exhibits a notable alignment with the small-scale database, suggesting a fit with some minor exceptions. These exceptions are mostly in the low MCF domain. While this alignment might hint at potential patterns or correlations, it is essential to make such observations cautiously. It is plausible that the apparent coherence between the overlaid and extensive dataset is more coincidental than indicative of a meaningful trend. The coincidental fit can be a result of the great amount of scatter that is present in both of the data sets, especially in the SSS scatter band.

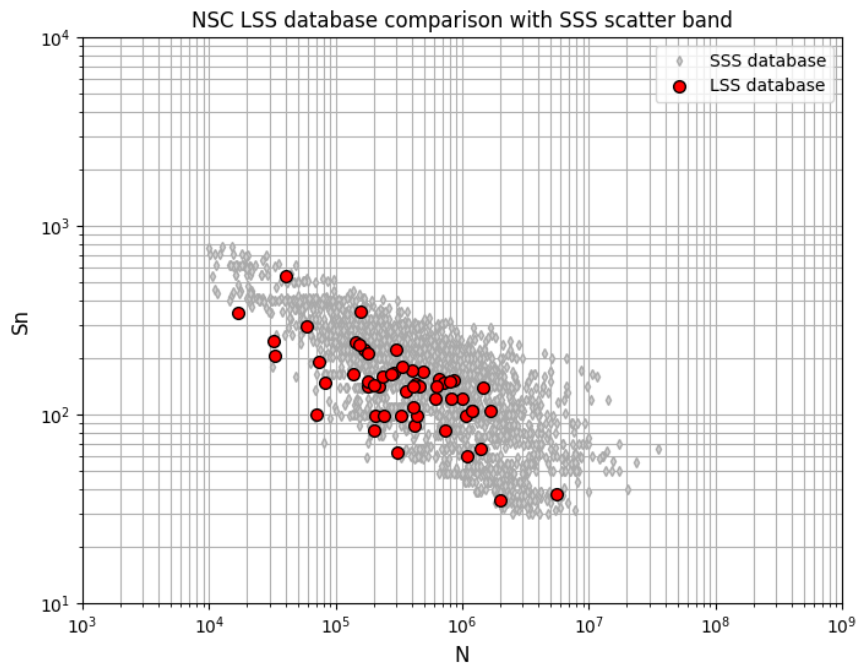


**Figure 6.8:** Large-scale & small-scale specimen database nominal stress comparison

However, making a direct comparison of all database entries using the NSC is incorrect. It is incorrect to compare all joint types using the nominal stress concept because the nominal stress does not adequately account for the stress concentration effects present in different joint geometries. Nominal stress assumes uniform stress distribution across the entire cross-section of a specimen, neglecting the localized stress amplification that occurs at geometric irregularities such as notches, fillets, and holes.

Different joint types have varying geometries and stress concentration factors, leading to significant disparities in stress distribution and severity of stress concentrations. Therefore, comparing them solely based on nominal stress would overlook these critical factors, potentially resulting in inaccurate assessments of their structural integrity and performance (Barsoum et al., 2012).

Instead, it's possible to compare the same joint types of the small- and large-scale databases. Figures 6.9 to 6.13 show a comparison for all different joints that are present in both databases. For the DS cruciform joints and DS longitudinal attachments, the curves generally align well, with the LSS mean curve positioned slightly below the SSS mean curve. However, for the DST-joints, there is considerable scatter. The other figures also exhibit significant deviations; however, these deviations are based on data from only two and one specimen in the LSS database, respectively, making it difficult to draw meaningful conclusions.

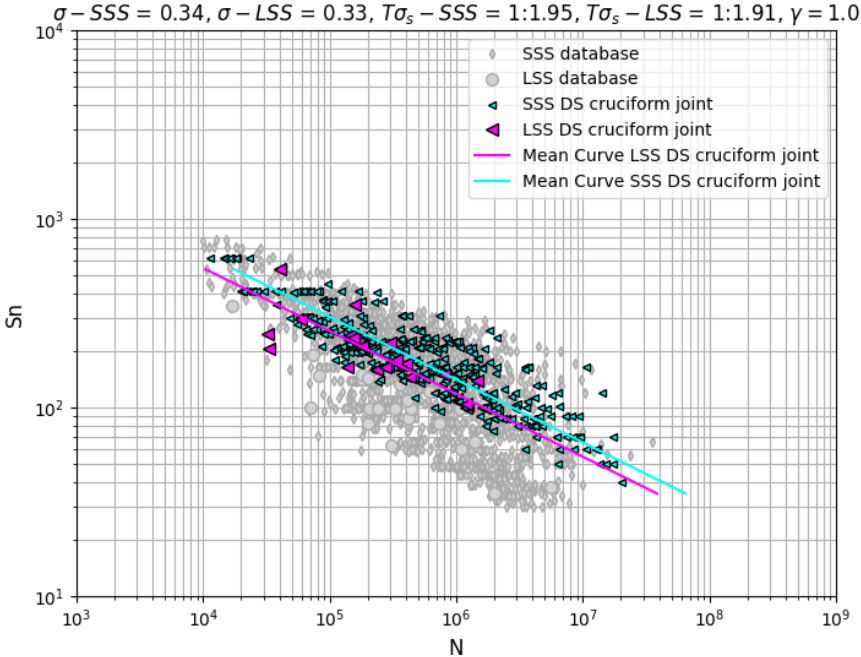


Figure 6.9: Large-scale & small-scale specimen DS cruciform joint comparison

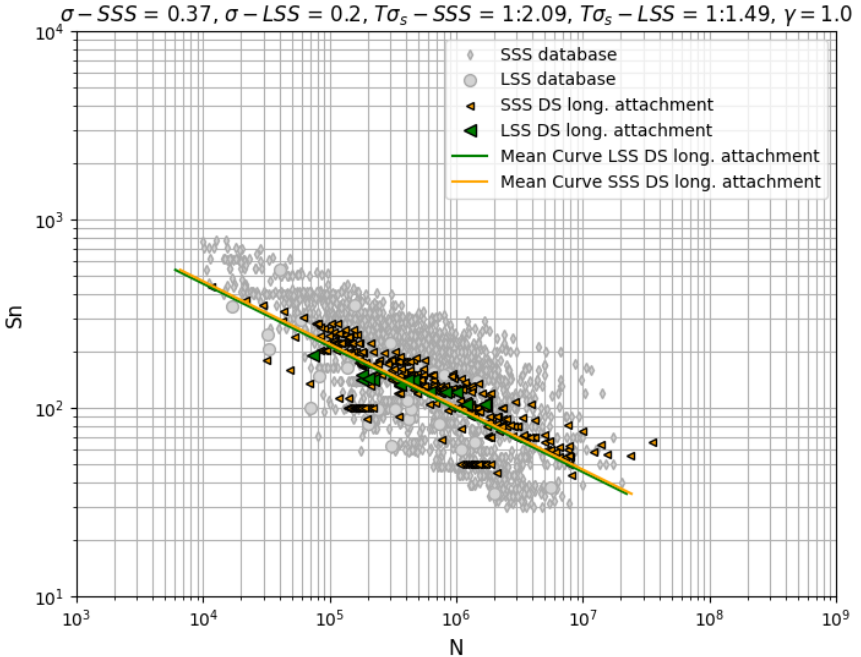


Figure 6.10: Large-scale & small-scale specimen DS longitudinal attachment comparison

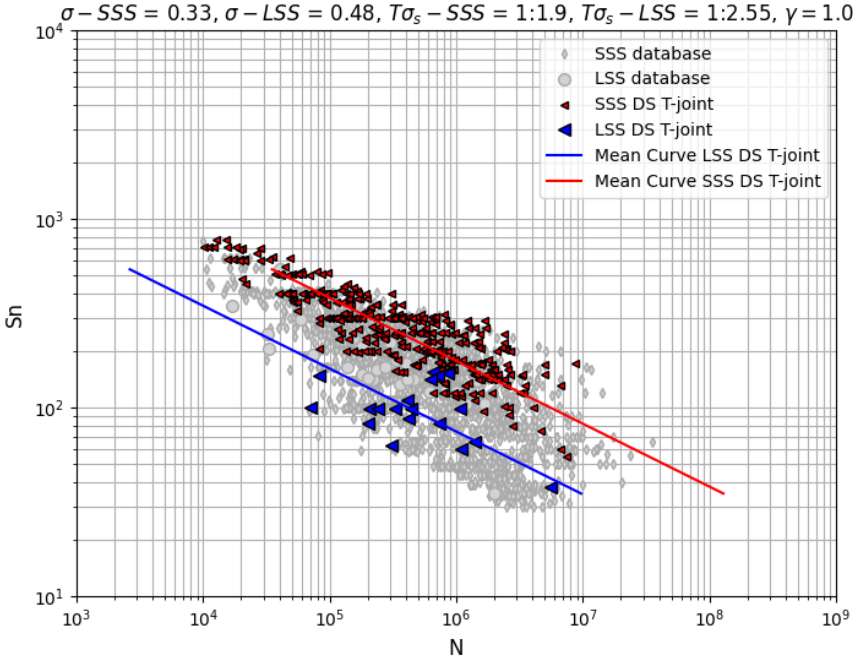


Figure 6.11: Large-scale & small-scale specimen DS T-joint comparison

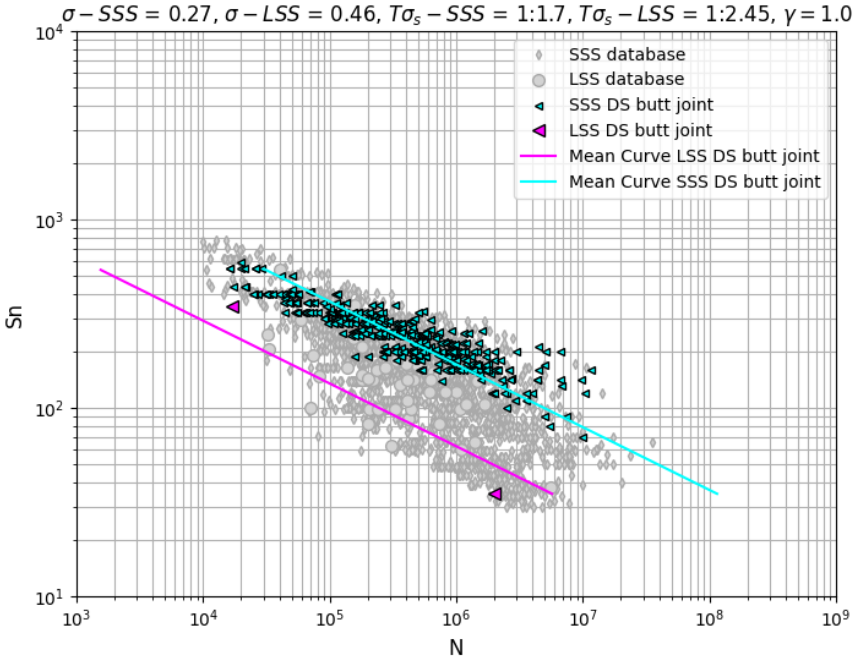
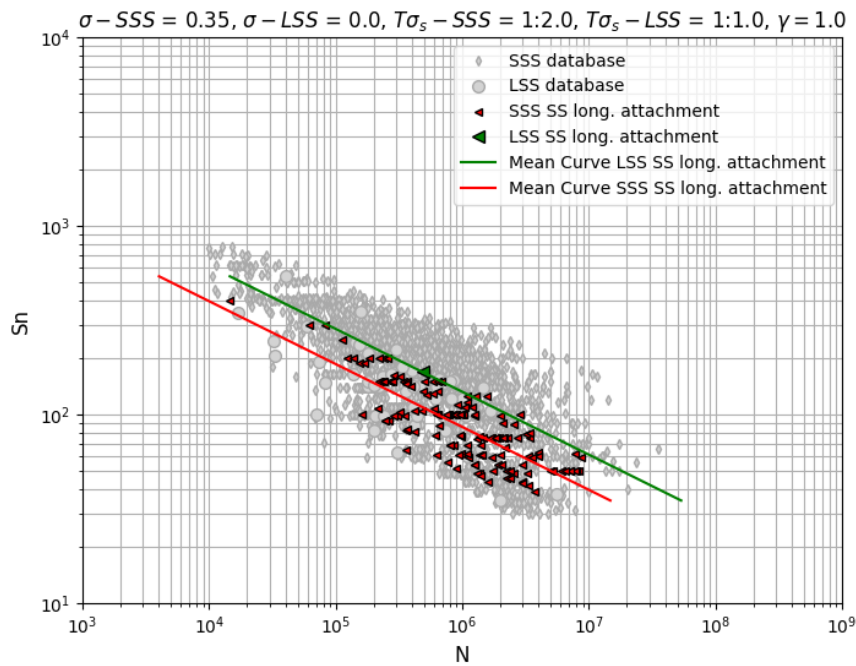


Figure 6.12: Large-scale & small-scale specimen DS butt joint comparison



**Figure 6.13:** Large-scale & small-scale specimen SS longitudinal attachment comparison

Table 6.1 show the scatter parameters for the small- and large-scale specimen database, separated for each joint type.

**Table 6.1:** Scatter parameters comparison for the different joints

Joint type	$\sigma - SSS$	$T\sigma_s - SSS$	$\sigma - LSS$	$T\sigma_s - LSS$
DS cruciform joint	0.34	1:1.95	0.33	1:1.91
DS long. attachment	0.37	1:2.09	0.2	1:1.49
DS T-joint	0.33	1:1.9	0.48	1:2.55
DS butt joint	0.27	1:1.7	0.46	1:2.45
SS long. attachment	0.35	1:2.0	-	-

## 6.2. Hot spot structural stress concept

In this section, the databases will be tested and compared using the HSSSC. Subsection 6.2.1 will cover the SSS database, while the LSS database will be discussed in Subsection 6.2.2. A comparison will be made in Subsection 6.2.3.

### 6.2.1. Small-scale scatter band

Figure 6.14 shows the hot spot structural stress SSS database without run-outs. At first glance, it can already be seen that the database is less spread out. To construct the HSSSC database, FE models were made for all specimens to perform calculations. To calculate the hot spot stress, the structural stress method by Dong (2001) was used.

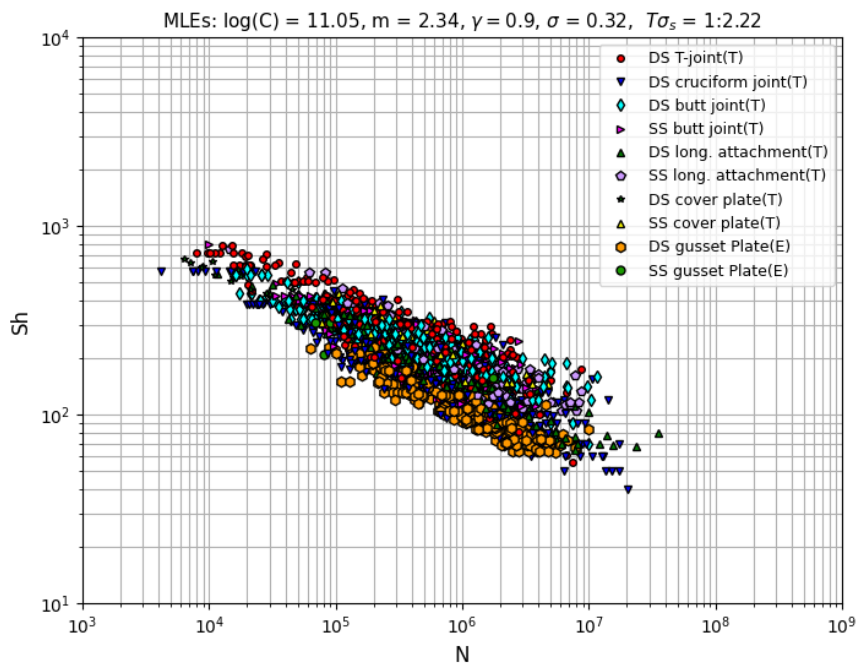


Figure 6.14: HSSSC SSS database scatter band

### 6.2.2. Large-scale specimen data points

As explained in section 2.2 there are multiple ways to calculate the stress in the hot spot. In this analysis, four out of the five mentioned methods will be used, as only these are suitable for use with shell elements. The sub-surface stress evaluation will be dropped as it is only possible with a solid model. This paragraph will cover the different methods and calculations per large-scale specimen, with references to the appendix for more extensive calculations.

#### Bilge corner

First, the bilge corner from a Ro-Ro ship from Subsection 5.2.1 will be examined using linear surface extrapolation. The DNV (2021a) advises extrapolating from  $3t_p/2$  and  $t_p/2$  to the hot spot. The mesh size was reduced locally around the hot spot to acquire converged results. The results are visible in table 6.2. The values are the stresses in MPa for a reference stress equal to 1 MPa. The resulting hot spot stress for this method is 6.3 MPa.

Table 6.2: Results linear extrapolation of the bilge corner

Mesh size [mm]	Stress at $3t_p/2$ [MPa]	Stress at $t_p/2$ [MPa]	Hot spot stress [MPa]
6	2.1	5.2	6.7
3	1.9	4.9	6.4
1.5	2.0	5.0	6.5
0.75	1.8	4.8	6.3
0.375	1.8	4.8	6.3

Figure 6.15 shows the linear extrapolation that is made. The zero on the x-axis means the location of the hot spot. The figure shows that the stress towards the hot spot increases exponentially, at least in the FE model. Figure 6.16 displays a detail of the hot spot in the finite element model.

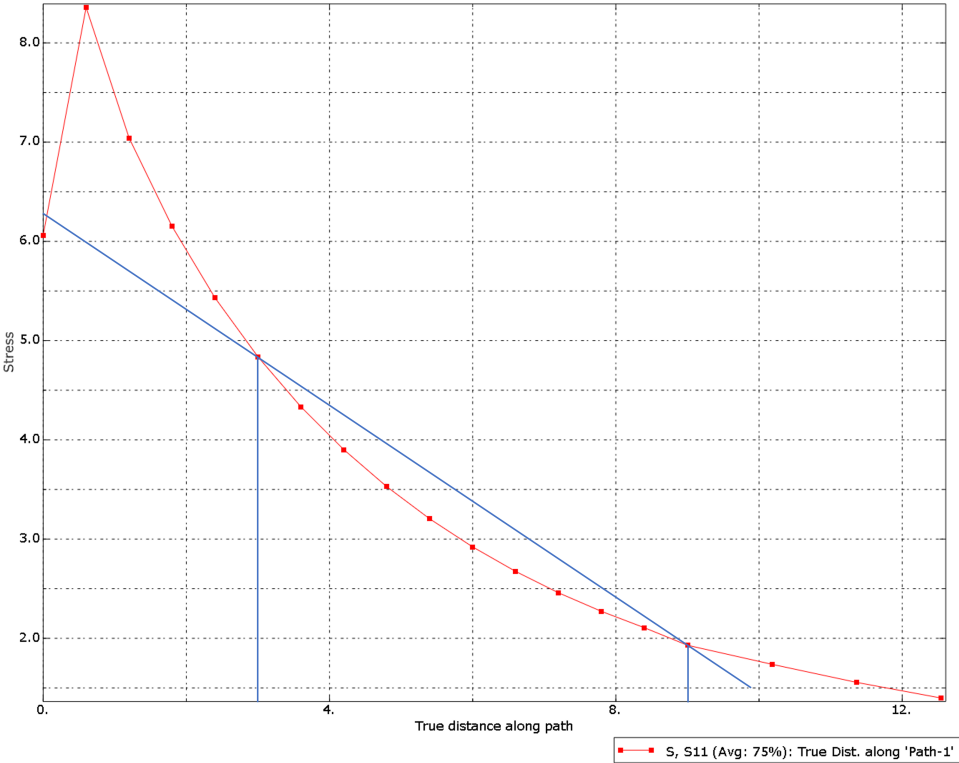


Figure 6.15: Stress distribution on the path towards the hot spot on the bilge corner

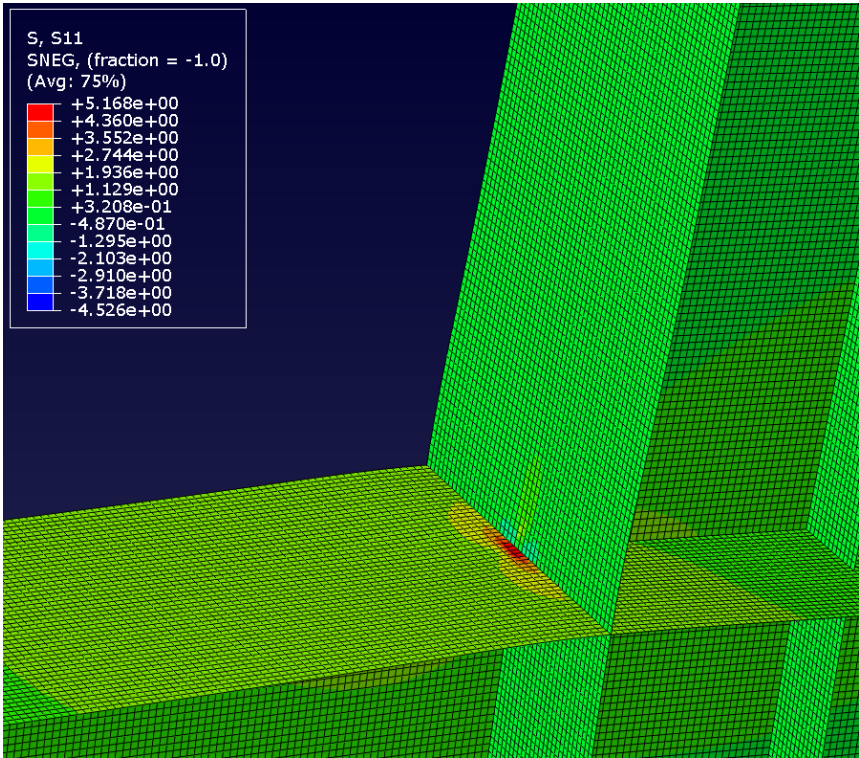


Figure 6.16: FEM detail of the hot spot

The next method that is advised by DNV is the derivation of stress at a read out point  $t_p/2$  from the hot spot

time a coefficient. The coefficient is depended on the joint type and location of the hot spot. For a weld toe on a flange, this coefficient is equal to 1.12. The formula from DNV (2021a) is shown in equation (6.2). For the stress at  $t_p/2$  the converged value of from table 6.2 is taken. The resulting hot spot stress is equal to 5.4 MPa.

$$\sigma_{HS} = 1.12 \cdot \sigma \quad (6.2)$$

A method that is advised by the IIW is non-linear surface extrapolation with read-out points at  $0.4t_p$ ,  $0.9t_p$ , and  $1.4t_p$  (Hobbacher, 2016). The formula is given in equation (6.3). For this method a mesh size of  $0.1t_p$  was used to ensure nodes were present at the desired read out points. Due to the calculation time, only a convergence test was performed with a mesh size of  $0.05t_p$  which showed converged results. The stresses at  $0.4t_p$ ,  $0.9t_p$ , and  $1.4t_p$  were 4.9, 3.2, and 1.8 MPa respectively. Using equation (6.3), the hot spot stress is equal to 6.5 MPa.

$$\sigma_{HS} = 2.52 \cdot \sigma_{0.4t_p} - 2.24 \cdot \sigma_{0.9t_p} + 0.72 \cdot \sigma_{1.4t_p} \quad (6.3)$$

The last method that will be used for this research is the through-thickness linearization. This method is based on the structural stress definition by Dong (2001). This definition proposes a structural stress definition at the weld toe, based on a membrane component ( $\sigma_m$ ) and bending component ( $\sigma_b$ ). A visualization is given in figure 6.17.

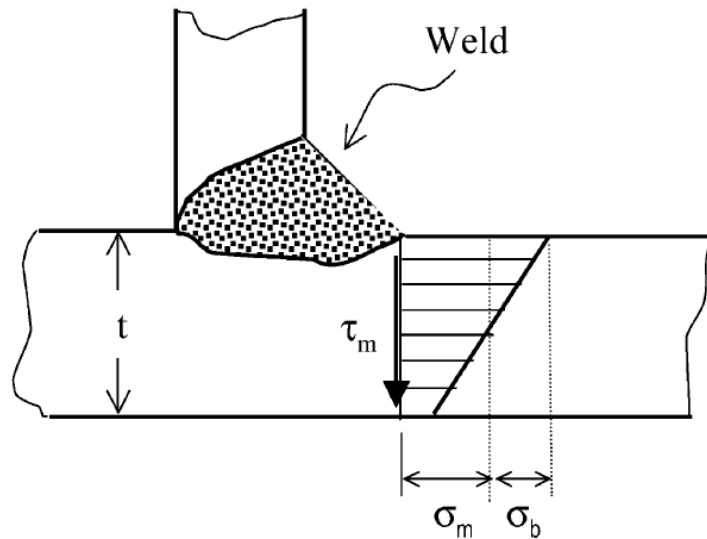


**Figure 6.17:** Visual representation of the structural stress method (Dong, 2001)

The method uses the element nodal forces and moments ( $F_n$ ,  $M_b$ ) and transforms them into line forces and moments ( $f'_n$ ,  $m'_b$ ). This transformation into line forces and moments differs depending on the hot spot type in question. A more extensive calculation, along with a convergence study, can be found in appendix B. The line forces and moments are the input in equation (6.4) to calculate the hot spot structural stress. For this specimen,  $\sigma_m$  and  $\sigma_b$  are respectively 1.8 and 4.6 MPa, giving a structural stress ( $\sigma_s$ ) of 6.4 MPa.

$$\sigma_s = \sigma_m + \sigma_b = \frac{f'_x}{t_p} + \frac{6(m'_y + \delta \cdot f'_z)}{t_p^2} \quad (6.4)$$

A summary of all hot spot stress results has been given in table 6.3. The results are in good agreement with each other, apart from the second method which turns out to be lower than the others. In the DNV (2021a), no reason was found for the coefficient to have a value of 1.12. The stress distribution within this hot spot likely exhibits a steeper gradient compared to the specimens used as references for this value.

**Table 6.3:** Results hot spot stress calculations of the bilge corner

Method	Hot spot stress [MPa]
Linear extrapolation	6.3
Stress at $0.5t_p$ times coefficient	5.4
Non-linear extrapolation	6.5
Through-thickness linearization	6.4

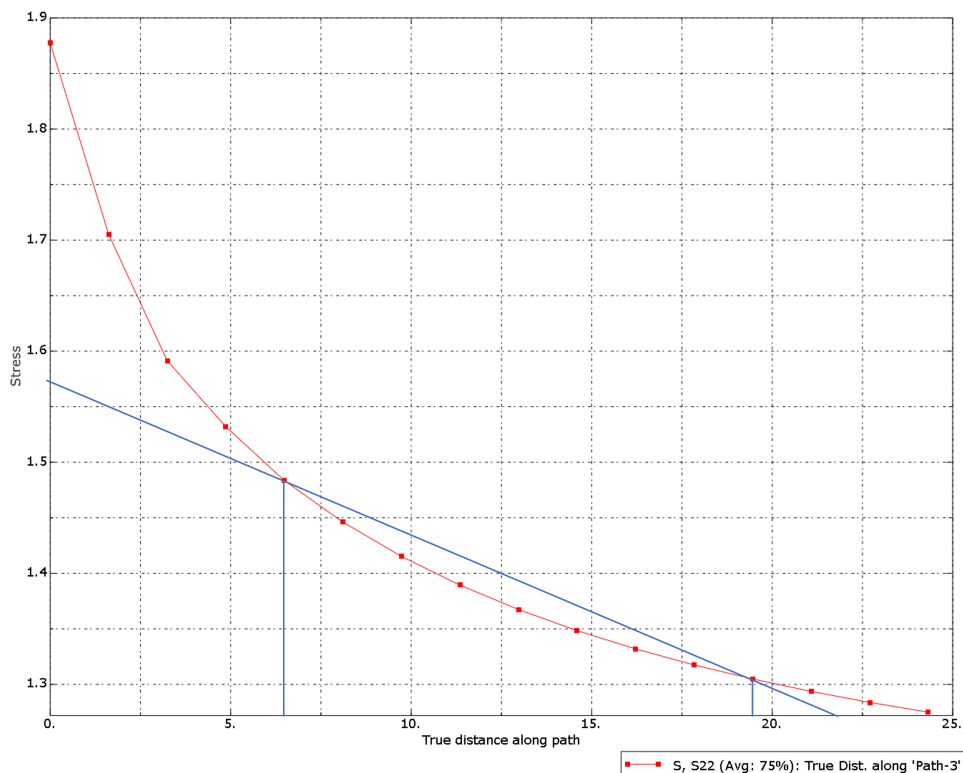
### T-shaped stiffener

Next is the T-shaped stiffener from Subsection 5.2.2. This subsection will follow the same layout as the previous, so the first calculation that will be done is the linear extrapolation. The results have been given in table 6.4 for different mesh sizes until the results converged. The converged hot spot stress is equal to 1.5 MPa for a reference stress of 1 MPa.

**Table 6.4:** Results linear extrapolation of the T-shaped stiffener

Mesh size [mm]	Stress at $3t_p/2$ [MPa]	Stress at $t_p/2$ [MPa]	Hot spot stress [MPa]
13	1.1	1.5	1.7
6.5	1.3	1.4	1.5
3.25	1.4	1.5	1.6
1.625	1.4	1.5	1.6

Figure 6.18 shows the linear extrapolation that is made. Also here, the zero on the x-axis is equal to the hot spot location.

**Figure 6.18:** Stress distribution on the path towards the hot spot on the T-shaped stiffener

In the next method, the converged stress at  $0.5t_p$  will be multiplied by 1.12, following equation (6.2). This results in a hot spot stress of 1.7 MPa.

The next method is the non-linear extrapolation. A mesh size of  $0.1t_p$  was used, and a mesh size of  $0.05t_p$  to check for convergence. The stresses at  $0.4t_p$ ,  $0.9t_p$ , and  $1.4t_p$  were 1.4, 1.1, and 1.0 MPa respectively. Using equation (6.3), the hot spot stress is equal to 1.6 MPa.

The final method is once again the structural stress calculation, however, it differs from the calculation used in the previous subsection as this specimen has a hot spot type A. Now, the virtual node method by Dong (2003) will be used. This method places a virtual node at a distance  $L_1$  away from the weld. At this node the line force and moment will be calculated. Which is then put into equation (6.5). The full calculation is given in appendix B. For the T-shaped stiffener,  $\sigma_m$  and  $\sigma_b$  are respectively 1.0 and 0.6 MPa, giving a structural stress ( $\sigma_s$ ) of 1.6 MPa.

$$\sigma_s = \sigma_m + \sigma_b = \frac{f'_x}{t_p} + \frac{6 \cdot m'_y}{t_p^2} \quad (6.5)$$

A summary of all hot spot stress results has been given in table 6.5. The results are in good agreement with each other, even though they are different simplifications of reality and some deviation was to be expected. This is not the case here.

**Table 6.5:** Results hot spot stress calculations of the T-shaped stiffener

Method	Hot spot stress [MPa]
Linear extrapolation	1.6
Stress at $0.5t_p$ times coefficient	1.7
Non-linear extrapolation	1.6
Through-thickness linearization	1.6

### Scallop

Lastly are the hot spot calculations for the scallop specimen from Subsection 5.2.3. To begin with is the linear extrapolation calculation. The results are displayed in table 6.6. The results converged to a hot spot stress of 1.7 MPa with a reference stress of 1 MPa.

**Table 6.6:** Results linear extrapolation of hot spot stress for the scallop

Mesh size [mm]	Stress at $3t_p/2$ [MPa]	Stress at $t_p/2$ [MPa]	Hot spot stress [MPa]
9	1.2	1.6	1.9
4.5	1.2	1.7	2.0
2.25	1.2	1.6	1.8
1.125	1.3	1.5	1.7
0.5625	1.3	1.5	1.7

Figure 6.19 shows the linear extrapolation that has been done. The stress increases exponentially as the stress gets closer to the hot spot. This figure would make believe the linear extrapolation does not quite catch the stress at the hot spot. However, the hot spot is modeled as a hard point where a singularity exists. At this point, the stress will always increase. A detail of the hot spot in the finite element model is shown in figure 6.20.

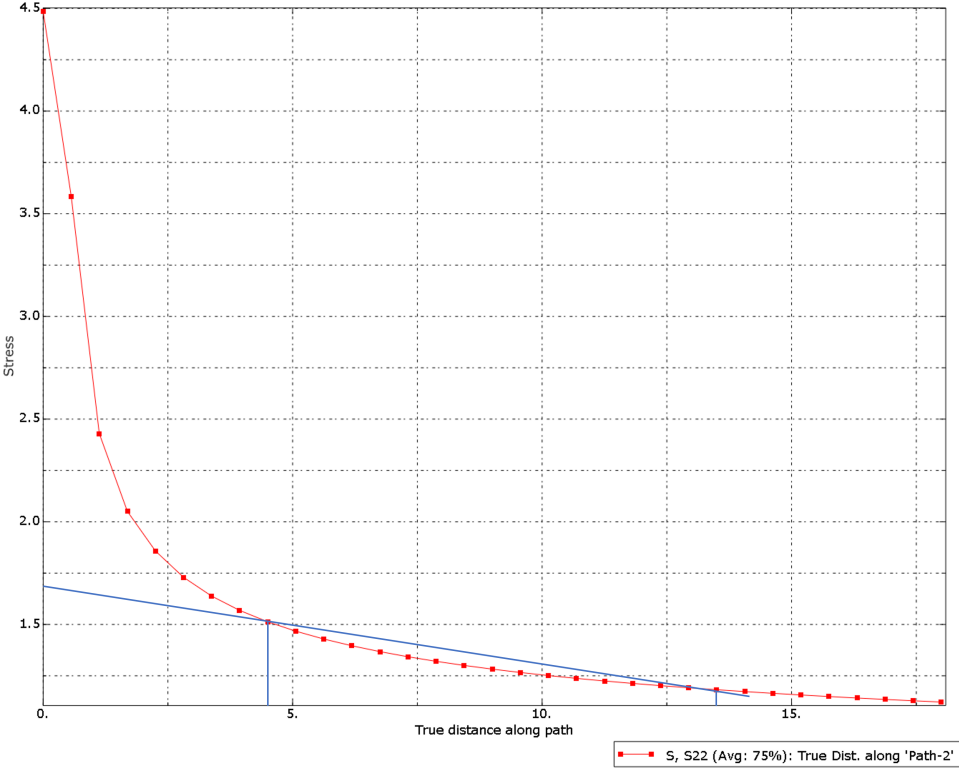


Figure 6.19: Stress distribution on the path towards the hot spot on the scallop

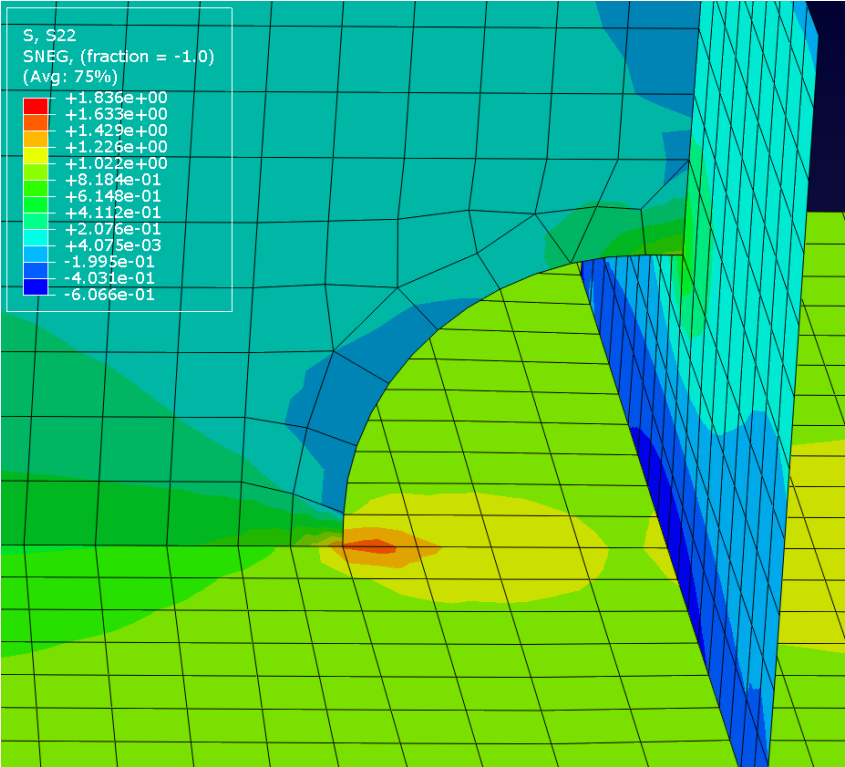


Figure 6.20: FEM detail of the hot spot

In the following method, the converged stress at  $0.5t_p$  will be multiplied by 1.12, as per equation (6.2). This

results in a hot spot stress of 1.7 MPa.

The next method is again the non-linear extrapolation. A mesh size of  $0.1t_p$  was used, as well as a mesh size of  $0.05t_p$  to check for convergence. The stresses at  $0.4t_p$ ,  $0.9t_p$ , and  $1.4t_p$  were 1.6, 1.3, and 1.1 MPa respectively. Using equation (6.3), the hot spot stress is equal to 1.8 MPa. 6.3

The final method is the structural stress calculation, once again with the help of a virtual node. The full calculation is given in appendix B. For the scallop, the stress due to bending was negligible,  $\sigma_m$  and  $\sigma_b$  are respectively 1.4 and 0.0 MPa, giving a structural stress ( $\sigma_s$ ) of 1.4 MPa.

A summary of all the hot spot stress results is shown in table 6.7. The methods by DNV (2021a) matches well with each other, but the through-thickness linearization gives slightly lower results. This difference is because each method defines structural stress differently and offers an estimate of it. The method by Dong (2001) is less affected by high surface stresses compared to the DNV-GL methods because it considers the stress distribution across the thickness of the plate, while the DNV-GL methods only focus on surface stresses.

**Table 6.7:** Results hot spot stress calculations for the scallop

Method	Hot spot stress [MPa]
Linear extrapolation	1.7
Stress at $0.5t_p$ times coefficient	1.7
Non-linear extrapolation	1.8
Through-thickness linearization	1.4

### Concluding remarks

Four methods have been used to calculate the stress at the hot spot. This has been done to test if they agree with each other and to keep a link to the methods that are currently widely used in practice. However, to compare the LSS data points with the SSS database, the structural stress method by Dong (2001) will be used for the remainder of this research. This is because the SSS database is constructed with this method as well and otherwise a comparison is impossible. Table 6.8 displays the  $K_s$  values, with  $K_s$  defined as  $S_h/S_n$ , for the three specimens using the through-thickness linearization. These are the values that will be used in the database comparison in the following paragraph.

**Table 6.8:** The  $K_s$  factors for all three specimens

Specimen	$K_s$
Bilge corner	6.4
T-shaped stiffener	1.6
Scallop	1.4

### 6.2.3. Database comparison

The results from the HSSSC for the LSS have been plotted in figure 6.21. It can be seen that the high  $K_s$  value for the bilge corner has its effect. The data points lie way above the SSS scatter band, saying that there would be no fatigue similarity between the bilge corner specimen and the small-scale specimens. The remaining data points do fall into the scatter band. The data points from the T-shaped stiffener lie more in the upper range, while the data points from the scallop are almost perfectly centered. These data points do show fatigue resistance similarity between the small- and large-scale specimens.

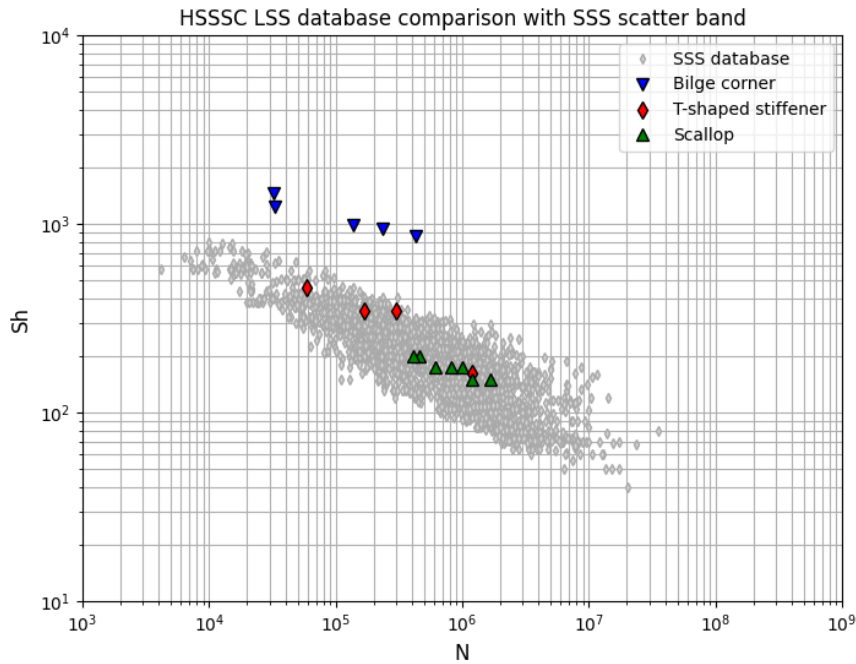


**Figure 6.21:** SSS and LSS comparison hot spot structural stress

Table 6.9 shows the scatter parameters for the HSSSC, divided into load-carrying (LC) and non-load-carrying (NLC). As the results for the bilge corner lie so far out of the scatter band, the data points are not considered in the table.

**Table 6.9:** Scatter parameters large-scale specimens for the HSSSC

HSSSC	$\sigma - LSS$	$T\sigma_s - LSS$
LC	0.14	1:1.36
NLC	0.1	1:1.11

### 6.3. Effective notch stress concept

In this section, the databases will be tested and compared using the ENSC. Subsection 6.3.1 will cover the SSS database, and Subsection 6.3.2 will discuss the LSS database. But first, the ENSC will be explained in more detail.

Section 2.3 explained that there are multiple methods to calculate the effective notch stress ( $S_e$ ), however for this research the averaged effective notch stress will be adopted. Qin et al. (2019) showed that the AENSC had reduced scatter compared to the artificial notch method and used this method to construct the SSS database. As this research will make comparisons to that database, the same method will be adopted.

Typically, a solid FE solution is required to obtain an averaged effective notch stress. However, the weld notch stress distribution by den Besten (2015) can also be used. The approach comprises an analytical through-thickness weld notch stress distribution ( $\sigma_n$ ) which is then averaged over the material-characteristic micro-structural support length  $\rho^*$ , as can be seen in equation (6.6).

$$\sigma_e = \frac{1}{\rho^*} \int_0^{\rho^*} \sigma_n(r) dr \quad (6.6)$$

The effective notch stress is a function of  $S_e = f(\rho^*, t_p, \sigma_s, r_s, C_{bw}, \alpha, \beta)$  with:

- $\rho^*$  Micro-structural support length
- $t_p$  Plate thickness
- $\sigma_s$  Structural field stress distribution
- $r_s$  Structural bending stress ratio ( $\sigma_b/\sigma_s$ )
- $C_{bw}$  Weld load carrying stress coefficient
- $\alpha$  Half of the notch angle
- $\beta$  Stress angle

The weld load carrying stress coefficient ( $C_{bw}$ ) is an analytically described function of the base plate thickness ( $t_b$ ), the connecting plate thickness ( $t_c$ ), weld leg height ( $h_w$ ) and weld leg length ( $l_w$ ). These and other parameters are visualized in figure 6.22.

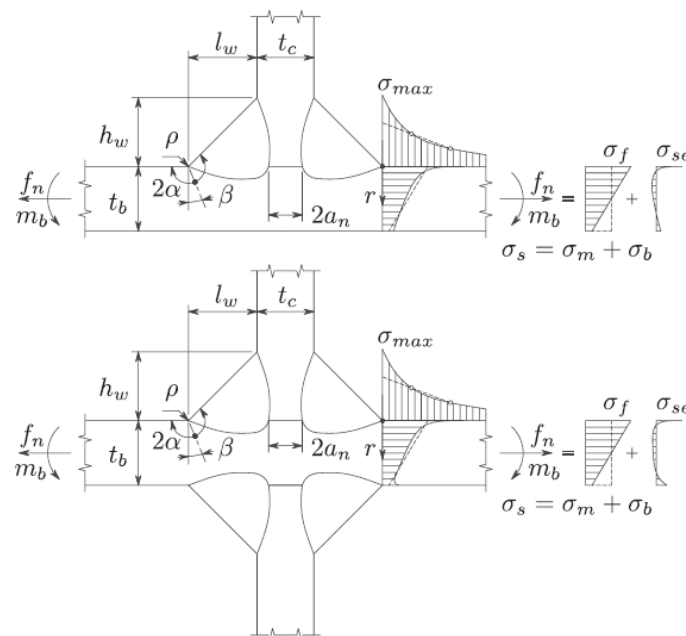


**Figure 6.22:** Sketch with input parameters for the ENSC (Qin et al., 2019)

The structural stress distribution obtained from the HSSSC is an input parameter for the ENSC. That is why the ENSC is a follow-up to the HSSSC, and since the SSS database uses the structural stress by Dong (2003) as an input for the ENSC, the structural stress found in section 6.2 will be used to create the large-scale specimen data points as well.

### 6.3.1. Small-scale database

Figure 6.23 displays the effective notch stress SSS database without any run-outs. Upon initial examination, it becomes evident that the database exhibits less scatter. In the case of the ENSC SSS scatter band, the  $\sigma$  and  $T_{\sigma_s}$  values stand at 0.21 and 1:1.49 respectively. Also, a visual comparison between the scatter bands shows a reduction in scatter, with the ENSC SSS scatter band having the most compact scatter band.

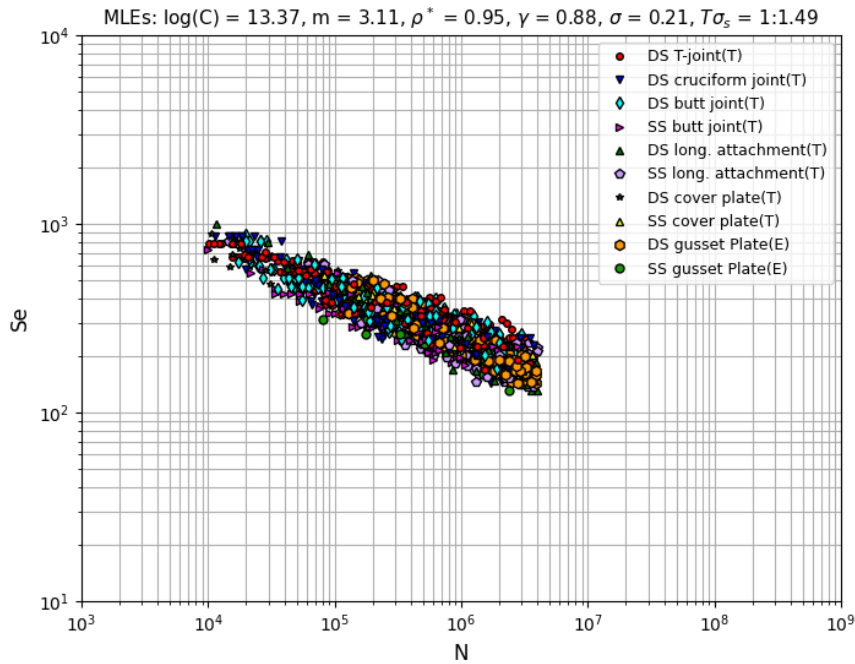


Figure 6.23: ENSC SSS database scatter band

### 6.3.2. Large-scale specimen data points

Previously, the method of calculating the effective notch stress was explained. This paragraph will cover the calculations and results for the individual large-scale specimens.

#### Bilge corner

As a first step to calculating the effective notch stress, it is necessary to create the weld notch stress distribution  $\sigma_n$ . The weld notch stress distribution, for symmetry with respect to  $(t_p/2)$ , is given as (den Besten, 2015; Qin et al., 2019):

$$\begin{aligned} \sigma_n = \sigma_s \left\{ \left[ 1 - 2 \cdot r_s \left\{ 1 - f\left(\frac{r}{t_p} = \frac{1}{2}\right) \right\} \right] f\left(\frac{r}{t_p}\right) \right. \\ \left. + r_s \cdot \left\{ 2f\left(\frac{r}{t_p} = \frac{1}{2}\right) - 1 \right\} \cdot \left[ \left\{ 1 - f\left(\frac{r}{t_p} = \frac{1}{2}\right) \right\} - 2 \cdot \left(\frac{r}{t_p}\right) \right] \right\} \end{aligned} \quad (6.7)$$

In equation (6.7),  $r_s = \sigma_b/\sigma_s$ . Full definitions for  $f\left(\frac{r}{t_p} = \frac{1}{2}\right)$  and  $f\left(\frac{r}{t_p}\right)$  can be found in appendix C. Figure 6.24 displays the weld notch stress distribution for the bilge corner over the base plate thickness  $\frac{r}{t_b}$ , as well as the far field stress distribution  $\sigma_f/\sigma_s$  with  $\sigma_f = \sigma_s \left\{ 1 - 2r_s \left(\frac{r}{t_p}\right) \right\}$ . Dividing the weld notch stress distribution by the structural stress allows for a comparison of the local stress concentration at the weld notch relative to the overall stress state in the component. The weld notch stress distribution does not fully overlap the far-field stress, but the slope is similar.

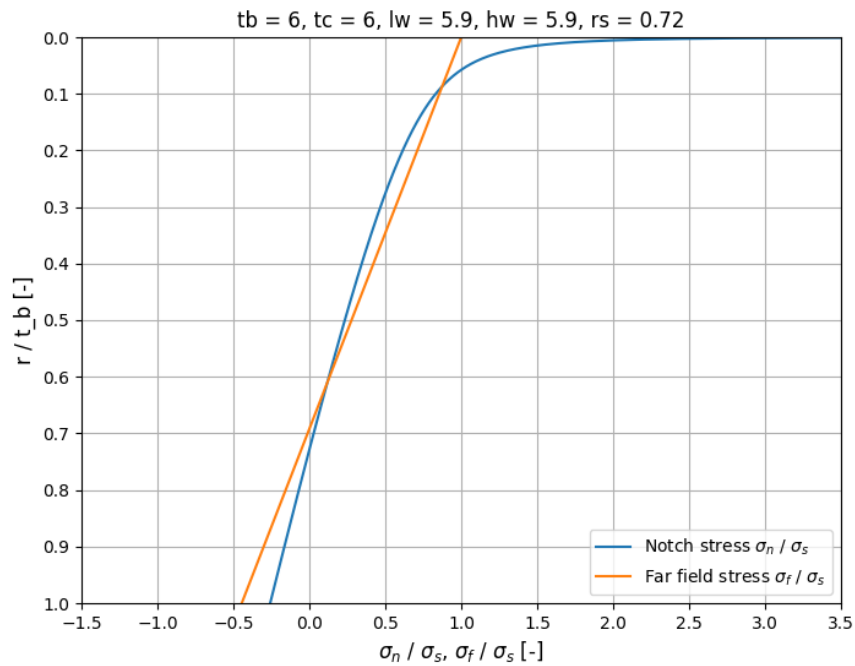


**Figure 6.24:** Notch & far-field stress distribution for the bilge corner

The  $\sigma_n$  distribution will be used to calculate the effective notch stress using equation (6.6). To be able to make a comparison with the SSS database, the same value for  $\rho^*$  will be used, namely  $\rho^* = 0.95$ . The full calculation can be found in appendix C. For the bilge corner, the effective notch stress is equal to 5.3 MPa for a reference stress of 1 MPa.

#### **T-shaped stiffener**

The notch & far-field stress distributions for the T-shaped stiffener have been given in figure 6.25. The distributions do not overlap, but the slope is similar. This dictates that the notch stress is not that dependent on the far field stress.

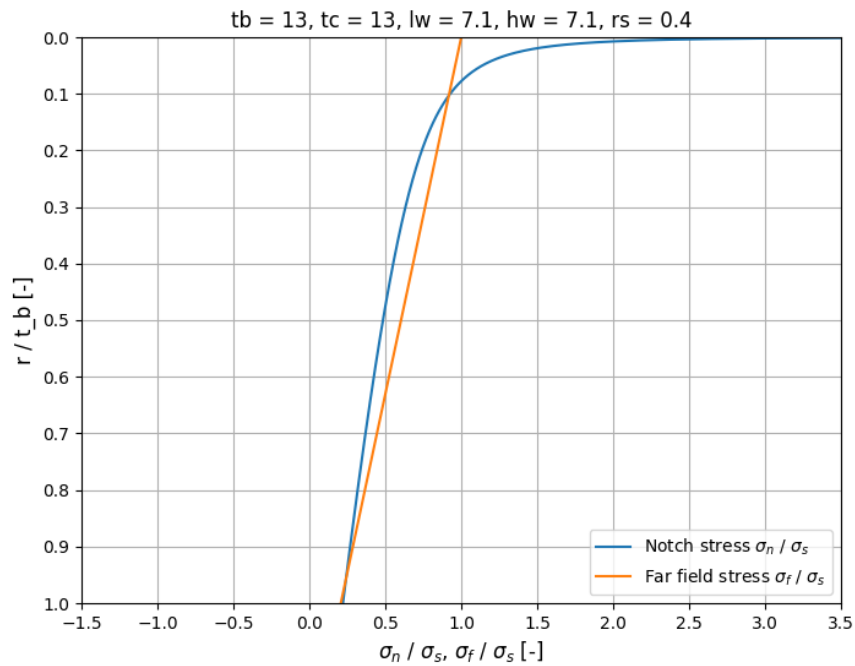


**Figure 6.25:** Notch & far-field stress distribution for the T-shaped stiffener

For this specimen, the effective notch stress has also been calculated with a  $\rho^*$  value of 0.95. The effective notch stress is equal to 2.1 MPa for a reference stress of 1 MPa.

### Scallop

The notch & far-field stress distributions for the T-shaped stiffener have been given in figure 6.26. As the bending stress ratio is near zero, the far field stress is only dependent on the structural stress. This causes the straight line equal to one over the whole thickness. The notch stress distribution starts at its peak in the notch, and gradually finds its equilibrium around 0.7.

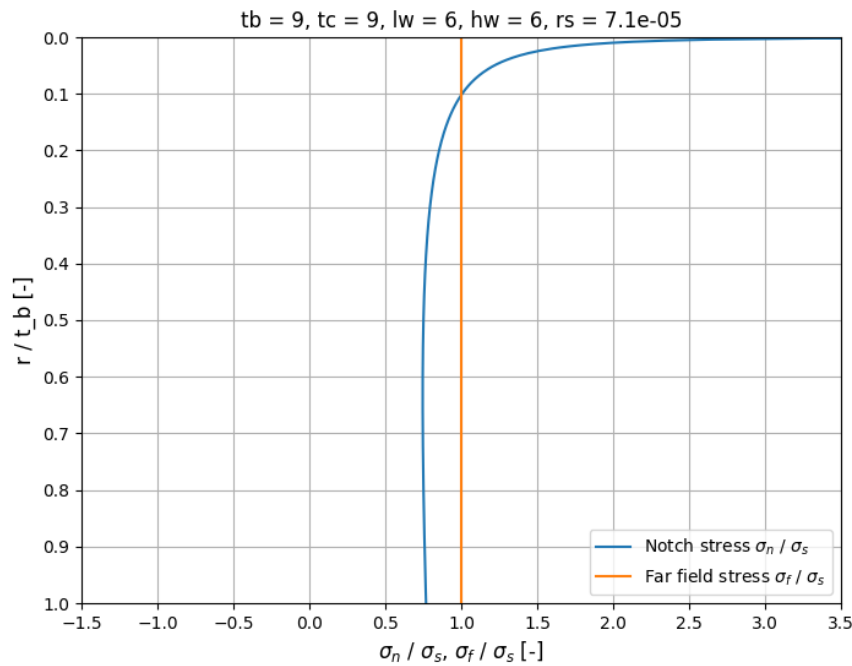


**Figure 6.26:** Notch & far-field stress distribution for the scallop

For the last specimen, the effective notch stress has also been calculated with a  $\rho^*$  value of 0.95. The effective notch stress is equal to 1.8 MPa for a reference stress of 1 MPa.

### Concluding remarks

The effective notch stress method has been applied to the three specimen. Table 6.10 displays the effective notch stress concentration factor  $K_e = S_e/S_n$  and theoretical stress concentration factor  $K_t = \sigma_e/\sigma_s$  values. The theoretical stress concentration factor shows how the effective notch stress compares with the structural stress. For the T-shaped stiffener and the scallop, the values are greater than 1. This agrees with the FAT classes for the effective notch stress (Hobbacher, 2016). However, for the bilge corner, the value is smaller than 1. This indicates that when incorporating local weld information the stress is calculated to be lower than with the HSSSC. The values for  $K_e$  are also given and will be used in the comparison with the SSSdatabase.

**Table 6.10:** The  $K_e$  and  $K_t$  factors for all three specimens

Specimen	$K_e$	$K_t$
Bilge corner	5.3	0.8
T-shaped stiffener	2.1	1.3
Scallop	1.8	1.3

### 6.3.3. Database comparison

The results from the ENSC for the LSS have been plotted in figure 6.27. It can be seen that the data points resulting from the bilge corner still lie above the scatter band, however, not as far as with the the HSSSC. For the other data points, the gross of the T-shaped stiffener data points shifted toward the middle of the scatter band, while the rightmost data point moved toward the bottom of the scatter band. The same can be seen for the results of the scallop. The data points all moved towards the bottom of the scatter band.

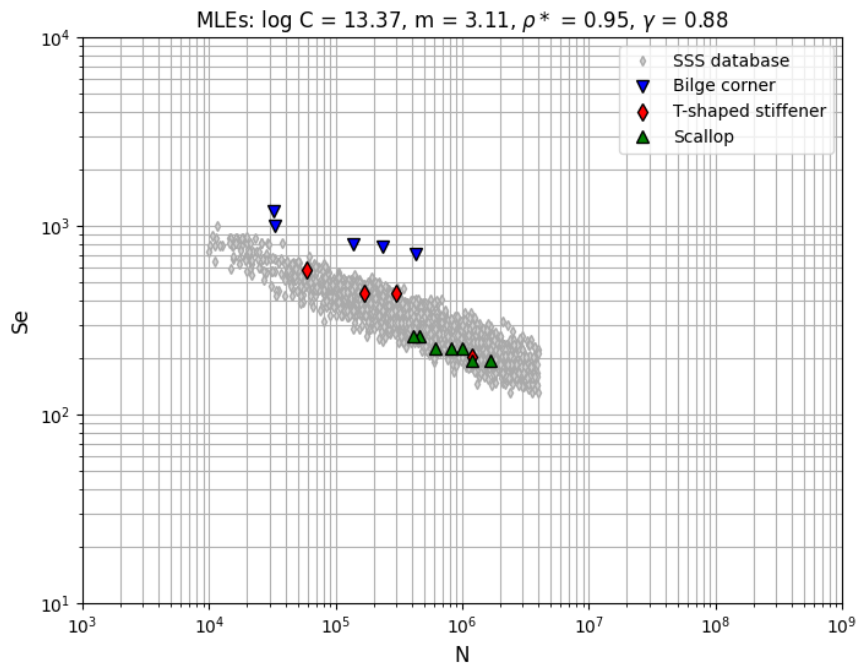


**Figure 6.27:** SSS and LSS comparison effective notch stress

Figure 6.28 shows the same effective notch stress data points, but this time the scatter parameters are added. Table 6.11 shows the scatter parameters without the bilge corner data points. These data points are omitted for a better comparison.

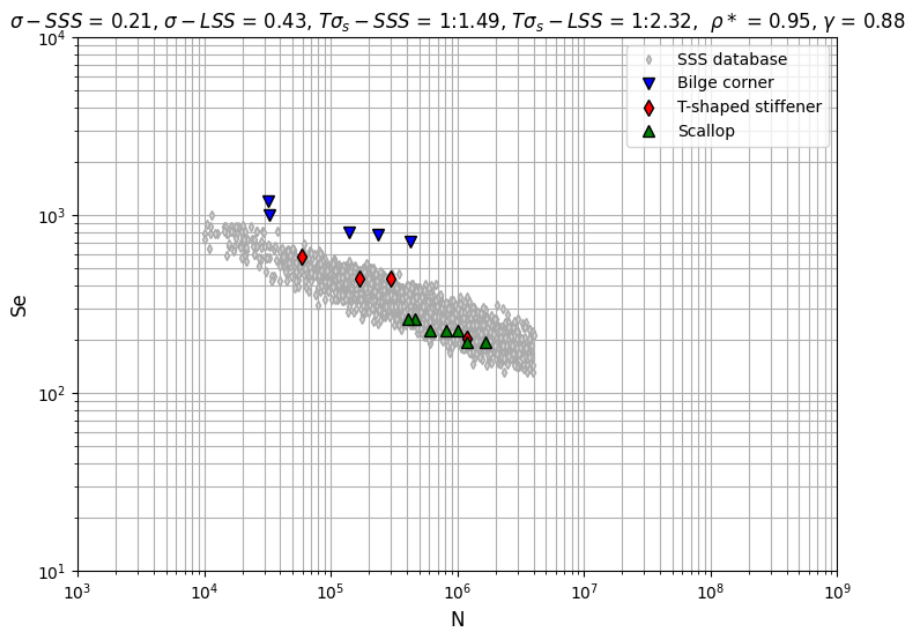


**Figure 6.28:** SSS and LSS comparison effective notch stress with scatter parameters

**Table 6.11:** Scatter parameters large-scale specimens for the ENSC

	$\sigma - LSS$	$T\sigma_s - LSS$
ENSC	0.15	1:1.36

### 6.4. Scale effects

This section will make a comparison of the vertical shift of the LSS data points in comparison with the SSS database using the different concepts. Figures 6.29 to 6.31 display the position of the LSS fatigue data points relative to the SSS database for respectively the NSC, HSSSC, and the ENSC.

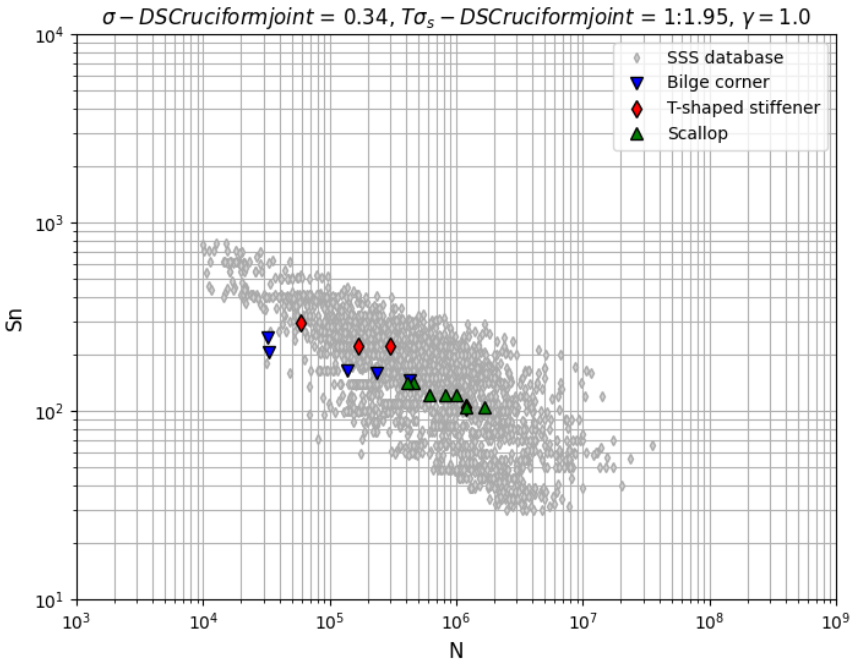


**Figure 6.29:** SSS and LSS comparison nominal stress

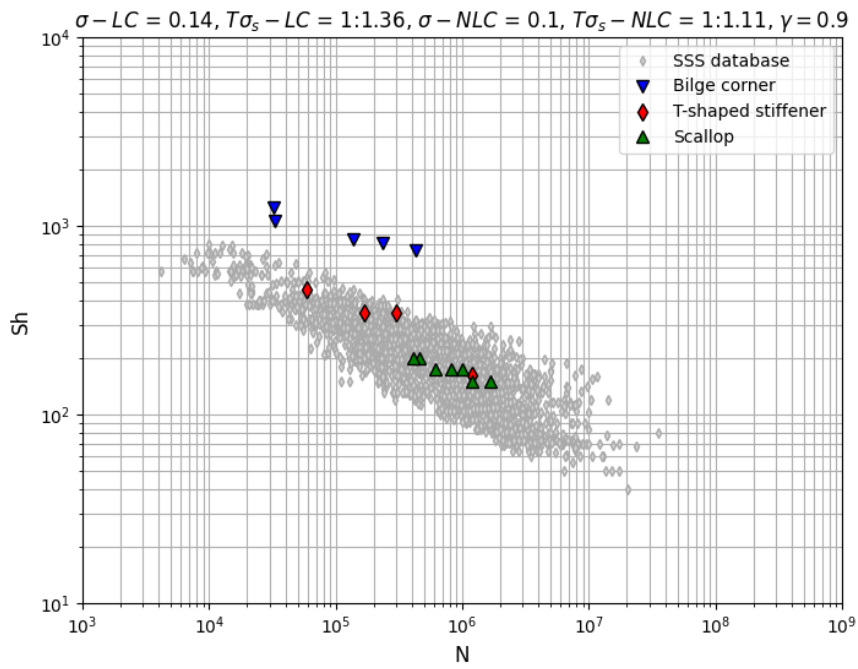


Figure 6.30: SSS and LSS comparison hot spot structural stress

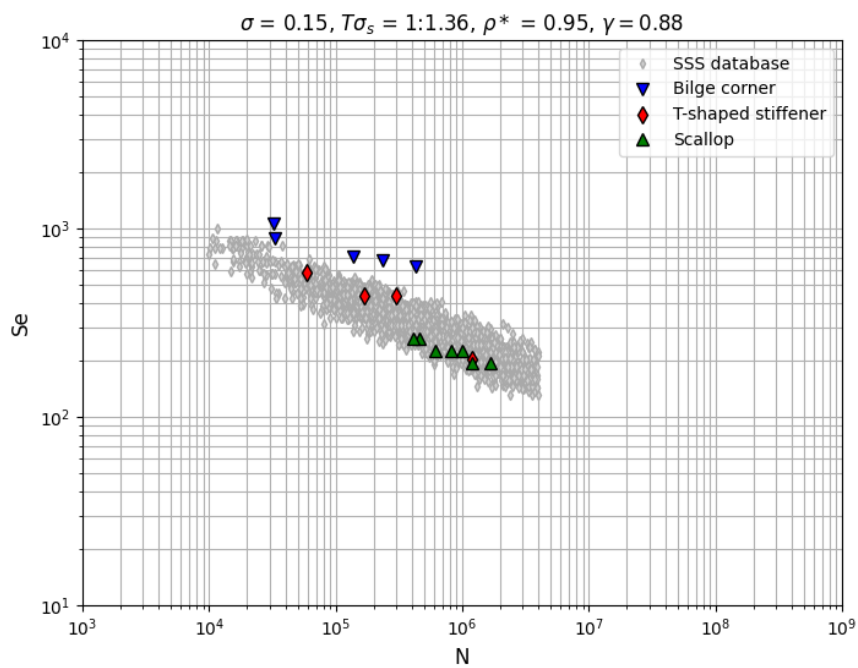


Figure 6.31: SSS and LSS comparison effective notch stress

First, figures 6.29 and 6.30 will be compared. It can be seen that three data points from the T-shaped stiffener shift from the lower/middle area of the scatter band in the NSC, to the upper area of the scatter band in the HSSSC. A look at figure 6.9 shows that the T-shaped stiffener data points are also in the

lower/middle area of the scatter band when compared only with DS cruciform joints. This shows that when switching from fatigue assessment with the NSC to assessment with the HSSSC, the stress calculation for the T-shaped stiffener results in a higher stress range relative to the SSS database. The data points for the scallop using the NSC are in the middle of the scatter band. When adopting the HSSSC, this remains the same as they are still in the middle of the HSSSC scatter band. This implies that there is no change in the magnitude of the stress range relative to the SSS database.

For the second comparison, the results using the HSSSC, figure 6.30, will be compared to the results from the ENSC, shown in figure 6.31. The three data points from the T-shaped stiffener that are at the top of the HSSSC scatter band, experience a small downwards shift relative to the SSS database when calculating the stress with the ENSC. This indicates that transitioning from fatigue evaluation using the NSC to assessment with the HSSSC leads to a lower stress range for the T-shaped stiffener relative to the SSS database. Contrary to the comparison between the NSC and the HSSSC for the scallop, the data points now do experience a shift relative to the SSS database. This also indicates that transitioning from fatigue evaluation using the NSC to assessment with the HSSSC leads to a lower stress range for the scallop relative to the SSS database.

### 6.4.1. Mean stress correction

For the mean stress correction, a comparison will be made between the HSSSC SSS scatter band with the LSS data points to see its effect. The HSSSC is chosen, because this was the only concept where the scatter band was also available where a mean stress correction was not applied. Figures 6.32 and 6.33 show respectively the scatter band with and without mean stress correction. It can be seen that the  $T_{\sigma_s}$  changes ever so slightly. The corrected figure shows the lowest  $T_{\sigma_s}$ .

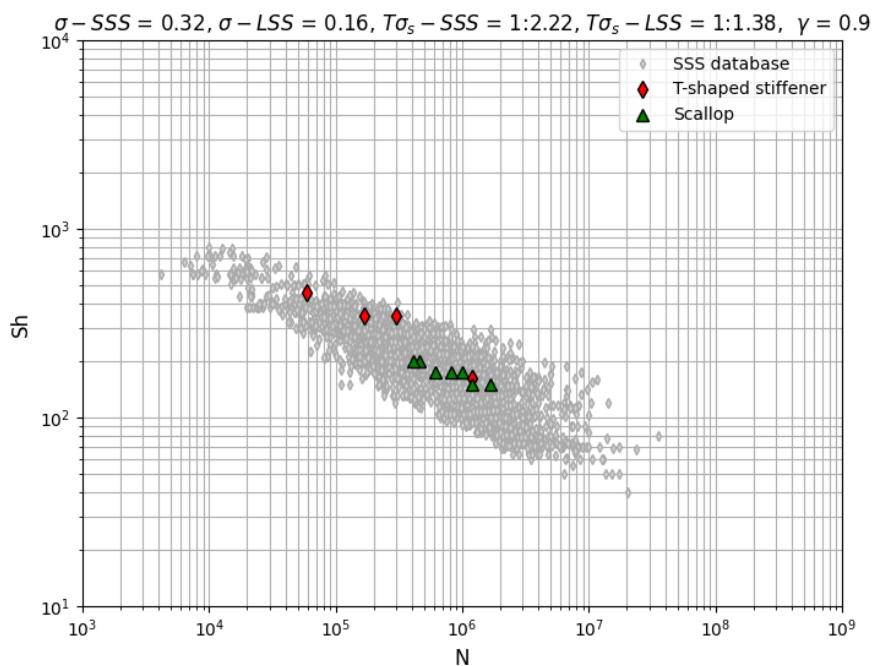
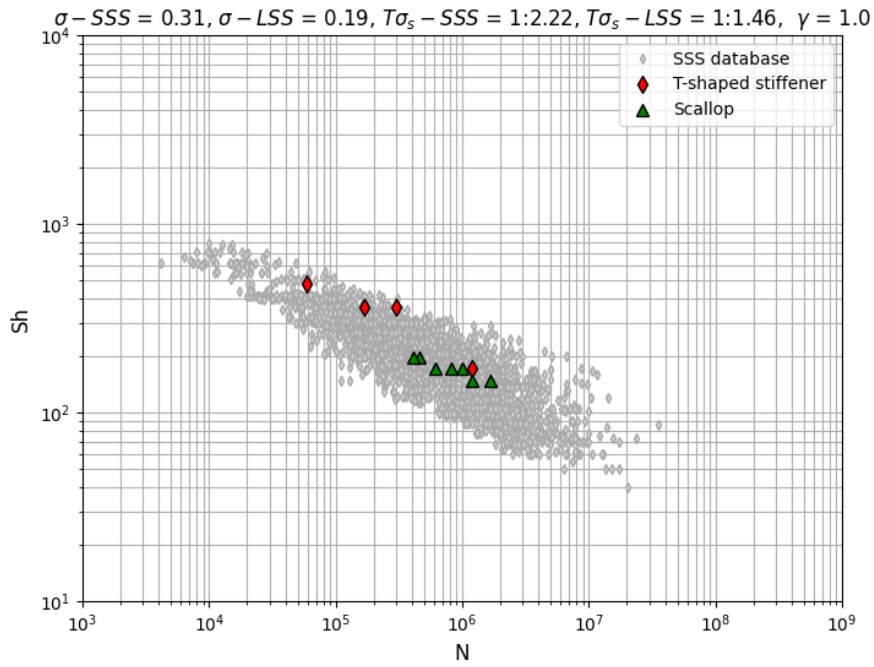
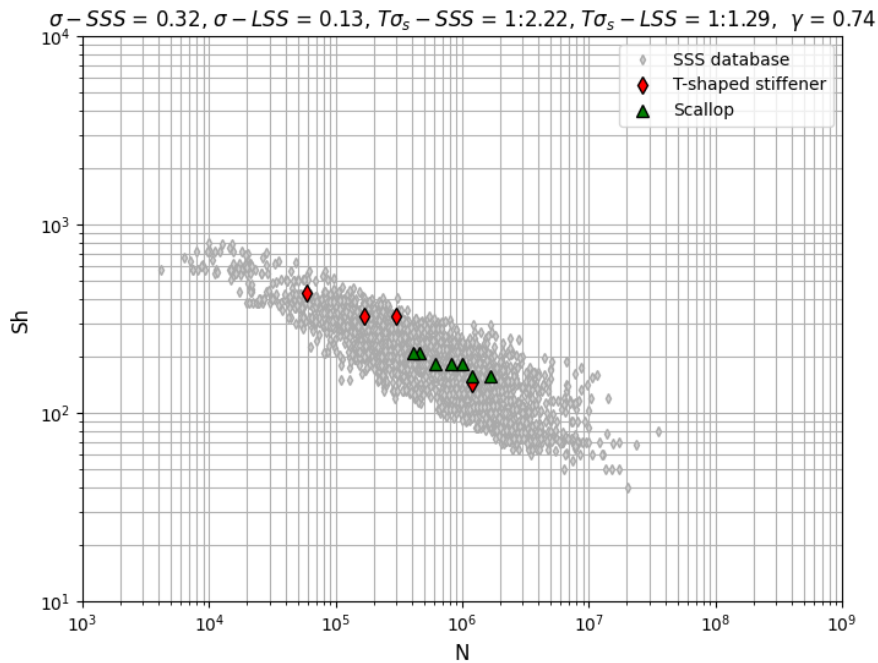


Figure 6.32: SSS and LSS comparison with the mean stress correction



**Figure 6.33:** SSS and LSS comparison without the mean stress correction

Figure 6.34 shows the scatter band with a  $\gamma = 0.74$ , this value is fitted to result in the smallest  $\sigma$  and  $T\sigma_s$  for the LSS. These values are 0.13 and 1:1.29. Drawing conclusions with a comparison to the scatter band is not possible, as the gamma for the scatter band is still equal to 0.90.



**Figure 6.34:** SSS and LSS comparison with a different mean stress correction

# Part III

## Judgement & future work

# Evaluation

## 7.1. Conclusions

This section will test the hypotheses mentioned in section 4.2.

***I) Large-scale fatigue data fits in the small-scale data scatter band when incorporating local (weld) geometry information.***

To test this hypothesis, the findings from sections 6.1 to 6.3 will be consulted. By comparing the placement of the LSS fatigue data points on the SSS fatigue data scatter band for the different fatigue assessment concept, different observations can be made. For the NSC, when comparing individual joint types, it can not be said that there is a fit between the SSS and LSS data points. For some joints, there is somewhat of an overlap, but saying it fits the scatter band would be far-fetched.

The findings from the bilge corner by Kozak (1999) will **not** be taken into consideration for the following explanations due to significant uncertainty, which prevents drawing meaningful conclusions.

When looking at the HSSSC in section 6.2, the SSS data scatter band has become narrower and more compact due to the reduction in scatter compared to the NSC scatter band. Even with this smaller scatter band, the hot spot structural stress LSS fatigue data points overlap well with the SSS data scatter band. So it can be said that the results from the T-shaped stiffener and the scallop fit the SSS scatter band when using the HSSSC.

Examining the ENSC results from in section 6.3, provides similar results. The effective notch stress SSS data scatter band has become even narrower and more compact due to more reduction in scatter compared to the HSSSC scatter band. The effective notch stress LSS data points do once again fit into the scatter band.

Considering these explanations the hypothesis can be accepted: large-scale fatigue data does fit in the small-scale data scatter band when incorporating local (weld) geometry information.

***II) Large-scale fatigue data captured with the ENSC will prove to have a better fit in the small-scale data scatter band than fatigue data captured with the HSSSC. The reason for the better fit is less structural redundancy effect and the removal of the notch effect.***

This hypothesis will be tested with the results from sections 6.3 and 6.4. It is adopted that a better fit means a reduction in the performance indicators, i.e. the standard deviation and the strength scatter band index. Tables 7.1 and 7.2 are shown to display the scatter parameters for the distinguishable curves. These indicate that the scatter parameters are not so different from each other.

**Table 7.1:** Scatter parameters large-scale specimens for the HSSSC

HSSSC	$\sigma - LSS$	$T\sigma_s - LSS$
LC	0.14	1:1.36
NLC	0.1	1:1.11

**Table 7.2:** Scatter parameters large-scale specimens for the ENSC

	$\sigma - LSS$	$T\sigma_s - LSS$
ENSC	0.15	1:1.36

A comparison between the HSSSC and the ENSC is made in section 6.4. Beforehand it was expected that the application of the ENSC would show a vertical shift upwards for the LSS data points. This would happen as a result of the removal of the notch effect mentioned in Subsection 3.4.2. It is expected that the large-scale specimens show a reduction in fatigue strength because of the notch effect, so the incorporation of this scale effect within the ENSC would remove the reduction in fatigue strength, and thus show a vertical shift upwards. This is not what is observed for the inspected specimens. The HSSSC and ENSC are both local assessment concepts, therefore it is not expected that the structural redundancy scale effect has influence on the observed vertical shift downwards.

These explanations considered, the hypothesis can be rejected. The ENSC does not necessarily show a better fit, and it can not be concluded that a decrease in structural redundancy and the removal of the notch effect play a part.

***III) Applying a mean stress correction will provide for a better fit of the large-scale specimen data in the small-scale data scatter band.***

The hypothesis expects that applying a mean stress correction will lead to a better alignment of large-scale specimen data within the scatter band derived from small-scale data. However, the findings from the comparison between scatter bands with and without mean stress correction suggest otherwise. In the analysis, it was observed that the mean stress correction had a small effect on the scatter band, as evidenced by the changes in the  $T\sigma_s$ . Moreover, when a different gamma value, 0.74, was employed to minimize the standard deviation and achieve the best fit for the large-scale specimen data, but no meaningful conclusions could be drawn due to the mismatch in gamma values between the scatter band and the large-scale data. Therefore, this hypothesis can neither be accepted nor rejected. Further investigation and refinement of the mean stress correction methodology may be warranted to better understand its potential effects on aligning data from different scales within a common scatter band. The method should also be applied to all the different fatigue assessment concepts.

The research goal of this thesis is the following:

***The goal of this research is to improve the understanding of fatigue resistance similarity between steel small-scale test specimens and large-scale structures used for structure design. Specifically listing and quantifying the scaling phenomena that arise when transferring fatigue data from small-scale specimen tests to large-scale results used for structure design. Proving fatigue resistance similarity and mapping these scale effects and their influence on the fatigue strength of a full-scale structure can reduce design conservatism***

The research was to be called successful if the scaling phenomena that arise when transferring fatigue data from small- to -large-scale were found and quantified. This could be achieved by assessing large-scale specimen with different fatigue assessment concepts, incorporating various scale effects. To a certain extent, this has been accomplished. For the two large-scale test specimens that were used in the conclusions, fatigue resistance similarity could be shown using the effective notch stress concept. The

strength scatter band index in the results dropped from 1:1.62, to 1:1.45, to 1:1.36 adopting respectively the nominal stress concept, the hot spot structural stress concept and the effective notch stress concept. However, quantifying the scaling phenomena proved to be a challenging endeavor. Despite the analysis conducted, the results did not reveal any clear or unequivocal influence of the individual scale effects.

## 7.2. Discussion

The results and conclusions have been presented in respectively chapter 6 and section 7.1. This section will reflect on the results and conclusion.

A main issue with the results are the results from the bilge corner. Because of the high uncertainty in the failure criterion for this specimen it is high impossible to draw meaningful conclusions surrounding this specimen. As mentioned in Subsection 5.2.1 there is data on the number of cycles for a crack that is 80-90% of the flange width for this specimen. The results for the HSSSC and ENSC have been plotted in respectively figures 7.1 and 7.6. The figures show a horizontal shift of the data points compared to the results in sections 6.2 and 6.3. This horizontal shift causes the data points to have a  $N$  that lies outside of the MCF range the SSS data scatter band covers. So it can hardly be said that this data now fits the SSS data scatter band. However, a visual extrapolation of the SSS data scatter band show that this failure criterion shows more promising results than the  $N$  mentioned in the article by Kozak (1999).

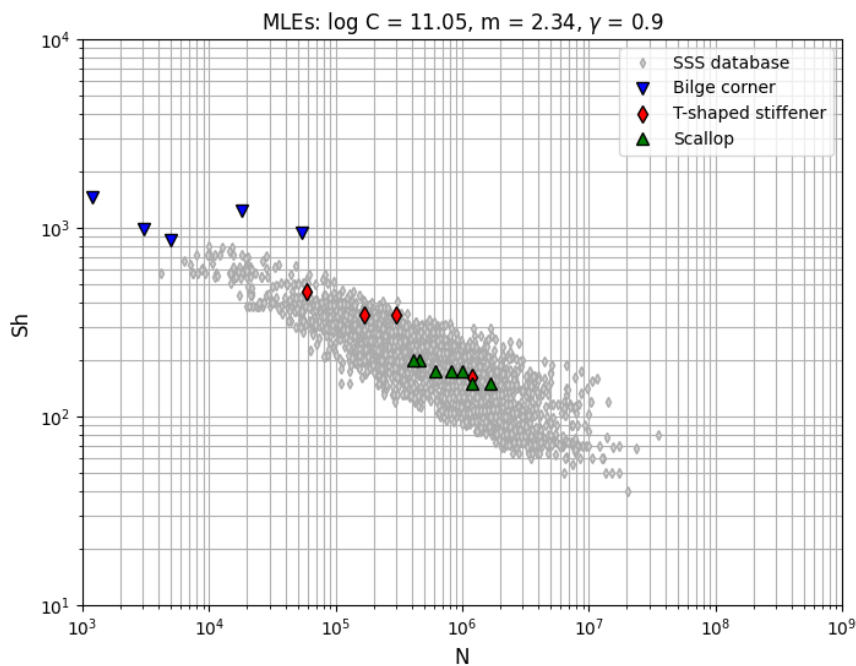


**Figure 7.1:** SSS and LSS comparison hot spot structural stress with a different failure criterion for the bilge corner

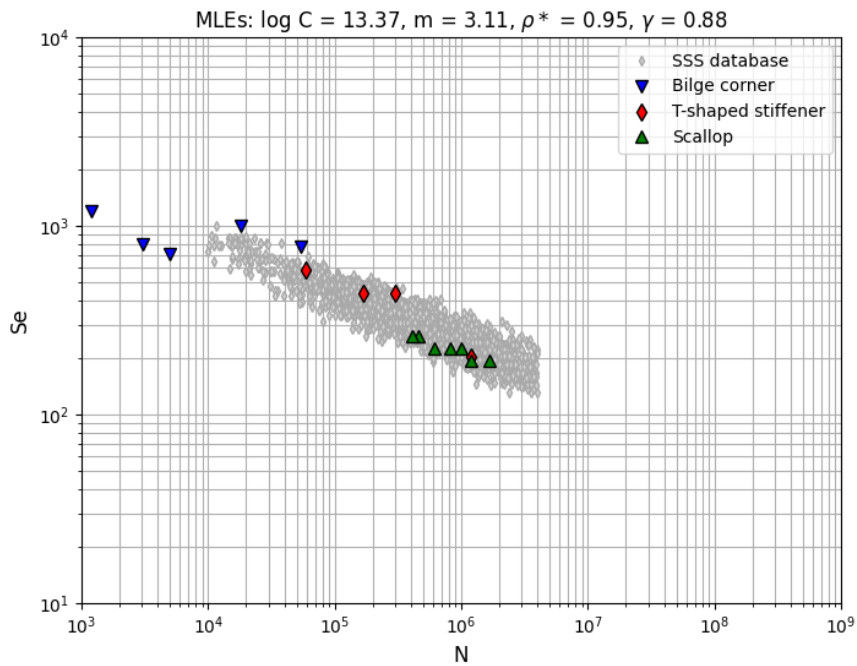


**Figure 7.2:** SSS and LSS comparison effective notch stress with a different failure criterion for the bilge corner

Another issue with the bilge corner is the hard point that is found at the hot spot. Thus it can also be interpreted as a hot spot type A. Considering this, also calculations using the virtual node method were completed. Figure 7.3 shows a comparison for the hot spot type A and C method. The virtual node method shows consistent results for the different mesh sizes, with an SCF of around 5.5, which is lower than the 6.4 found using the HSSSC earlier. For the ENSC the SCF reduces from 5.3 to 4.7. The results can be found in figures 7.4 and 7.5.

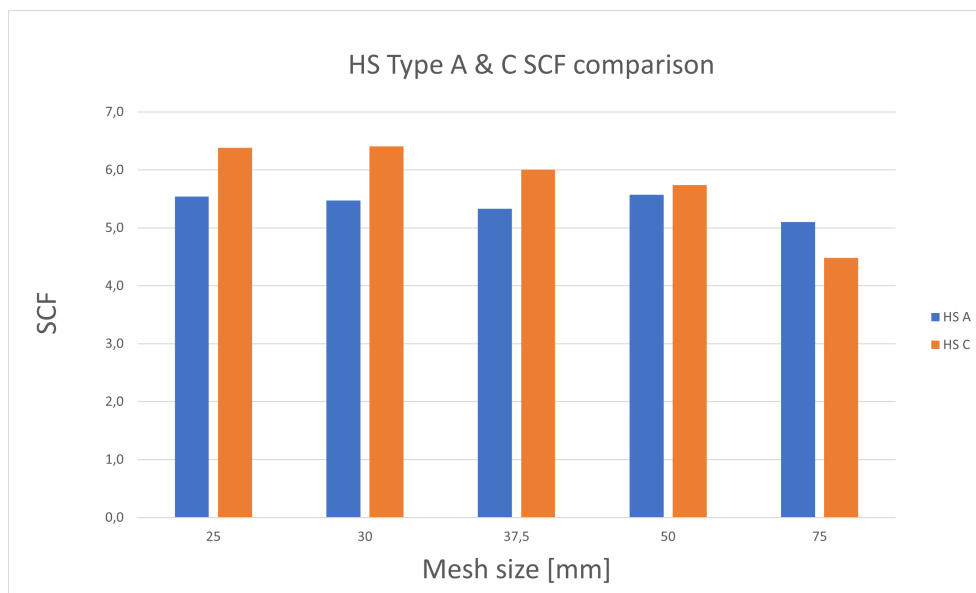


**Figure 7.3:** HS type A and C comparison for the bilge corner

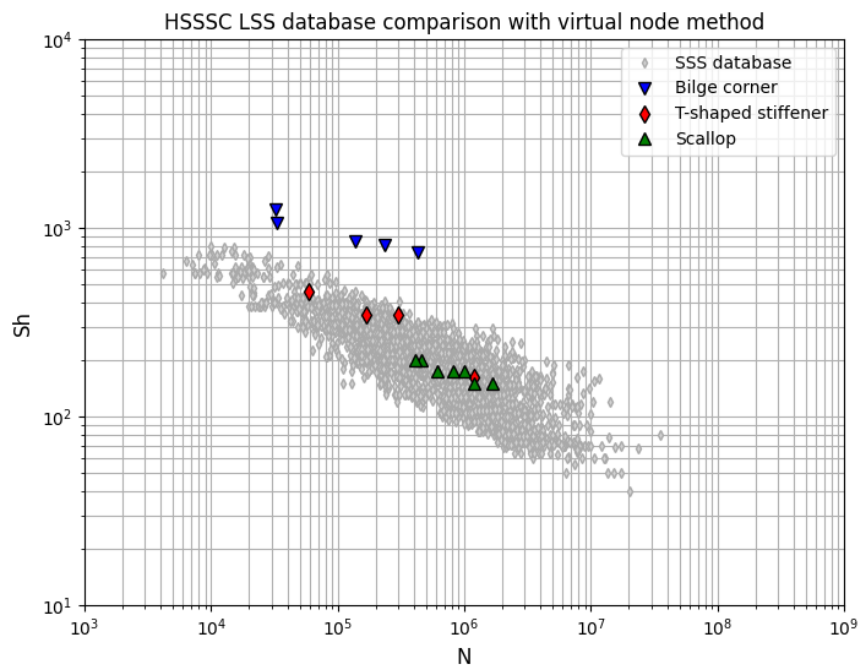


**Figure 7.4:** HSSSC comparison using the virtual node method

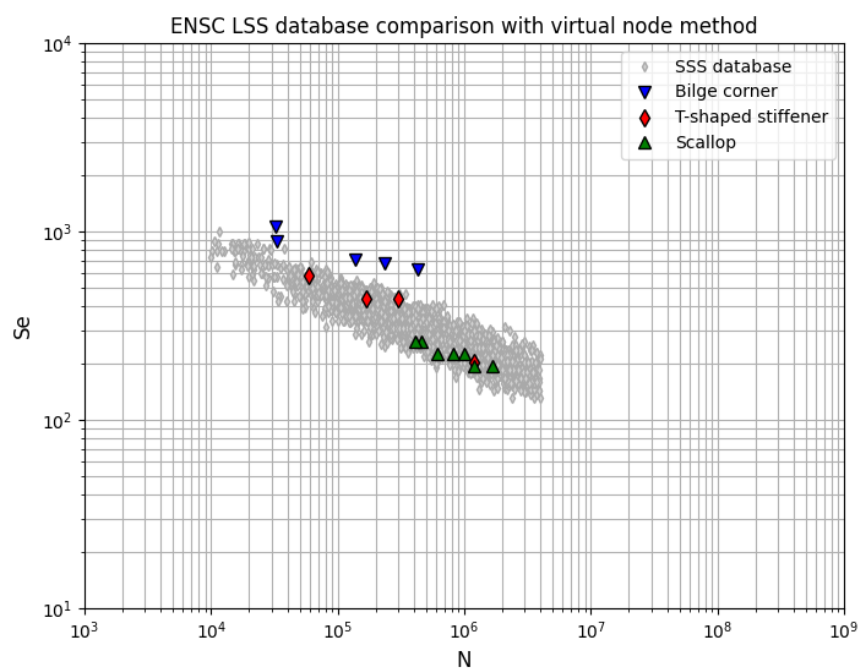


**Figure 7.5:** ENSC comparison using the virtual node method

Another difficulty arose when analyzing the results from the HSSSC and the ENSC. It was expected that due to the removal of the notch effect, the data points would show a relative shift upwards compared to the SSS database. However, the opposite occurred. No explanation has yet been found for the unexpected

outcome. It is possible that the base plate thickness size effects plays a role. Comparing figures 11B and 12B from Qin et al. (2019) shows that the thicker plates ( $20 < t_p$ ) are more towards the bottom of the scatter band. The plate thicknesses in question are only 13 and 9 mm. So it would make sense that for the HSSSC the LSS data points are more positioned towards the upper end of the scatter band. When looking at figure 12B from Qin et al. (2019) the plate thicknesses play little to no role, when the ENSC is applied as all thicknesses appear randomly throughout the scatter band. This could also be the explanation for the behaviour that is displayed in the comparison in this thesis.

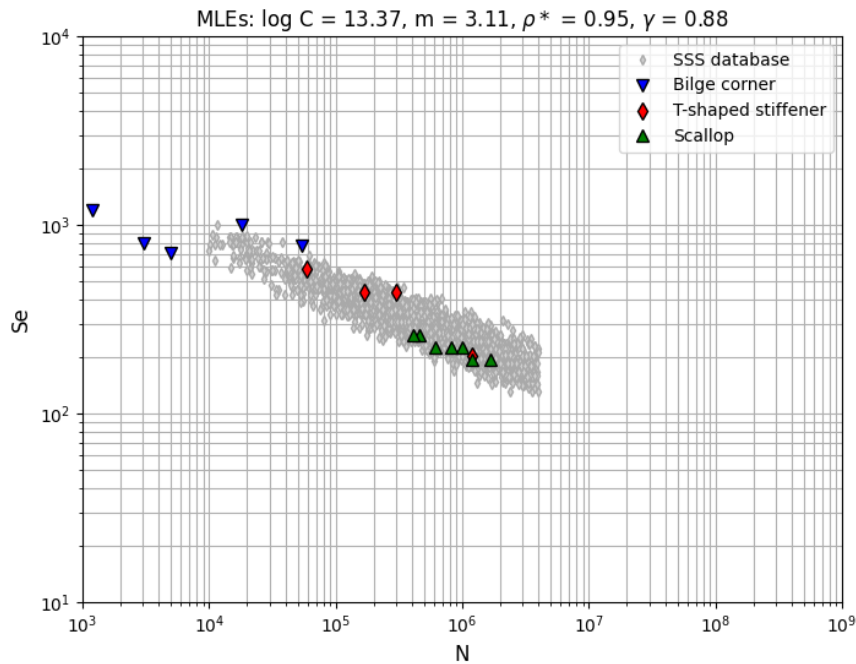


**Figure 7.6:** SSS and LSS comparison effective notch stress with a different failure criterion for the bilge corner

A scale effect that was not explicitly researched is the statistical scale effect. The statistical scale effect could have had an influence. However, no significant effect stemming from this scale effect was observed in the analysis. One possible explanation for this absence of effect is the relatively smaller database available for large-scale specimens compared to their smaller counterparts. It is plausible that the statistical scale effect, which would be more pronounced with a larger and more comprehensive dataset for large-scale specimens, was mitigated to some extent due to the limited amount of data available. This observation highlights the importance of considering the size and representativeness of the dataset when analyzing scale effects in fatigue testing, as well as the potential need for further research with larger sample sizes to fully understand the impact of the scale effects on fatigue behavior.

### 7.3. Recommendations

Following the finding of this thesis regarding a fit of two of the large-scale specimen using the ENSC, the first recommendation is to increase the size of the large-scale specimen database. With an increased sample size, more results could be compared, which makes conclusions less susceptible to outliers. Another benefit would be that the influence of the scale effects could become more apparent. The current results could not fully depict and quantify the influence of the scale effects.

Another recommendation would be to subject the large-scale specimens to the TSC. Considering the TSC combines the crack initiation and crack propagation stage, which could lead to new insights in the scaling phenomena as the crack growth behaviour is not as evident in large-scale specimens.

---

The third recommendation is to apply the mean stress correction to more than just one database. The application to just one database is not very extensive. Also, if possible, an option is to try different mean stress correction models on the small- and large-scale specimen databases. This could lead to different results and insights with respect to the residual stresses scale effect.

# References

- Alang, N. A., Razak, N. A., & Miskam, A. (2011). Effect of surface roughness on fatigue life of notched carbon steel. <https://api.semanticscholar.org/CorpusID:15392333>
- Alava, M., Nukala, P., & Zapperi, S. (2009). Size effects in statistical fracture. *Journal of Physics D: Applied Physics*, 42. <https://doi.org/10.1088/0022-3727/42/21/214012>
- Arzola, N., & Hernández, E. (2017). Experimental characterization of fatigue strength in butt welded joint considering the geometry and the effect of cooling rate of the weld. *Journal of Physics: Conference Series*, 843, 012047. <https://doi.org/10.1088/1742-6596/843/1/012047>
- Barsoum, Z., Khurshid, M., & Barsoum, I. (2012). Fatigue strength evaluation of friction stir welded aluminium joints using the nominal and notch stress concepts. *Materials Design*, 41, 231–238. <https://doi.org/https://doi.org/10.1016/j.matdes.2012.05.018>
- Beretta, S., Clerici, P., & Matteazzi, S. (1995). The effect of sample size on the confidence of endurance fatigue tests. *Fatigue & Fracture of Engineering Materials & Structures*, 18(1), 129–139. <https://doi.org/https://doi.org/10.1111/j.1460-2695.1995.tb00147.x>
- Blacha, Ł., Karolczuk, A., Bański, R., & Stasiuk, P. (2013). Application of the weakest link analysis to the area of fatigue design of steel welded joints [Special issue on ICEFA V- Part 1]. *Engineering Failure Analysis*, 35, 665–677. <https://doi.org/https://doi.org/10.1016/j.engfailanal.2013.06.012>
- Blagojević, B., & Žiha, K. (2008). On the assessment of redundancy of ship structural components.
- C. Fischer, W. F., & Rizzo, C. M. (2018). Fatigue assessment of web-stiffened corners in plated structures by local approaches. *Ship Technology Research*, 65(2), 69–78. <https://doi.org/10.1080/09377255.2018.1441781>
- den Besten, H. (2015). Fatigue resistance of welded joints in aluminium high-speed craft: A total stress concept. *PhD Thesis; Delft University of Technology*. <https://doi.org/10.4233/uuid:370b3d44-f4a6-403e-9629-d36174c3aca4>
- den Besten, H. (2018). Fatigue damage criteria classification, modelling developments and trends for welded joints in marine structures. *Ships and Offshore Structures*, 13(8), 787–808. <https://doi.org/10.1080/17445302.2018.1463609>
- den Besten, H. (2021a). *OE44085-03-FatigueFundamentalsInStructures* (tech. rep.). TU Delft.
- den Besten, H. (2021b). *OE44085-07-HotSpotStructuralStressConcept* (tech. rep.). TU Delft.
- Deul, M., Lieshout, P., & Werter, N. (2022). On the validity of using small-scale fatigue data to design full-scale steel welded structures: Testing assumptions on residual stress relief. *PRADS, Technical Sessions- Structures, Structural Analysis I*.
- DNV. (2021a). *CG-0129: Fatigue assessment of ship structures* (tech. rep.). DNV.
- DNV. (2021b). *RP-C203: Fatigue design of offshore steel structures* (tech. rep.). DNV.
- Dong, P. (2001). A structural stress definition and numerical implementation for fatigue analysis of welded joints. *International Journal of Fatigue*, 23(10), 865–876. [https://doi.org/https://doi.org/10.1016/S0142-1123\(01\)00055-X](https://doi.org/https://doi.org/10.1016/S0142-1123(01)00055-X)
- Dong, P. (2003). A robust structural stress method for fatigue analysis of ship structures. *Proceedings of the International Conference on Offshore Mechanics and Arctic Engineering - OMAE*, 3. <https://doi.org/10.1115/OMAE2003-37313>
- Dowling, N. E. (2007). *Mechanical behaviour of materials (3rd edition)*.

- Fang, Z., & Fan, H. (2011). Redundancy of structural systems in the context of structural safety [The Proceedings of the Twelfth East Asia-Pacific Conference on Structural Engineering and Construction]. *Procedia Engineering*, 14, 2172–2178. <https://doi.org/https://doi.org/10.1016/j.proeng.2011.07.273>
- Fatemi, A., & Yang, L. (1998). Cumulative fatigue damage and life prediction theories: A survey of the state of the art for homogeneous materials. *International Journal of Fatigue*, 20(1), 9–34. [https://doi.org/https://doi.org/10.1016/S0142-1123\(97\)00081-9](https://doi.org/https://doi.org/10.1016/S0142-1123(97)00081-9)
- Feng, X., Zheng, K., Heng, J., Zhu, J., & He, X. (2022). Fatigue performance of rib-to-deck joints in orthotropic steel deck with pwht. *Journal of Constructional Steel Research*, 196. <https://doi.org/https://doi.org/10.1016/j.jcsr.2022.107420>
- Fricke, W., & Paetzold, H. (2010). Full-scale fatigue tests of ship structures to validate the s–n approaches for fatigue strength assessment. *Marine Structures*, 23(1), 115–130. <https://doi.org/https://doi.org/10.1016/j.marstruc.2010.01.004>
- Garbatov, Y., Ås, S., Branner, K., Choi, B., den Besten, J., Dong, P., Lillemäe, I., Lindstrom, P., de Souza, M. L., Parmentier, G., Quéméner, Y., Rizzo, C., Rörup, J., Vhanmane, S., Villavicencio, R., Wang, F., & Yue, J. (2018). Proceedings of the 20th international ship and offshore structures congress. *Progress in Marine Science and Technology*, 4(1), 85–108. <https://ebooks.iospress.nl/volumearticle/53809>
- Heckel, K., Köhler, J., & München, T. (1975). Experimentelle untersuchung des statistischen größeneinflusses im dauerschwingversuch an ungekerbten stahlproben. *Materialwissenschaft und Werkstofftechnik*, 6(2), 52–54. <https://doi.org/https://doi.org/10.1002/mawe.19750060204>
- Hendawi, S., & Frangopol, D. M. (1994). System reliability and redundancy in structural design and evaluation [Reliability-based Structural System Assessment, Design and Optimization]. *Structural Safety*, 16(1), 47–71. [https://doi.org/https://doi.org/10.1016/0167-4730\(94\)00027-N](https://doi.org/https://doi.org/10.1016/0167-4730(94)00027-N)
- Herzberg, R. W. (1995). *Deformation and fracture mechanics of engineering materials (4th edition)*. John Wiley & Sons.
- Hobbacher, A. F. (2016). *Recommendations for fatigue design of welded joints and components*. <https://doi.org/10.1007/978-3-319-23757-2>
- Ibrahim, R. A. (2015). Overview of Structural Life Assessment and Reliability, Part II: Fatigue Life and Reliability Assessment of Naval Ship Structures. *Journal of Ship Production and Design*, 31(02), 100–128. <https://doi.org/10.5957/jspdp.2015.31.2.100>
- Inoma, J. E., Pavlou, D. G., & Zec, J. (2019). Implementation of linear, double-linear, and nonlinear fatigue damage accumulation rules for fatigue life prediction of offshore drilling top-drive tie-rods. *IOP Conference Series: Materials Science and Engineering*, 700(1), 012025. <https://doi.org/10.1088/1757-899X/700/1/012025>
- Klevtsov, G., & Klevtsova, N. (2008). Influence of stress ratio  $r$  on the fatigue strength and fatigue crack path in metal materials, 359–365. [https://www.researchgate.net/publication/267363680\\_Influence\\_of\\_Stress\\_Ratio\\_R\\_on\\_the\\_Fatigue\\_Strength\\_and\\_Fatigue\\_Crack\\_Path\\_in\\_Metal\\_Materials](https://www.researchgate.net/publication/267363680_Influence_of_Stress_Ratio_R_on_the_Fatigue_Strength_and_Fatigue_Crack_Path_in_Metal_Materials)
- Kozak, J. (1999). Fatigue problems in ship structure. *Transactions on the Built Environment*, 42, 541–550.
- Kozak, J., & Górski, Z. (2015). Fatigue damage model for welded joints of perpendicular plates. *Welding International*, 29(11), 856–860. <https://doi.org/10.1080/09507116.2014.937598>
- Lassen, T., Darcis, P., & Recho, N. (2005). Fatigue behavior of welded joints part 1 - statistical methods for fatigue life prediction. *Welding Journal (Miami, Fla)*, 84, 183–s.
- Leonetti, D., Maljaars, J., & Snijder, H. (2020). Probabilistic fatigue resistance model for steel welded details under variable amplitude loading : Inference and uncertainty estimation. *International Journal of Fatigue*, 135. <https://doi.org/10.1016/j.ijfatigue.2020.105515>
- Li, D., Zhang, C., & Lu, P. (2020). Fatigue property and improvement of a rounded welding region between the diaphragm plate and closed rib of an orthotropic steel bridge deck. *Metals*, 10(2). <https://doi.org/10.3390/met10020161>

- Liao, D., Zhu, S.-P., Keshtegar, B., Qian, G., & Wang, Q. (2020). Probabilistic framework for fatigue life assessment of notched components under size effects. *International Journal of Mechanical Sciences*, *181*, 105685. <https://doi.org/https://doi.org/10.1016/j.ijmecsci.2020.105685>
- Liu, S., & Liu, Y. (2019). Summary of research on fatigue life assessment of welded joints. *Journal of Physics: Conference Series*, *1303*(1), 012002. <https://doi.org/10.1088/1742-6596/1303/1/012002>
- Loporcaro, G., Pampanin, S., & Kral, M. (2015). Experimental validation of "the hardness method" to estimate the residual ductility of plastically deformed steel reinforcement.
- Lotsberg, I. (2016). *Fatigue design of marine structures*. Cambridge University Press. <https://doi.org/10.1017/CBO9781316343982>
- Lotsberg, I., & Landet, E. (2005). Fatigue capacity of side longitudinals in floating structures. *Marine Structures*, *18*(1), 25–42. <https://doi.org/https://doi.org/10.1016/j.marstruc.2005.08.002>
- Maddox, S., & Zhang, Y. (2008). Comparison of fatigue of girth-welds in full-scale pipes and small-scale strip specimens. <https://doi.org/10.1115/OMAE2008-57103>
- Magoga, T., Aksu, S., Cannon, S., Ojeda, R., & Thomas, G. (2019). Through-life hybrid fatigue assessment of naval ships. *Ships and Offshore Structures*, *14*(7), 664–674. <https://doi.org/10.1080/17445302.2018.1550900>
- Makkonen, M. (2001). Statistical size effect in the fatigue limit of steel. *International Journal of Fatigue*, *23*(5), 395–402. [https://doi.org/https://doi.org/10.1016/S0142-1123\(01\)00003-2](https://doi.org/https://doi.org/10.1016/S0142-1123(01)00003-2)
- Makkonen, M. (2003). Notch size effects in the fatigue limit of steel. *International Journal of Fatigue*, *25*(1), 17–26. [https://doi.org/https://doi.org/10.1016/S0142-1123\(02\)00053-1](https://doi.org/https://doi.org/10.1016/S0142-1123(02)00053-1)
- Miki, C., & Tateishi, K. (1997). Fatigue strength of cope hole details in steel bridges. *International Journal of Fatigue*, *19*(6), 445–455. [https://doi.org/https://doi.org/10.1016/S0142-1123\(97\)85727-1](https://doi.org/https://doi.org/10.1016/S0142-1123(97)85727-1)
- Miner, M. A. (1945). Cumulative Damage in Fatigue. *Journal of Applied Mechanics*, *12*(3), A159–A164. <https://doi.org/10.1115/1.4009458>
- Nagy, W., Wang, B., Culek, B., Bogaert, P., & De Backer, H. (2017). Development of a fatigue experiment for the stiffener-to-deck plate connection in orthotropic steel decks. *International Journal of Steel Structures*, *17*, 1353–1364. <https://doi.org/10.1007/s13296-017-1207-8>
- NEN. (2012). *Eurocode 3: Ontwerp en berekening van staalconstructies - deel 1-9: Vermoeiing* (tech. rep.). NEN.
- Neuber, H. (1937). *Kerbspannungslehre*. Springer.
- Nikolaidis, E., & Kapania, R. K. (1990). System Reliability and Redundancy of Marine Structures: A Review of the State of the Art. *Journal of Ship Research*, *34*(01), 48–59. <https://doi.org/10.5957/jsr.1990.34.1.48>
- Ohta, A., Maeda, Y., Mawari, T., Nishijima, S., & Nakamura, H. (1986). Fatigue strength evaluation of welded joints containing high tensile residual stresses. *International Journal of Fatigue*, *8*(3), 147–150. [https://doi.org/https://doi.org/10.1016/0142-1123\(86\)90006-X](https://doi.org/https://doi.org/10.1016/0142-1123(86)90006-X)
- Ohta, A., Maeda, Y., & Suzuki, N. (1993). Effect of yield strength on the basic fatigue strength of welded joints. *Fatigue & Fracture of Engineering Materials & Structures*, *16*(5), 473–479. <https://doi.org/https://doi.org/10.1111/j.1460-2695.1993.tb00760.x>
- Ohta, A., Maeda, Y., & Suzuki, N. (2002). Residual stress effect on fatigue strength of non-load-carrying cruciform welded joints of sm570q steel for welded structures. *Welding in the World*, *46*, 20–25. <https://api.semanticscholar.org/CorpusID:135756162>
- Paik, J. K., & Kim, B. J. (2002). Ultimate strength formulations for stiffened panels under combined axial load, in-plane bending and lateral pressure: A benchmark study. *Thin-Walled Structures*, *40*(1), 45–83. [https://doi.org/https://doi.org/10.1016/S0263-8231\(01\)00043-X](https://doi.org/https://doi.org/10.1016/S0263-8231(01)00043-X)
- Palmgren, A. (1924). Die lebensdauer von kugellagern. *Zeitschrift des Vereines Deutscher Ingenieure (VDI Zeitschrift)*, *68*(14), 339–341.

- Papatheocharis, T., Sarvanis, G. C., Perdikaris, P. C., Karamanos, S. A., & Zervaki, A. D. (2020). Fatigue resistance of welded steel tubular x-joints. *Marine Structures*, 74, 102809. <https://doi.org/https://doi.org/10.1016/j.marstruc.2020.102809>
- Pedersen, M. (2019). Thickness effect in fatigue of welded butt joints: A review of experimental works. *International Journal of Steel Structures*, 19. <https://doi.org/10.1007/s13296-019-00254-y>
- Peterson, R. (1938). Methods of correlating data from fatigue tests of stress concentration specimens. In *Stephen timoshenko 60th anniversary volume* (p. 197). The Macmillan Company.
- Polezhayeva, H., Howarth, D., Maddox, S., & Robinson, A. (2013). Fatigue testing to identify effect of mean stress on fatigue strength of welded joints in ship structures.
- Pyttel, B., Schwerdt, D., & Berger, C. (2011). Very high cycle fatigue – is there a fatigue limit? [Advances in Very High Cycle Fatigue]. *International Journal of Fatigue*, 33(1), 49–58. <https://doi.org/https://doi.org/10.1016/j.ijfatigue.2010.05.009>
- Qin, Y., den Besten, H., Palkar, S., & Kaminski, M. L. (2021). Mid- and high-cycle fatigue of welded joints in steel marine structures: Effective notch stress and total stress concept evaluations. *International Journal of Fatigue*, 142, 105822. <https://doi.org/https://doi.org/10.1016/j.ijfatigue.2020.105822>
- Qin, Y., den Besten, H., Palkar, S. M., & Kaminski, M. L. (2019). Fatigue design of welded double-sided t-joints and double-sided cruciform joints in steel marine structures: A total stress concept. *Fatigue & Fracture of Engineering Materials & Structures*. <https://api.semanticscholar.org/CorpusID:203555123>
- Rizzo, C. M., & Tedeschi, R. A. (2007). Fatigue strength of a typical ship structural detail: Tests and calculation methods. *Fatigue & Fracture of Engineering Materials & Structures*, 30(7), 653–663. <https://doi.org/https://doi.org/10.1111/j.1460-2695.2007.01147.x>
- Rizzo, C. M., & Fricke, W. (2013). Fatigue assessment of bulb stiffener joints according to local approaches. *Ships and Offshore Structures*, 8(1), 73–83. <https://doi.org/10.1080/17445302.2011.647805>
- Saini, D. S., Karmakar, D., & ray chaudhuri, S. (2016). A review of stress concentration factors in tubular and non-tubular joints for design of offshore installations. *Journal of Ocean Engineering and Science*, 1. <https://doi.org/10.1016/j.joes.2016.06.006>
- Schijve, J. (2009). *Fatigue of structures and materials*. Springer.
- Schijve, J. (2012). Fatigue predictions of welded joints and the effective notch stress concept. *International Journal of Fatigue*, 45, 31–38. <https://doi.org/https://doi.org/10.1016/j.ijfatigue.2012.06.016>
- Siemens. (2021). Ship structures design. *Siemens Digital Industries Commercial Shipbuilding Software*.
- Sonsino, C. M., & Fischer, G. (2005). Local assessment concepts for the structural durability of complex loaded components. *Materialwissenschaft und Werkstofftechnik*, 36(11), 632–641. <https://doi.org/https://doi.org/10.1002/mawe.200500932>
- Sonsino, C. (2009). Effect of residual stresses on the fatigue behaviour of welded joints depending on loading conditions and weld geometry [Fatigue assessment of welded connections]. *International Journal of Fatigue*, 31(1), 88–101. <https://doi.org/https://doi.org/10.1016/j.ijfatigue.2008.02.015>
- Sonsino, C., Fricke, W., de Bruyne, F., Hoppe, A., Ahmadi, A., & Zhang, G. (2012). Notch stress concepts for the fatigue assessment of welded joints – background and applications [Modern Local Design Concepts for the Fatigue Assessment of Welded Structures – Industrial Applications]. *International Journal of Fatigue*, 34(1), 2–16. <https://doi.org/https://doi.org/10.1016/j.ijfatigue.2010.04.011>
- Stiansen, S. (1984). Interrelation between design, inspection and redundancy in marine structures. *National Academy Press Washington D.C.*
- Sumeracki, M. (2018). Understanding sample sizes and the word "significant". *Learning scientists*. <https://www.learningscientists.org/blog/2018/11/1-1>

- Sungwoo, I., & Joonmo, C. (2021). Comparison of fatigue provisions in various codes and standards-part 1: Basic design s-n curves of non-tubular steel members. *Journal of Ocean Engineering and Technology*, 35(2), 161–171. <https://doi.org/10.26748/KSOE.2021.001>
- Tomaszewski, T. (2018). Analysis of the statistical size effect model with a critical volume in the range of high-cycle fatigue [ECF22 - Loading and Environmental effects on Structural Integrity]. *Procedia Structural Integrity*, 13, 1756–1761. <https://doi.org/https://doi.org/10.1016/j.prostr.2018.12.372>
- Tomaszewski, T. (2020). Statistical size effect in fatigue properties for mini-specimens. *Materials*, 13(10). <https://doi.org/https://doi.org/10.3390/ma13102384>
- Tomaszewski, T., Sempruch, J., & Piatkowski, T. (2014). Verification of selected models of the size effect based on high-cycle fatigue testing on mini specimens made of en aw-6063 aluminum alloy. *Journal of Theoretical and Applied Mechanics*, 52, 883. <https://doi.org/10.15632/jtam-pl.52.4.883>
- Walker, K. (1970). The effect of stress ratio during crack propagation and fatigue for 2024-t3 and 7075-t6 aluminum. <https://api.semanticscholar.org/CorpusID:137690461>
- Wöhler, A. (1860). *Versuche über die festigkeit der eisenbahnwagenachsen*.
- Xiao, W., Chen, H., & Yin, Y. (2012). Effects of surface roughness on the fatigue life of alloy steel. *Key Engineering Materials*, 525-526, 417–420. <https://doi.org/10.4028/www.scientific.net/KEM.525-526.417>
- Xiao, Z.-G., & Yamada, K. (2005). Fatigue strength of intersecting attachments. *Journal of Structural Engineering*, 131(6), 924–932. [https://doi.org/10.1061/\(ASCE\)0733-9445\(2005\)131:6\(924\)](https://doi.org/10.1061/(ASCE)0733-9445(2005)131:6(924))
- YPI. (2020). *Metals surface finish and surface roughness* (tech. rep.). Yaang Pipe Industry. <https://www.epowermetals.com/what-metals-surface-finish-and-surface-roughness.html>
- Yuan, H. (2011). Optimization of rib-to-deck welds for steel orthotropic bridge decks.
- Zamiri Aklaghi, F., Al-Emrani, M., Fryba, L., & Urushadze, S. (2009). Fatigue testing and analysis of an orthotropic bridge welded detail using structural hot spot stress method.
- Zehnder, A. T. (2013). Modes of fracture. In Q. J. Wang & Y.-W. Chung (Eds.), *Encyclopedia of tribology* (pp. 2292–2295). Springer US. [https://doi.org/10.1007/978-0-387-92897-5\\_258](https://doi.org/10.1007/978-0-387-92897-5_258)
- Zenner, H., & Hinkelmann, K. (2019). August wöhler – founder of fatigue strength research. *Steel Construction*, 12(2), 156–162. <https://doi.org/https://doi.org/10.1002/stco.201900011>
- Zheng, K., Feng, X., Heng, J., Zhu, J., & Zhang, Y. (2019). Fatigue reliability analysis of rib-to-deck joints using test data and in-situ measurements. *Applied Sciences*, 9(22). <https://doi.org/10.3390/app9224820>
- Zhu, S.-P., Ai, Y., Liao, D., Correia, J. A., De Jesus, A. M., & Wang, Q. (2021). Recent advances on size effect in metal fatigue under defects: A review. *International Journal of Fracture*, 1–23.



# Derivations

## A.1. Weakest link theory

The weakest link concept by Blacha et al. (2013) makes use of four parameters:  $V_0$ ,  $p$ ,  $C_f$  and  $m_f$ . The process of identification of these parameters is presented in this appendix.

### Shape parameter $p$

The survival probability of an element with ascribed efficient material properties and volume equal to  $n \cdot V$  (a volume that is  $n$  times larger) can be described as:

$$P_s(n \cdot V) = e^{-n \cdot \left( \frac{\log N}{\log C_f - m_f \log \Delta \sigma} \right)^p} \quad (\text{A.1})$$

The simulation of survival probability distributions for different values of  $n$  is shown in Fig. 2. For the same value of  $P_s$ ,  $\Delta \sigma$ ,  $C_f$ ,  $m_f$  the derived fatigue life  $N$  differs. The volume effect can describe this phenomenon. It should be mentioned, that in case of cyclic loading good estimates of this effect can be produced by a continuous, monotonic function [20]. The following notation is proposed:

$$\log(N(V)) = s \cdot \log(N(n \cdot V)) \quad (\text{A.2})$$

where  $N(V)$ ,  $N(n \cdot V)$  - number of cycles to failure for the volume of  $V$  and  $n \cdot V$ , respectively,  $s$  - parameter proposed to describe the volume effect (coefficient of proportionality, in the logarithmic scale). From the comparison of  $P_s$  probabilities derived for volume  $V$  and  $n \cdot V$

$$e^{-\left( \frac{\log N(V)}{\log C_f - m_f \log \Delta \sigma} \right)^p} = e^{-n \left( \frac{\log N(n \cdot V)}{\log C_f - m_f \log \Delta \sigma} \right)^p} \quad (\text{A.3})$$

and with the consideration of relation equation (A.2), the following formula can be derived:

$$e^{-\left( \frac{s \cdot \log N(n \cdot V)}{\log C_f - m_f \log \Delta \sigma} \right)^p} = e^{-n \left( \frac{\log N(n \cdot V)}{\log C_f - m_f \log \Delta \sigma} \right)^p} \quad (\text{A.4})$$

After the transformations of

$$\left( \frac{s \cdot \log N(V)}{\log C_f - m_f \log \Delta \sigma} \right)^p = n \left( \frac{\log N(V)}{\log C_f - m_f \log \Delta \sigma} \right)^p \quad (\text{A.5})$$

it can be concluded that  $s^p = n$  and  $p = \frac{\log n}{\log s}$ .

### Scale parameter $H$

Scale parameter  $H$ , where  $H = \log C_f - m_f \log \Delta \sigma$ , is in the form of number of cycles to failure determined from the efficient material S-N curve. Such a curve is described by two parameters:  $C_f$  and  $m_f$ .

The identification process requires the knowledge of the number of cycles to failure for a given geometry and survival probability  $P_s$ . The identification criteria involved in this approach can be ideally met through the application of the nominal stress approach and FAT S-  $N$  curves [4]. The FAT number is equal to stress range ( $\Delta \sigma = \text{FAT}$ ) at  $2 \times 10^6$  cycles, derived for 95% survival probability  $P_s$ .

The process of identification of the  $C_f$  and  $m_f$  parameters proceeds through Nelder-Mead minimization of the  $E(C_f, m_f)$  estimator for efficient material parameters:

$$E(C_f, m_f) = 0,95 - e^{-(\log N_{FAT})^p} \int_V \left( \frac{1}{\log C_f - m_f \log \Delta \sigma} \right)^p dV \tag{A.6}$$

$$E(C_f, m_f) \rightarrow 0$$

where  $N_{FAT}$  – number of cycles to failure derived from the nominal stress approach.

Referential volume  $V_0$  for efficient material is assumed to be equal to  $1 \text{ mm}^3$ . In the assumptions underlying the model, the grade of the steel elements being joined (in fatigue analysis grade of most steels is of secondary importance), do not affect the efficient material characteristic. Similar situation arises in case of their geometry. Only a slight impact is forecasted since during the calculations not only the notch but also the surrounding volume has an influence on the distribution (non-local fatigue assessment method).

**Probability of failure relationships**

For the investigated elements, the obtained parameters for  $\log C_f$ ,  $m_f$ , and  $p$  were 13.65, and 3.18, and 66.82 respectively. The investigated elements had a total weld volume of around  $800 \text{ mm}^3$ . For this thesis it is interesting to investigate what the effect of the weld volume is on the probability of failure. For that, figures A.1 and A.2 were made. Figure A.1 shows the relationship between the failure probability and the number of cycles. For this graph, the stress range was kept constant at 100 MPa, to visualize what the influence of the number of cycles is on the failure probability for different weld volumes. The different weld volumes vary with  $700 \text{ mm}^3$ . The graph shows that the higher the weld volume is, the number of cycles have less of an effect on the failure probability.

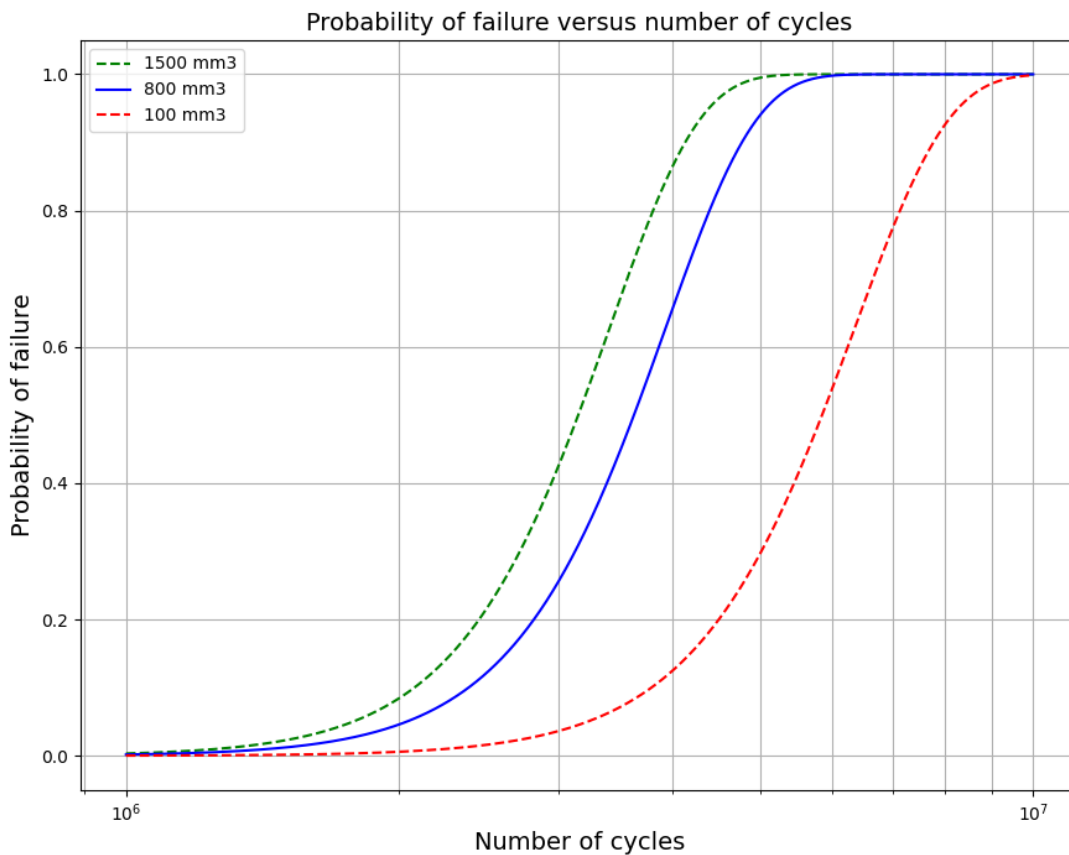


**Figure A.1:** Relationship between the probability of failure  $P_f$  and number of cycles  $N$

Figure A.2 shows the relationship between the failure probability and the stress range. For this graph, the number of cycles  $N$  was kept constant at  $2 \cdot 10^6$  to investigate the influence of the stress range on the failure probability for multiple weld volumes. Here, the same behaviour can be seen that the sensitivity of an increasing weld volume decreases. A weld volume of  $100 \text{ mm}^3$  has a failure probability of 0.6 at around 150 MPa. At  $800 \text{ mm}^3$ , the same failure probability is at 125 MPa, around 25 MPa lower. For a big increase in weld volume,  $200000 \text{ mm}^3$  the same failure probability is at around 80 MPa. So the stress is only 65% of the stress compared to a weld volume of  $800 \text{ mm}^3$ , while the weld volume has increased by 250 times. However, these extrapolated results can not be interpreted directly. The parameters have been optimized for small-scale specimens, so extrapolating these results to a weld volume that is 250 times larger is not accurate.

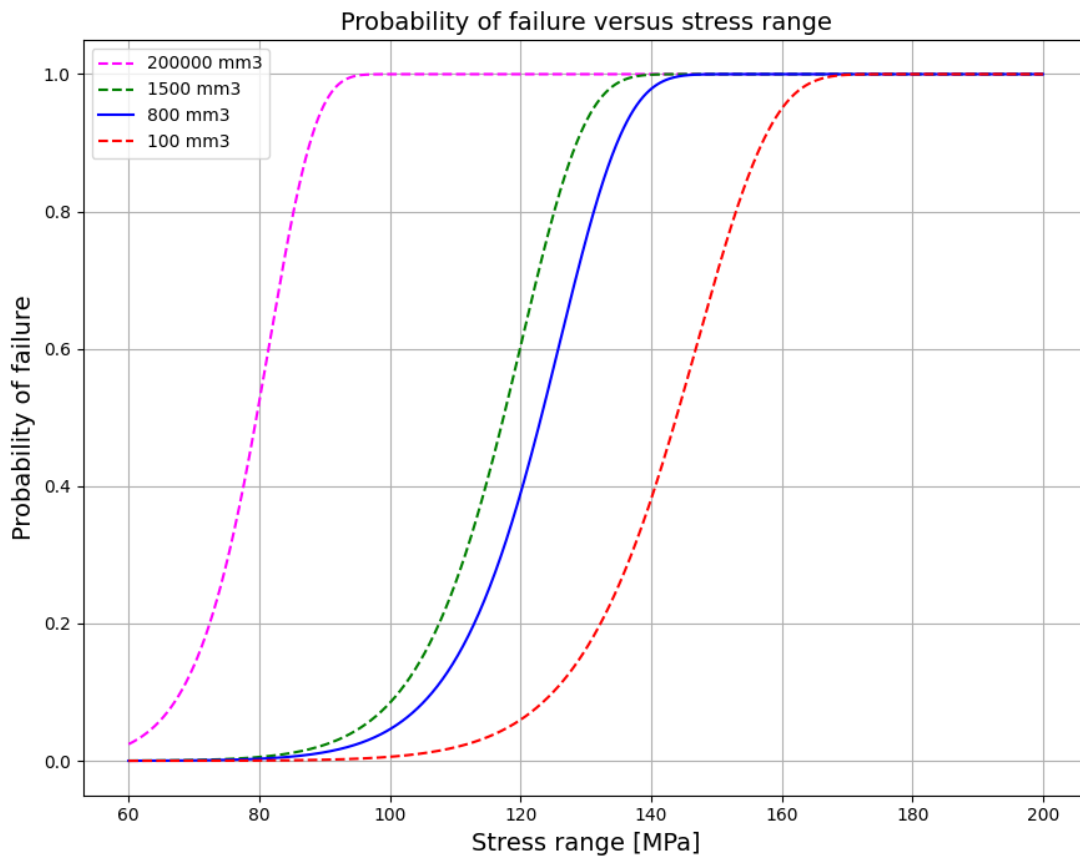


**Figure A.2:** Relationship between the probability of failure  $P_f$  and stress range  $S$

# B

## HSSSC analysis

### B.1. Bilge corner

The bilge corner, as a hot spot type C is considered, uses the following method by Dong (2003). The nodal forces need to be converted to line forces, using the table in figure B.1. In the table,  $F_n$  are the nodal forces, where  $n$  is the node number. The line forces are given as  $f_n$  and  $l_n$  is the distance between node  $n$  and node  $n + 1$ . To calculate the line forces, the matrix dependent on  $l_n$  is constructed and inverted, followed by a multiplication with the nodal forces vector. The resulting vector holds the line forces. The same method works for the line moments  $m_n$ .

$$\begin{Bmatrix} F_1 \\ F_2 \\ F_3 \\ \cdot \\ \cdot \\ F_n \end{Bmatrix} = \begin{bmatrix} \frac{l_1}{3} & \frac{l_1}{6} & 0 & 0 \\ \frac{l_1}{6} & \frac{(l_1+l_2)}{3} & \frac{l_2}{6} & 0 \\ 0 & \frac{l_2}{6} & \frac{(l_2+l_3)}{3} & \frac{l_3}{6} \\ 0 & 0 & \dots & \dots \end{bmatrix} \begin{Bmatrix} f_1 \\ f_2 \\ f_3 \\ \cdot \\ \cdot \\ f_n \end{Bmatrix}$$

Figure B.1: Method to convert nodal forces to line forces

A calculation is shown in figure B.2. This calculation is done for a mesh size of  $L = 75\text{mm}$ , which equals 5 nodes over the width of 300 mm. From left to right, this gives a 5x5 matrix, a 5x5 inverted matrix, two 5x1 nodal force and nodal moment vectors, together with two 5x1 line force and moment vectors. The values for the middle node are used in equation (B.1), which gives  $\sigma_m$ ,  $\sigma_b$  and  $\sigma_s$ .

$$\sigma_s = \sigma_m + \sigma_b = \frac{f'_x}{t_p} + \frac{6m'_y}{t_p^2} \quad (\text{B.1})$$

											F	M	f'	m'	sigma_m	sigma_b	sigma_s
25	12,5	0	0	0	0,046	-0,012	0,003	-0,001	0,000		202	32	4,4	0,4	0,73	0,06	0,8
12,5	50	12,5	0	0	-0,012	0,025	-0,007	0,002	-0,001		520	356	7,3	1,8	1,22	0,30	1,5
0	12,5	50	12,5	0	0,003	-0,007	0,023	-0,007	0,003		572	1095	7,8	21,0	1,29	3,49	4,8
0	0	12,5	50	12,5	-0,001	0,002	-0,007	0,025	-0,012		522	368	7,4	2,0	1,23	0,33	1,6
0	0	0	12,5	25	0,000	-0,001	0,003	-0,012	0,046		203	39	4,4	0,6	0,73	0,09	0,8

Figure B.2: Structural stress calculation

This calculation has been done 5 times with mesh sizes between 75 mm and 25 mm. The results converge to the value of  $\sigma_s = 6.4$ . This can be seen in figure B.3.

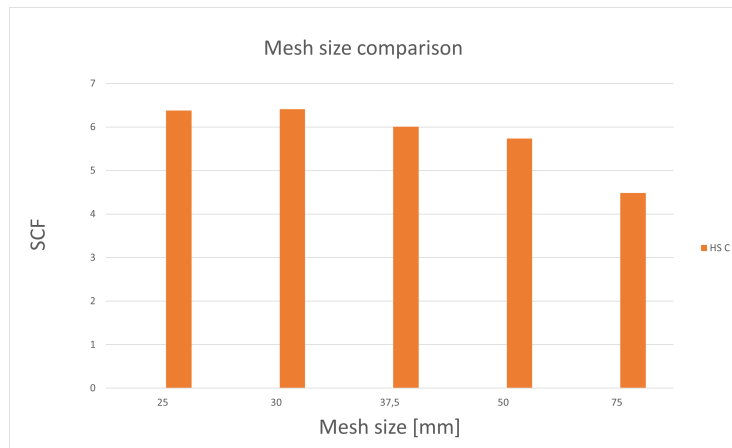


Figure B.3: Structural stress mesh size comparison

## B.2. T-shaped stiffener

On the T-shaped stiffener, a hot spot type A is present. This changes the calculation compared to the bilge corner. Now the virtual node method by Dong (2003) is adopted, which is visualized in figure B.4. In the figure,  $F_n$  are the nodal forces,  $L$  is the distance between the nodes,  $L_1$  is the distance to the virtual node, and  $f_n$  are the line forces. Using equation (B.2), the line force can be calculated, and with the same method, the line moment can be calculated. This results are once again used in equation (B.1) to obtain the structural stress.

$$f_1 = \frac{F_1(L_1 + L) + F_2(L_1 - L)}{L_1 L} \quad (\text{B.2})$$

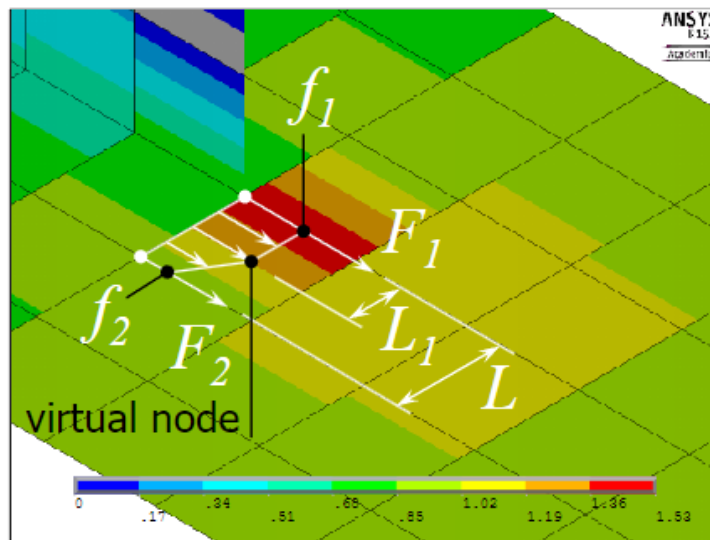
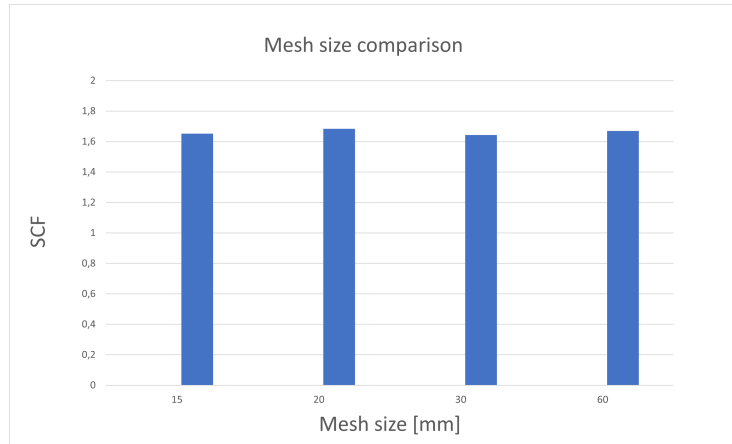


Figure B.4: Virtual node method (den Besten, 2021b)

The calculation for the T-shaped stiffener is shown in figure B.5. In this calculation the element size  $L$  is 15 mm, while  $L_1 = 13.6$ . Calculations were also performed for different mesh sizes which showed similar results, these results are shown in figure B.6.

Node	NFORC2	NFORC4	f'	m		sigma_m	sigma_b	sigma_s
1	-194,0	274,9	-13,0	18,4		1,00	0,652	1,65
86	-193,5	273,9						

**Figure B.5:** Stress calculation using the virtual node method



**Figure B.6:** Structural stress mesh size comparison

### B.3. Scallop

Lastly are the calculations for the scallop. This hot spot is also a type A, so the virtual node method will again be adopted. The nodal forces and calculations are shown in figure B.7. Here  $L$  is equal to the element size, and  $L_1 = 10.5$ . The mesh size comparison is shown in figure B.8. For this calculation the nodal and line moments were not needed as there is no bending moment in the plate of the specimen.

Element size	F1	F2	f_m	$\sigma_s$
12,50	76,09	62,06	12,39	1,38
16,67	97,44	74,10	12,51	1,39
20,00	118,37	111,24	12,16	1,35
25,00	137,71	121,60	11,91	1,32
33,33	169,30	140,00	12,07	1,34

**Figure B.7:** Nodal forces of the scallop for different mesh sizes

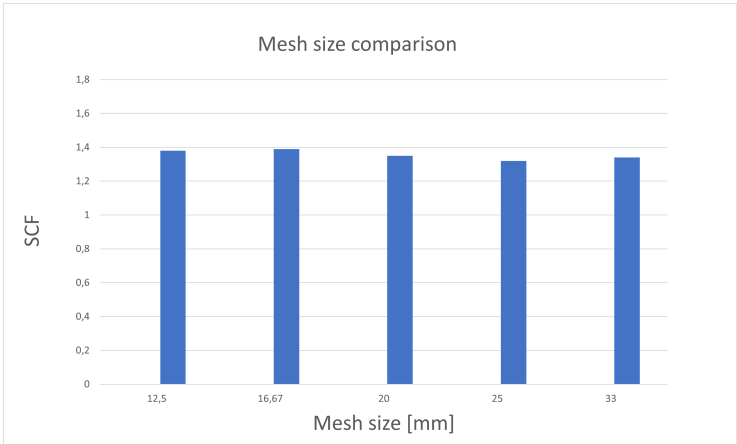
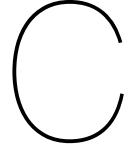


Figure B.8: Structural stress mesh size comparison



## ENSC analysis

The ENSC calculation used the averaged effective notch stress approach, shown in equation (C.1). This approach adopts the weld toe notch stress distribution. All large-scale specimens make use of the symmetry variant by den Besten (2015). All equations are listed below.

$$\sigma_e = \frac{1}{\rho^*} \int_0^{\rho^*} \sigma_n(r) dr \quad (C.1)$$

$$\begin{aligned} \sigma_n\left(\frac{r}{t_p}\right) = & \sigma_s \left\{ \left[ 1 - 2 \cdot r_s \left\{ 1 - f\left(\frac{r}{t_p} = \frac{1}{2}\right) \right\} \right] f\left(\frac{r}{t_p}\right) \right. \\ & \left. + r_s \cdot \left\{ 2f\left(\frac{r}{t_p} = \frac{1}{2}\right) - 1 \right\} \cdot \left[ \left\{ 1 - f\left(\frac{r}{t_p} = \frac{1}{2}\right) \right\} - 2 \cdot \left(\frac{r}{t_p}\right) \right] \right\} \end{aligned} \quad (C.2)$$

$$f\left(\frac{r}{t_p} = \frac{1}{2}\right) = \frac{(\lambda_a - \lambda_s)(\lambda_s \lambda_a - 2C_{bw})}{\lambda_a(\lambda_a - 1) - \lambda_s(\lambda_s - 1)} + C_{bw} \quad (C.3)$$

$$\begin{aligned} f\left(\frac{r}{t_p}\right) = & \left[ \left(\frac{r}{t_p}\right)^{\lambda_s - 1} \mu_s \lambda_s (\lambda_s + 1) [\cos\{(\lambda_s + 1)\beta\} - \chi_s \cos\{(\lambda_s - 1)\beta\}] + \right. \\ & \left. \left(\frac{r}{t_p}\right)^{\lambda_a - 1} \mu_a \lambda_a (\lambda_a + 1) [\sin\{(\lambda_a + 1)\beta\} - \chi_a \sin\{(\lambda_a - 1)\beta\}] + \right. \\ & \left. C_{bw} \left\{ 4\left(\frac{r}{t_p}\right) - 1 \right\} \right] \end{aligned} \quad (C.4)$$

$$\begin{aligned} \mu_s = & \frac{(\frac{1}{2})\lambda_a(\lambda_a - 1) + C_{bw}}{C_s [\cos\{(\lambda_s + 1)\beta\} - \chi_s \cos\{(\lambda_s - 1)\beta\}]} \\ \mu_a = & - \frac{(\frac{1}{2})\lambda_s(\lambda_s - 1) + C_{bw}}{C_a [\sin\{(\lambda_a + 1)\beta\} - \chi_a \sin\{(\lambda_a - 1)\beta\}]} \end{aligned} \quad (C.5)$$

$$\begin{aligned} C_s = & \left(\frac{1}{2}\right)^{\lambda_s} (\lambda_s + 1) \{\lambda_a(\lambda_a - 1) - \lambda_s(\lambda_s - 1)\} \\ C_a = & \left(\frac{1}{2}\right)^{\lambda_a} (\lambda_a + 1) \{\lambda_a(\lambda_a - 1) - \lambda_s(\lambda_s - 1)\} \end{aligned} \quad (C.6)$$

With  $\lambda_a, \lambda_s$  being the first eigenvalues of the (anti-)symmetry parts and  $\chi_a, \chi_s$  being the first eigenvalue

coefficients of the (anti-)symmetry parts.

Combining all definitions, equation (C.1) becomes equation (C.7).

$$\begin{aligned}
\sigma_e &= \frac{1}{\rho^*} \int_0^{\rho^*} \sigma_n(r) \mathbf{d}r \\
&= \sigma_s \left( \frac{t_p}{\rho^*} \right) \left\{ \left[ 1 - 2r_s \left\{ 1 - f \left( \frac{r}{t_p} = \frac{1}{2} \right) \right\} \right] \right. \\
&\quad \left( \left( \frac{\rho^*}{t_p} \right)^{\lambda_s} \mu_s (\lambda_s + 1) [\cos\{(\lambda_s + 1)\beta\} - \chi_s \cos\{(\lambda_s - 1)\beta\}] + \right. \\
&\quad \left. \left( \frac{\rho^*}{t_p} \right)^{\lambda_a} \mu_a (\lambda_a + 1) [\sin\{(\lambda_a + 1)\beta\} - \chi_a \sin\{(\lambda_a - 1)\beta\}] + \right. \\
&\quad \left. C_{bw} \left\{ 2 \left( \frac{\rho^*}{t_p} \right)^2 - \left( \frac{\rho^*}{t_p} \right) \right\} + \right. \\
&\quad \left. r_s \left\{ 2f \left( \frac{r}{t_p} = \frac{1}{2} \right) - 1 \right\} \cdot \left[ \left\{ 1 - f \left( \frac{r}{t_p} = \frac{1}{2} \right) \right\} \cdot \left( \frac{\rho^*}{t_p} \right) - \left( \frac{\rho^*}{t_p} \right)^2 \right] \right\}
\end{aligned} \tag{C.7}$$